Light management films for enhanced harvesting in printable photovoltaics

Inauguraldissertation

zur
Erlangung der Würde eines Doktors der Philosophie
vorgelegt der
Philosophisch-Naturwissenschaftlichen Fakultät
der Universität Basel

von

Jan Axel Mayer
aus Ulm, Deutschland

Basel, 2017

Genehmigt von der Philosophisch-Naturwissenschaftlichen Fakultät
auf Antrag von

Prof. Dr. C. Schönenberger
Dr. R. Ferrini
Prof. Dr. C. Brabec
Prof. Dr. O. Inganäs

Basel, den 21.02.17

Prof. Dr. Martin Spiess
Dekan

"The world is in greater peril from those who tolerate or encourage evil than from those who actually commit it." - Albert Einstein

für Moritz

Abstract / Zusammenfassung

Abstract

Printed organic photovoltaics promise lightweight and flexible light harvesting devices for conformable integration into buildings, portable electronics or vehicles. Besides the challenges in material synthesis and engineering of the printing processes, the optical design of these thin film layer devices is inevitable to achieve high power conversion efficiencies.

In this respect, light management, which denotes the control of light incoupling and light absorption in the device by photonic micro- and nanostructures, plays an increasingly important role.

In this thesis, dielectric diffractive nanostructures are introduced as such light management solution, which stands out due to its device-independent fabrication. The optical properties of the periodic structures and the angle dependent absorption in the OPV devices are carefully analyzed and their enhancement potential is demonstrated experimentally on single-junction and tandem devices.

To demonstrate the applicability of this class of light management solutions, advanced nanostructures are fabricated, on the one hand, as self-standing foils to reveal their potential for mass production and, on the other hand, as buried structures, which provide protection against abrasion.

An optical model is developed in this thesis, which enables the optimization of the geometrical parameters of the nanostructure, with respect to the yearly harvested energy in different application-relevant device orientations (façade, consumer electronics, shading, automotive).

Zusammenfassung

Die gedruckte organische Photovoltaik verspricht leichte und flexible Solarzellen für die konforme Integration in Gebäude, elektronische Mobilgeräte oder Fahrzeuge. Neben der Synthetisierung von Materialien und der Weiterentwicklung der Druckprozesse, ist dabei das optische Design dieser Dünnschichtzellen unverzichtbar, um einen hohen Wirkungsgrad zu erreichen.

In diesem Zusammenhang spielt Lichtmanagement, welches die Kontrolle über Lichteinkopplung und Lichtabsorption in den Zellen mit Hilfe von Mikro- und Nanostrukturen beschreibt, eine immer größere Rolle.

In dieser Arbeit werden dielektrische, diffraktive Nanostrukturen als ein solcher Lichtmanagement Ansatz vorgestellt, welcher sich insbesondere durch seine Solarzellen unabhängige Herstellung auszeichnet. Die optischen Eigenschaften der periodischen Strukturen, sowie die winkelabhängigen Absorption in den Zellen, werden dabei sorgfältig untersucht und ihr Verbesserungspotenzial experimentell auf Einzel- und Tandemzellen demonstriert.

Um die Eignung dieser Art von Lichmanagement Lösungen für die Anwendung zu demonstrieren, werden verschiedene weiterentwickelte Nanostrukturen hergestellt, einerseits als selbständige Folien, um ihr Potenzial für die Massenproduktion aufzuzeigen, und andererseits als eingelassene Strukturen, welche den Schutz gegen Abnutzung gewährleisten.

Ein optisches Simulationsmodel wird in dieser Arbeit entwickelt, welches die optimierung der strukturellen Parameter der Nanostrukturen mit Bezug auf die jährliche Energieausbeute in verschiedenen anwendungsrelevanten Zellorientierungen ermöglicht (Fassaden, Konsumerelektronik, Sonnenschutz, Fahrzeugtechnik).

Contents

Abstract / Zusammenfassung iv

Introduction ix

I Principles 1

1 Printed photovoltaics and light management: overview 2
1.1 Printed photovoltaics . . . 2
1.1.1 Solution processible solar cells . . . 4
1.1.2 Organic photovoltaics (OPV) . . . 5
1.2 Light management . . . 7
1.2.1 State of the art . . . 7
1.3 Aim of the thesis . . . 10

2 Theoretical background 12
2.1 Organic solar cells . . . 12
2.1.1 Organic semiconductors . . . 12
2.1.2 Device physics . . . 13
2.2 Optical absorption in OPV . . . 17
2.2.1 Functional layers . . . 17
2.2.2 Thin film interference . . . 19
2.3 Light management . . . 19
2.4 Diffractive nanostructures . . . 20
2.4.1 Periodic nanostructures . . . 21
2.4.2 Diffraction pattern & light management . . . 25

3 Experimental methods & optical modeling **27**
3.1 Experimental methods . . . 27
3.1.1 Solar cell fabrication . . . 27
3.1.2 Nanostructure fabrication . . . 28
3.1.3 Solar cell characterization . . . 31
3.1.4 Nanostructure characterization . . . 34
3.2 Optical modeling . . . 36
3.2.1 Surface reflections . . . 36
3.2.2 Periodic nanostructures . . . 37
3.2.3 Thin film solar cells . . . 38
3.2.4 Combination of RCWA and TMM . . . 40

4 Proof of principle **44**
4.1 Reference device . . . 44
4.2 Angle dependent modeling . . . 46
4.2.1 Optical path length . . . 47
4.2.2 Interference effects . . . 50
4.2.3 Influence of device architecture . . . 51
4.3 Experimental validation . . . 53
4.3.1 Optimization of the diffractive nanostructures . . . 53
4.3.2 Period dependence . . . 53
4.3.3 Efficiency improvement . . . 54
4.3.4 Spectral analysis . . . 55
4.3.5 Testing the light management . . . 57

II Applications **59**

5 Advanced structures **60**
5.1 Crossed nanostructures . . . 60
5.2 Plastic lamination . . . 64
5.3 Embedded nanostructures . . . 66
5.3.1 Optimization of light trapping . . . 67
5.3.2 Experimental results . . . 68
5.3.3 Angle dependency . . . 70

6 Application to optimized devices **72**
6.1 Single-junction devices . . . 73
6.1.1 Different device architectures (simulation) . . . 73
6.1.2 Different active layer thicknesses (experimental) . . . 75
6.2 Tandem devices . . . 78
6.2.1 Optical simulations of multi-junction cells . . . 79
6.2.2 Light management in tandem devices . . . 80

6.2.3 Experimental 81

7 Yearly energy harvesting **83**
7.1 Illumination conditions 84
7.2 Modeling the yearly performance 86
7.2.1 Hourly angle 87
7.2.2 Hourly spectra 90
7.2.3 Averaged azimuth response 92
7.2.4 Extrapolated azimuth response 94

III Backmatter **99**

Conclusions & Outlook **100**

Bibliography **104**

A Correction factors **115**
A.1 Spectral mismatch 115
A.2 Quartz window 118
A.3 Other spectra 119

Publications **120**

Acknowledgements **122**

Introduction

Advanced semiconductor materials, which convert light into electricity, can provide photoelectric liquids and thus enable the processing of light absorber layers at low temperatures. Combined with other solution-based functional materials, they form the basis of an emerging field, which holds out the prospect of high-throughput, low-cost, lightweight and flexible energy supply: Printed photovoltaics.

Provoked by the possibilities of this technology, the intensive research in the past decades on the associated semiconductors and their device physics, have steadily increased the power conversion efficiency (PCE) of printable photovoltaic devices. This progress can mainly be categorized into three fields:

- **Material development** - Chemical design of the semiconductor absorbers and other functional layers of the device, including energy levels optimization for a maximum power output.
- **Process engineering** - Investigation of the coating dynamics, interface and phase formation of the absorber layers and optimization of process conditions, regarding choice of solvents, deposition, drying and annealing steps.
- **Optical design** - Device design and optical optimization of layer thicknesses as well as light management, which denotes the optimization of light in-coupling and light absorption (e.g. by using photonic structures).

All three fields are usually influencing each other, which puts a huge challenge on the overall optimization of the device performance. The development of a new material often requires a new processing procedure and changed optical constants will give rise to different layer thickness for maximum absorption. On the other hand, the ideal optical design may be compromised by the thickness restriction of a chosen absorber material or by its deposition technique.

Furthermore, additional optical nanostructures may compromise an already developed process for ideal layer formation.

Recent developments have shown great progress especially in the first two fields. The development of new materials [1–3] and process engineering [1, 4, 5] has led to photovoltaic devices with excellent electrical properties [6–9]. This being said, high potential for further improvements particularly remains in the latter field. Since devices with good electric properties and a successful extraction of photogenerated charges usually require very thin absorber films, the absorption and hence the power conversion efficiency of printable solar cells is limited by the semiconductor layer thickness. Light management (LM) for printed photovoltaics by introducing photonic structures outside (external LM) or inside the device (integrated LM) is therefore becoming more and more important in the development of new device designs [10–12] and therefore constitutes the topic of the present thesis.

Motivation

In order to comply with the properties of printed photovoltaics, light management has to fulfill certain guidelines, which have been discussed in several review articles [13–16] and which can be summarized as follows:

- The enhancement in efficiency must not come at the expense of parasitic absorption or electronic losses
- The solutions should be cost-efficient in the integration and robust in withstanding operation conditions (weathering resistance, mechanical stability)
- The structures should exhibit mechanical flexibility and compatibility with large-area printing techniques of solution processible photovoltaics.
- The performance under oblique angles should be assessed to estimate the integrated energy harvested throughout a full year, rather than only the performance under straight incidence

The objective of this thesis is to develop light management solutions, which apply to all the above listed requirements and at the same time are preferably decoupled from the materials and processes of printed photovoltaics.

Firstly, to ensure that the interference with the delicate printing process of the absorber layer is completely avoided, external optical structures have to be chosen. However, when applied on the sunward surface of the device, these

structures are prone to abrasion during operation. Hence a solution is needed that is able to protect this sensitive optical interface.

Secondly, the light management should be applicable also for newly developed absorber materials or different light conditions. The first is challenging, since the optics of the thin film stack are determined by the material permittivities. Hence, a versatile solution has to be found, which contains several degrees of freedom, and which can thus be adapted to new material systems and light conditions, without changing its basic concept or its fabrication technique.

This thesis introduces dielectric diffractive nanostructures, as an external, transparent and eventually protected light management solution for printed photovoltaics. The structures can be imprinted in flexible plastics foils, which is fully independent from the PV device fabrication but still compatible with high-throughput roll-to-roll production [17]. Depending on the device architecture or the application case, the spectral and angular response of the nanostructure can be adapted through variation of its structural parameters. For this purpose, existing optical simulation models are extended to address the optimization of these nanostructures.

In order to investigate and demonstrate the potential of this light management solution, the concept will be applied to organic photovoltaics (OPV) in this thesis. Among the printable PV technologies that are briefly reviewed in the first chapter, OPV currently hold the highest potential for large scale production. Several companies[1] (InfinityPV, OPVIUS, eight19, Armor, Disa-Solar, epishine and CSEM Brazil) are currently producing ready-to-use organic photovoltaic modules [18, 19]. However, owing to its flexibility and device independent fabrication, this light management solution is generally applicable to other printed photovoltaic technologies.

[1] without any claim to completeness

Outline & structure

PART I - Principles:

In **Chapter 1**, an overview on printed photovoltaics is provided, including the state-of-the-art and potential applications, followed by an overview of existing light management solutions in this field, which leads to the aim of this thesis.

In **Chapter 2**, the theoretical background is reviewed, discussing principles of organic solar cells with a focus on their optical properties. This is followed by an introduction to the diffraction properties of periodic nanostructures, which constitute the light management solution of this thesis.

Chapter 3 is devoted to the experimental details, which include fabrication and characterization of both the solar cells and the nanostructures. In the second part, the optical simulation model is introduced.

In **Chapter 4**, the reference OPV device is introduced, which constitutes the basis of both the following optical analysis and the experimental proof of concept.

PART II - Application:

In **Chapter 5**, three concepts are investigated in order to improve the applicability of the light management simulation, leading to a improved angular response, a lamination process and a protected configuration.

In **Chapter 6** the present light management solution is applied to optimized devices, in order to show its adaptability to different device configurations, including tandem solar cells.

Chapter 7 focuses on the expansion of the simulation model to study yearly illumination conditions. Calculations of the expected yearly enhancement are performed for different light management solutions of the previous chapters.

PART III - Backmatter:

Finally a conclusion and an outlook on the topic is given, followed by the Bibliography and the Appendix.

PART I

PRINCIPLES

1

Printed photovoltaics and light management: overview

1.1 Printed photovoltaics

Broader context

Global energy consumption has nearly doubled in the past 40 years, increasing from 195 EJ (1973, 1 Exajoule (EJ) = 10^{18} Joule ≈ 277.8 TWh) to 389 EJ in 2013 and it is estimated to rise to over 800 EJ per year by 2050, in continuation of this trend [20, 21]. Meanwhile, mankind has realized that a massive emission of greenhouse gases will lead to a suppression of the earth's infrared energy emission and in consequence to a continuous heating of our world's climate, if this increasing demand is satisfied by fossil fuels. In a historic conference in December 2015 in Paris, 175 countries have decided to restrict global warming to below 2°C, promoting a contract, which is put into effect since 4th of November 2016 [22]. Since 2011, the European Commission already carried out huge effort to increase the ratio of carbon-neutral renewable energy sources, to now over 16% (2014) [23] with the goal to reduce greenhouse gases by 80% – 95% by 2050 (compared to 1990) [24]. Very recently, an European country (Portugal) was able to run four days straight on emission-free renewable energy sources [25].

Although the right path has been trodden with the extension of wind and solar power plants, the global share of renewable energy sources is still below 6%. If one considers that within 3.5 hours, 1000 EJ of solar power is impinging the

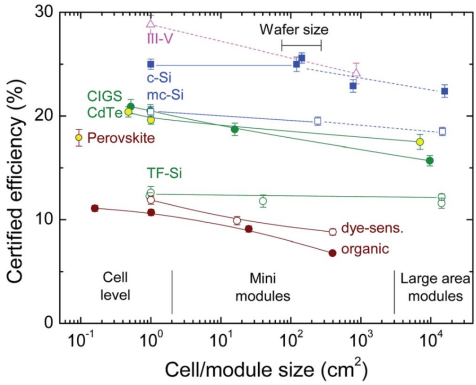

Figure 1.1: Certified solar cell efficiencies for various photovoltaic technologies and their up-scaling behaviour. Reproduced from Ref. [12] with permission from The Royal Society of Chemistry. The data is based on the certified efficiencies published by the U.S. National Renewable Energy Laboratory (NREL) [26]

earth's surface (exceeding today's global yearly energy demands by far) it is hard to imagine a future where carbon-neutral solar energy sources have only a minor share in global energy production.

Consequently, solutions are sought, on the one hand, to further extend the installed photovoltaic capacities by reducing the manufacturing cost of light harvesting technologies and, on the other hand, to increase the integrability of solar harvesting in applications, for which conventional photovoltaics (PV) are not suitable. Both considerations have supported the development of thin film photovoltaic (TFPV) technologies with sub-micron absorber thicknesses. Besides a reduction of material costs, some devices offer desirable new device properties, namely mechanical flexibility and/or even semi-transparency. Consequently, their field of potential applications reach from building facades and conformable fairing of vehicles to local off-grid energy harvesting in mobile electronic devices to power sources for the Internet of Things (IoT), wearables or clothing [19]. An overview of state of the art of thin film photovoltaic technologies is shown in Fig. 1.1 [12] for cells (< 1 cm) and modules (≥ 1 cm) and compared with first generation PV technologies (III-V, c-Si, mc-Si).[1]

[1] III-V seminconductors are e.g. GaAs,GaN,GaInAs; Silicon based photovoltaics are distinguished between crystalline (c-Si) and microcrystalline (mc-Si) solar cells

Table 1.1: Efficiency records for flexible and printed small area (< 2 cm) single-junction solar cells for different solution processible TFPV technologies.

system	solution-processed	flexible	flex & printed
CdTe	11,6% [27]	16.4% [28]	—
CIGS	13.8% [29]	20.4% [30]	—
CZTS	12.6% [31]	—	—
Organic	**11.4%** [5, 32]	**7.8%** [33]	**6.5%** [33]
Perovskites	12% [34]	16.2% [35]	4.9% [36]
$AgBiS_2$	6.3% [37]	—	—

1.1.1 Solution processible solar cells

Some of these TFPV technologies are solution-processible, which enables solar cells fabricated via high-throughput technologies that are well established from other industries. If the semiconductors can be coated onto flexible substrates and techniques like roll-to-roll (R2R) printing are used, this can greatly support the desired cost reduction. Besides the above mentioned range of applications, the resulting printed solar cells could further offer lightweight off-grid energy harvesting for developing countries at minor costs.

Solution processible solar materials within the TFPV technologies are cadmium telluride (CdTe), copper indium gallium diselenide (CIGS), copper zink tin sulfide (CZTS), dye-sensitized solar cells (DSSC), organic/polymer solar cells and more recent developed material systems like hybrid perovskite solar cells and $AgBiS_2$. However, demonstrations of fully flexible solar cells, fabricated by up-scalable printing techniques are still rare for most of these material systems. Reported efficiencies for solution-processed, flexible and printed & flexible small area devices are reported in Tab. 1.1. Furthermore, all technologies still exhibit certain weak points: Whereas DSSC use a liquid electrolyte, which imposes difficulties in printing of full devices [18], others exhibit toxic materials like cadmium (CIGS, CdTe), tellurium (CdTe) or lead (perovskite) [38]. CIGS further depends on the availability of scarce indium and gallium and usually needs a high-temperature step which is hardly compatible with plastic substrates.

Within printable TFPV materials, organic (polymer) solar cells are the most mature technology, when it comes to large-scale printing. Moreover, they provide other advantages such as the non-toxicity of their building blocks and the possibility to be successfully fabricated without any vacuum- or high temperature production step [33].

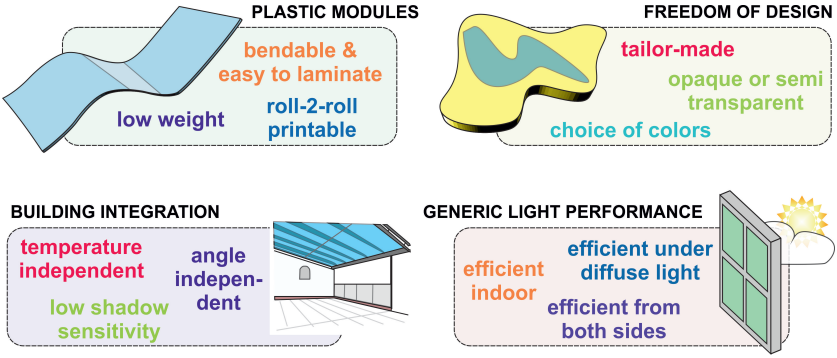

Figure 1.2: Summary of advantages accompagnied with organic photovoltaics, categorized into four main fields. (adapted from a presentation at LOPEC 2016 by Merck and from the company's homepage, accessed Jul. 2016)

1.1.2 Organic photovoltaics (OPV)

The unique advantages of OPVs resulting from these properties are classified in Fig. 1.2. Most importantly the aforementioned compatibility of the organic absorber materials with the low-temperature fabrication on plastic substrates promises lightweight, low-cost and conformable modules. Combined with free-form devices of different colors, which have been demonstrated by various research centers,[2] this offers every possibility for the integration into products.

Moreover, the integration of light-harvesting foils into building facades is one of the most exciting perspectives in this field, especially when combined with large-area production and the possibility to fabricate semi-transparent devices. With a relatively high efficiency under low light conditions [39], windows could not only harvest the sunlight with a high angular acceptance, but also convert part of the indoor light emitted by luminaires in the evening and early morning.

State-of-the-art

From an theoretical point of view, efficiencies of single-junction organic solar cells can reach up to $\eta_{PCE} = 15\%$ [40], whereas multi-junction cells have been estimated to theoretically achieve up to $\eta_{PCE} = 21\%$ [41] (see Tab. 1.2). The latter, known as tandem solar cells, are thereby composed of two spectrally complementary absorbers and can consequently harvest a larger portion of the sunlight. Record efficiencies of fabricated OPV cells have recently reached

[2] CSEM, VTT and i-MEET, to name a few

Table 1.2: State of the art power conversion efficiencies for organic photovoltaics at different development stages.

OPV design	single-junction	double-junction
Theoretical limit	15% [40]	21% [41]
cell in N_2 or vacuum	11.4% [5, 32]	11.0 [49]
cell printed* in air	8.3% [50]	10.0% [50]
module printed* in air	7.6% [51]	1.8% [52]

* printing excludes spin-coating.

certified 11.4% and 13.2% for single and multi(tripple)-junctions, respectively [5, 42] and new concepts of fullerene and ITO free device designs [3, 43] and solution-processible triple-junctions [44, 45] or ternary devices [46–48] promise further progress.

It can be seen from Tab. 1.2 that up-scaling of both the device area and the fabrication technique leads to some reduction in the efficiency. However, recent promising developments have enabled OPV modules fabricated by large-scale processes to reach PCE values between 7–8% [51, 53] for opaque and 4.5% for semi-transparent devices, the latter of which even were installed outdoors at the Universal EXPO in Milan (2015) [54], as shown in Fig. 1.3.

Figure 1.3: Examples for integrated OPV application. The picture shows the german pavillon at the EXPO world exhibition 2015 in Milan, equipped by Belectric OPV (Ref. [54]).

1.2 Light management

1.2.1 State of the art

Light management strategies for OPVs can be classified into different categories depending on their position in the device stack and the related fabrication techniques (see Fig. 1.4)

(a) Absorber or transport layer deposited on a structured substrate

(b) Structures imprinted in deposited absorber or transport layers

(c) Nanoparticles in absorber or transport layers

(d) Additional layers for interference shaping

(e) External surface structures (present thesis, see Fig. 1.5)

as well as any combination thereof. (For more details the reader is referred to several recent and comprehensive reviews on light managment for organic solar cells [15, 55–58] and for general thin film PV [11–14, 59–61])

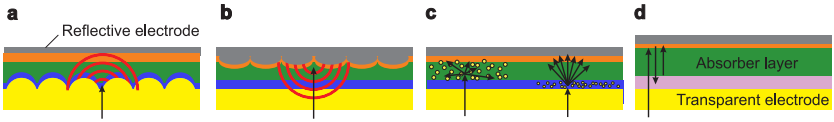

Figure 1.4: Different approaches for thin film light management. a Absorber deposition on a pre-patterned layer **b** Patterning of the active layer **c** Addition of nanoparticles **d** Optical spacer

Introducing resonant, scattering or diffractive structures in the vicinity of the absorber layer (a)–(c) can couple light into waveguided modes, i.e. the light is trapped in the absorber layer. Strategies of category (a) and (b) can additionally transfer the structure into the evaporated metal electrode, which can give rise to plasmonic field enhancement, similar to (c) if metallic particles are chosen. However, as emphasized in the introduction, these approaches will strongly influence the electrical device physics, since they interfere with the morphology and the phase formation, increase traps and interface recombination or introduce additional parasitic absorption into the functional layers of printed PV. Strategies of category (d) add one (optical spacers [62–64]) or multiple (Bragg reflectors [65], dielectric mirrors [66], photonioc crystals [67]) flat layers to the PV stack to shape its interference pattern or replace the absorbing backelectrode. Since all light management schemes of (a) – (d) thus act inside the functional (printed) layers, additional effort or complications are expected for large-area fabrication of the photovoltaic devices. [14–16, 59]

In the present thesis dielectric diffractive nanostructures are investigated, which act on the light-incident side of the device (e), thus being independently fabricated and spatially separated from the other device layers. In general, such external light management strategies are spatially separated from the solar cell (usually by a substrate) and can also be applied afterwards on a fabricated device. This is a huge advantage for large-scale production, where the production parameters that ensure optimal printing conditions are not as easily adjusted as in a laboratory. Moreover, since the electronic properties of the functional layers are preserved, an absorption enhancement is expected to directly translate into an increase in efficiency.

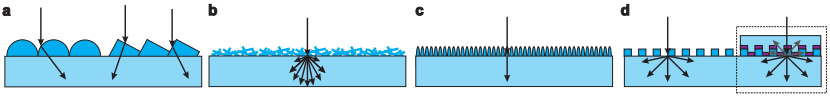

Figure 1.5: Different approaches for external light management. **a** refraction **b** diffusion or haze **c** anti-reflection and **d** diffraction (which works in embedded configuration)

Solutions that belong to the category (e) are illustrated in Fig. 1.5. They embrace front-side dielectric structures, which make use of light-redirection (Fig. 1.5a) and/or scattering (Fig. 1.5b). Another well established approach is the use of anti-reflection structures (Fig. 1.5c) [84], which eliminate surface reflections at the substrate surface (max. 4–6 %). The existing literature on external light management, for which considerable enhancement in device performance has been reported, is listed in Tab. 1.3.

Assessment of light management

For the evaluation of light management solutions, usually the percentage of efficiency enhancement is reported. However, already from the first two entries in Tab. 1.3, it appears that this number is not suited for an appropriate comparison of different enhancement schemes. If the same micro lense array (MLA) is applied to two different solar cells, the enhancement ratio of the device with initially lower PCE is twice than that of the cell with the higher PCE, due to the smaller denominator value of the first. Generally, a device will be much easier to improve, if it does not exhibit a pre-optimized layer thickness [85], and thus the ratio of final PCE to initial PCE can become enormous. In contrast, for a device, which is already optically optimized or which has a much thicker absorber layer, the improvement through engineering of light management solutions to the same degree will be much harder.

Table 1.3: Light management for OPV on the light incident interface

Structure	Enh. [%]	PCE_{ref} [%]	PCE_{LM} [%]	**FoM**	Year	Ref.
Microlens array (MLA)	31.8	2.2	2.9	**5.9**	2012	[68]
	12.9	6.2	7.0	**39.2**	2012	[68]
Retroreflector	19.57	4.6	5.5	**27.2**	2013	[69]
V-groove texture film	8.23	5.8	6.3	**19.1**	2013	[70]
Microlens array (MLA)	14.3	5.6	6.4	**32.8**	2013	[71]
Transparent paper	15 [a]	*N/A*	*N/A*	—	2014	[72]
Deterministic aperiodic nanostructure (DAN)[b]	3.78	8.5	8.8	**26.2**	2014	[73]
Moth-eye structure[b]	3.89	6.4	6.7	**11.2**	2014	[74]
Crystallite capping layer	42.8	4.2	6.0	**64.8**	2016	[75]
Silica nanoparticle arrays[c]	13.46	6.5	7.4	**48.5**	2014	[76]
Alumina nanowires	10.28	8.2	9.0	**68.2**	2015	[77]
Compound parabolc trapper (CPT) [b,d]	6.29	9.4	10.0	**58.7**	2015	[78]
CPT & V-groove texture[b]	10.87	9.4	10.4	**110.3**	2016	[78]
Microlens array (MLA)	10.61	7.7	8.6	**59.9**	2016	[79]
2D-Microstructured scattering layer (MSL)	14.21	7.5	8.6	**79.1**	2016	[80]
Luminescent down-shifting (LDS) Nanocones	13.8	4.0	4.6	**11.8**	2016	[81]
Inverted pyramids	13.0	7.4	8.4	**68.6**	2016	[82]
direct laser interference patterned (DLIP) PET	16.3	6.6	7.7	**64.0**	2016	[83]

[a] for white light illumination under an incident angle range of 60-87°.
[b] These works additionally included plasmonic structures in the active layer to achieve greater enhancements. The reported numbers state only the performance of their surface structure alone.
[c] realized on flexible device. [d] structure not exposed to surface.

In order to assess the potential of a given light management approach, the final power conversion efficiency PCE_{LM} should be considered with a higher weight and the influence of the relative enhancement should be reduced. Hence, in order to provide a more suitable rating for light-management solutions, the following figure of merit (FoM) is proposed and included in Tab. 1.3

$$\mathbf{FoM} = \Delta\mathrm{PCE} \cdot (PCE_{LM})^2, \tag{1.1}$$

with $\Delta\mathrm{PCE} = PCE_{LM} - PCE_{ref}$.

Notable measurement influences

It has to be noted that there exist several factors that can influence the measured enhancements of the light management solution. Organic solar cells sometimes exhibit a high variance in the measured performance values, which can be caused by layer quality or thickness variations. As will be discussed in Sec. 3.1.3, a statistical evaluation is therefore important to interpret the enhancement factor in order to prevent a comparison of a singular good LM device with a particular bad reference device. Furthermore, also the ratio of illuminated area to the area of the charge collecting electrodes can have an influence on the reported current [69].

These factors are rarely reported in the literature and can strongly influence the measured enhancement. In this thesis, particular attention will be devoted to consider fluctuations in the experiments by increasing the number of devices and to optimize and clearly indicate the measurement conditions and possible influences.

1.3 Aim of the thesis

Despite the advantages of the listed light management approaches, several drabacks may still affect their applicability. Whereas some solutions would clearly interfere with the optimization of the printing processes, other approaches would not be compatible with high-throughput roll-to-roll fabrication or would drastically increase the related costs.

Although external light management solutions have the potential to avoid these issues, a remaining drawback for photovoltaic applications is their vulnerability: with their functional optical interface exposed to air, they are prone to typical outdoor conditions like rain, dust or dirt, which are expected to change their refraction and scattering properties due to an altered refractive index contrast. Furthermore, exposed micro- and nanostructures will suffer abrasion through impacts (scratches) and stress (load), which can be expected

for integrated printed photovoltaic applications.

Aim of this thesis is, to develop a light management solution for printed OPVs with the following ultimate properties:

- External – no interference with the PV layer printing.
- Flexible – compatibility with roll-to-roll PV production.
- Protected – no optical sensitive interface exposed to the outside.
- Adaptable – applicable to different thin film PV devices and conditions.
- Cost-effective – yearly harvested energy gain should exceed cost.

2 Theoretical background

An overview over the theoretical background of organic solar cells is given in the following chapter. Especially the optical absorption in the devices is reviewed, since this is crucial for the understanding and development of the light management solutions of this thesis. The findings are put in context with the working principles of external light management approaches. In the following, dielectric diffractive nanostructures and the theoretical principles that govern their spectral response are eventually discussed.

2.1 Organic solar cells

Organic solar cells are excitonic solar cells, in which light does not directly create free charges, but excite an intermediate state (exciton). Hence, certain aspects are considerably different from conventional solid state photovoltaics and will be shortly summarized in the following.

2.1.1 Organic semiconductors

The central element of organic photovoltaic (OPV) devices is the absorber layer, which is composed of at least two organic semiconductors. These materials are molecules or polymers, based on large backbones of carbon. Their alternating single or double bonds (e.g benzene-rings) give rise to a sp^2 hybridization of the binding electrons. Additionally to the in-plane σ-bonds, the

p-orbitals overlap to form a conjugated system, resulting in delocalized electrons in the π-bonds along the polymer chain. The resulting broad density of states [86–88] can be classified into the highest occupied molecular orbital (HOMO) and the lowest occupied molecular orbital (LUMO), which open up the energy gap of the semiconductor

$$E_g = E_{HOMO} - E_{LUMO}, \tag{2.1}$$

and which will define the onset wavelength of the absorption $\lambda_i \approx 1.24/E_g$.

2.1.2 Device physics

Bulk-heterojunction

As mentioned before, absorbed photons give rise to tightly bound excitons (electron-hole pairs) with binding energies of $E_{ex} \approx 0.3 - 1$eV (grey ellipse in Figure 2.1a) [38, 89, 90]. Since this energy is too large for an electric field to dissociate the excitons in OPVs, they need a junction between two semiconductors with different energy levels, the (electron-) acceptor and (electron-) donor, respectively (see Figure 2.1a). At their interface, it will be energetically more favorable for the exciton to transfer the electron to the acceptor with the lower LUMO level, while the hole will stay on the donor (charge transfer (CT) state). From this CT state the electron-hole pair will either recombine or dissociate into free carriers. Since the conversion into free charges must thus take place at the interface of the two semiconductors, a first proposal of a planar junction by C.W. Tang in 1986 [91] was later replaced by the much more successful concept of a bulk-heterojunction (BHJ) [92–94], as shown in Figure 2.1c.

Internal field

Once the exciton is dissociated, the driving force towards the contacts is given by the internal voltage, which is related to the chemical potential $\mu = eV_{int}$. Only recently an analytical model could relate V_{int} to the externally applied voltage by a transport related term

$$V_{ext} = V_{int} + J \cdot R_{tr}, \tag{2.2}$$

where the transport resistance $R_{tr} \propto d/\mu_{eff}$ scales with the layer thickness d and is inverse proportional to the effective mobility $\mu_{eff} = \sqrt{\mu_e \mu_h}$ of electrons and holes [95]. The internal field can be best studied if the photocurrent J is zero and hence $V_{ext} = V_{int} = V_{OC}$ (Fig. 2.1b). At this open circuit voltage, recombination and charge-carrier generation rates counterbalance each other

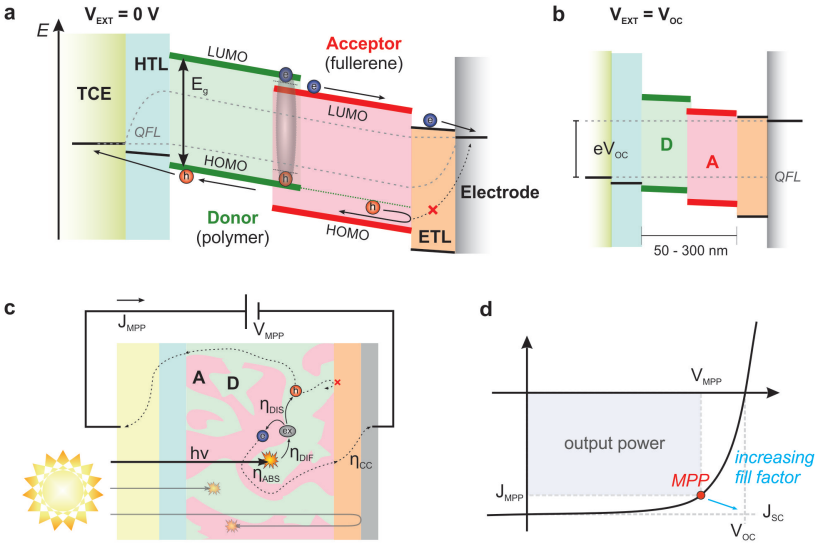

Figure 2.1: Charge generation in an organic solar cell. **a** Energy levels of a device (absorber + transport layers + electrodes) under illumination at zero bias. Absorbed photons create excitons (grey ellipse), which can be dissociated at the interface of the two blended seminconductors. An internal field acts as driving force for electrons and holes and moves them towards the charge collecting electrodes. **b** At open circuit, the applied voltage V_{OC} compensates the internal field and no current is flowing. **c** A geometrical crossection at $0 < V_{ext} = V_{MPP} < V_{OC}$ visualizes the different stations in the charge conversion process: absorption η_{ABS}, exciton diffusion η_{DIF}, exciton dissociation η_{DIS} and charge collection η_{CC}. **d** The generated power is defined by the product $V_{MPP} \cdot J_{MPP}$, which can be determined by the current voltage characteristic of the solar cell under standardized reference illumination.

and no net current is flowing [88]. Generally, the chemical potential and thus the internal voltage is determined by the splitting of the quasi-Fermi energy levels ($\mathrm{QFL}_{e,h}$) of electrons and holes, which at open circuit conditions are defined by the work functions of the electrodes (dotted lines). In case of negative photocurrents ($V_{ext} < V_{OC}$, see Fig 2.1d), generated charges accumulate in the absorber layer due to the low mobilities. The increased splitting of the QFLs give rise to an internal voltage that is higher than the voltage measured at the contacts V_{ext}, which according to Eq. (2.2) is reduced by JR_{tr} [95, 96].

Photon-to-charge conversion

For device operation, a maximum power point (MPP) is chosen, where the applied voltage $0 < V_{MPP} < V_{OC}$ enables a current density $J(V)$, which

leads to a maximum output power $P_{out} = J_{MPP}(V_{MPP}) \cdot V_{MPP}$. Under these conditions, the photon-to-charge conversion process can be described by a series of events, depicted in Figure 2.1c, which are each represented by an efficiency η:

- ▷ $\eta_{ABS}(\lambda)$ - Describes the percentage of absorbed photons (generated excitons) with respect to the number of incident photons for each wavelength. This is the most important term for this work and will be analyzed in more detail in section 2.2.
- ▷ η_{DIF} - Describes the percentage of created excitons that reach the donor-acceptor interface within their lifetime. It is thus determined by the difference between exciton diffusion length $L_D = \sqrt{D\tau} \approx 10$ nm [89, 97], where $D = e^{-1} k_B T \cdot \mu$ is the diffusion parameter, and the mean domain width of the semiconductor blend.
- ▷ η_{DIS} - Describes the percentage of excitons that can be dissociated into a pair of free charges before they decay from the interface state (charge-transfer state) to the ground state (geminate recombination) [96]
- ▷ η_{CC} - Describes the percentage of dissociated charges that are transported from the interface to the electrodes before they undergo free carrier recombination (at rate γ). It is impeded mostly by moderate mobilities of organic semiconductors and by additional recombination centers (defects, interfaces) or thick layers.

Whereas the absorption $\eta_{ABS}(\lambda)$ is an optical parameter, the other three terms describe the charge transport.

At short circuit condition $V_{ext} = 0$ these contributions can be combined to describe the internal quantum efficiency (IQE), which gives the percentage of extracted charges with respect to the number of absorbed photons

$$\eta_{IQE} = \eta_{DIF} \cdot \eta_{DIS} \cdot \eta_{CC} = \frac{\text{extracted charges}}{\text{absorbed photons}}. \tag{2.3}$$

The product of all four efficiency contributions gives the external quantum efficiency $\eta_{EQE}(\lambda)$, which can be measured experimentally for solar cells (see section 3.1.3). It indicates the ratio of extracted charges to incident photons at a given wavelength:

$$\begin{aligned} \eta_{EQE}(\lambda) &= \frac{\text{extracted charges}}{\text{incident photons}} \\ &= \eta_{ABS}(\lambda) \cdot \eta_{DIF} \cdot \eta_{CC} \cdot \eta_{DIS} \\ &= \eta_{ABS}(\lambda) \cdot \eta_{IQE} \end{aligned} \tag{2.4}$$

The number of incident photons can be calculated from any power density spectrum $S(\lambda)$ by division through the respective photon energy $h\nu = hc/\lambda$. If every extracted charge e contributes to the current, a short-circuit current density J_{SC} can be calculated from $\eta_{EQE}(\lambda)$ and $S(\lambda)$ by

$$J_{SC} = \frac{e}{hc} \int_{\lambda} \underbrace{\eta_{ABS}(\lambda) \cdot \eta_{IQE}}_{\eta_{EQE}} \cdot S(\lambda)\ \lambda\ d\lambda. \tag{2.5}$$

Power conversion efficiency (PCE)

Finally, Figure 2.1d shows the current-voltage characteristics of an organic solar cell (JV-curve) under illumination, with the MPP marked in red. From this measurement the performance of a solar cell is described by its power conversion efficiency

$$\eta_{PCE} = \frac{P_{out}}{P_{inc}} = \frac{V_{MPP} \cdot J_{MPP}}{P_{Inc}}. \tag{2.6}$$

With the introduction of the fill factor FF, which relates the MPP values to the above discussed extreme cases of $V = 0$ and $V = V_{OC}$

$$FF = \frac{V_{MPP} \cdot J_{MPP}}{V_{OC} \cdot J_{SC}}, \tag{2.7}$$

the efficiency can be expressed by the voltage at open circuit V_{OC} and the short circuit current density J_{SC}, which enables a better interpretation of the underlying physics of the device performance.

$$\eta_{PCE} = \frac{V_{OC} \cdot J_{SC} \cdot FF}{P_{inc}}. \tag{2.8}$$

The FF measures how effectively the charges are extracted with increasing externally applied voltage and can be interpretated as a measure for the charge carrier mobilities (higher $\mu_{e,h}$, higher FF [95]) and the recombination rate γ (higher γ, lower FF [98]).

Optimum layer thickness

According to the preceding considerations, large η_{IQE} and J_{SC} for given material parameters (L_D, $\mu_{e,h}$) can be achieved by small domain width (high η_{DIF}). At the same time, accounting for low mobilities in organic blends ($\mu_e \approx 10^{-5}$ and $\mu_h \approx 10^{-3}$ $\mathrm{cm^2V^{-1}s^{-1}}$ for electrons and holes, respectively [8]), the path of free charges to the electrode (Figure 2.1c) should be as short as possible in order to harvest the electrons before recombination (high η_{CC}). Furthermore,

to obtain higher V_{MPP} and FF, according to Eq. (2.2), the transport resistance $R_{tr} \propto d/\mu_{eff}$ should be reduced [96].

Altogether, this implies both a high ordering of the semiconductor phases and thin photoactive layer thicknesses d. However, too thin absorbers in turn will naturally reduce the absorption efficiency η_{ABS} of the device. Consequently, this limits the efficiency of organic photovoltaics (see Introduction) and state-of-the-art devices are typically realized with absorber layers around 100 nm [2, 3, 39, 99, 100]. Furthermore, besides the electrical aspects, also optical restrictions are imposed on the thicknesses of the different OPV layers, which will be analyzed in detail in the next section.

2.2 Optical absorption in OPV

According to Eq. (2.5) one can estimate a maximum J_{SC} for full absorption of all photons with an energy larger than the band gap $hc/\lambda \geq E_g$ and $\eta_{IQE} = 1$. As shown in Fig. 2.2a, this can be approximated already by a $d = 2000$ μm thick slab of a semiconductor blend. If the time-averaged local field intensity $|E(z)|^2 =\propto I(z)$ is modeled for incident sunlight, it is seen to decay exponentially according to the Lambert-Beer law

$$\frac{|E(z)|^2}{|E_0|^2} = \frac{I(z)}{I_0} = \exp(-\alpha \cdot z), \tag{2.9}$$

with the absorption coefficient $\alpha(\lambda) = \frac{4\pi\kappa(\lambda)}{\lambda}$ where $\kappa(\lambda)$ is the extinction coefficient. Neglecting surface reflections almost all light is absorbed and the theoretical EQE for this case (Fig. 2.2a, bottom) shows approximately 100% photon to charge conversion over the entire absorption range.

2.2.1 Functional layers

Besides the absorbing layer, however, additional elements are necessary for a well operating device - most importantly two electrodes to collect the generated current, with at least one being transparent to let the light enter the device. Additionally, charge selective electron transport layer (ETL) and hole transport layer (HTL) have been introduced to suppress recombination at the interfaces of the electrodes (indicated by the red crosses in Figs. 2.1a and 2.1c).

If these thin layers are included in the model (Fig. 2.2b, top), reflections at the new interfaces and light absorption in these functional layers are observed. Since this latter absorption does not contribute to the photocurrent, it leads to a reduced external quantum efficiency (Fig. 2.2b, bottom) and is therefore called parasitic absorption (yellow shaded area).

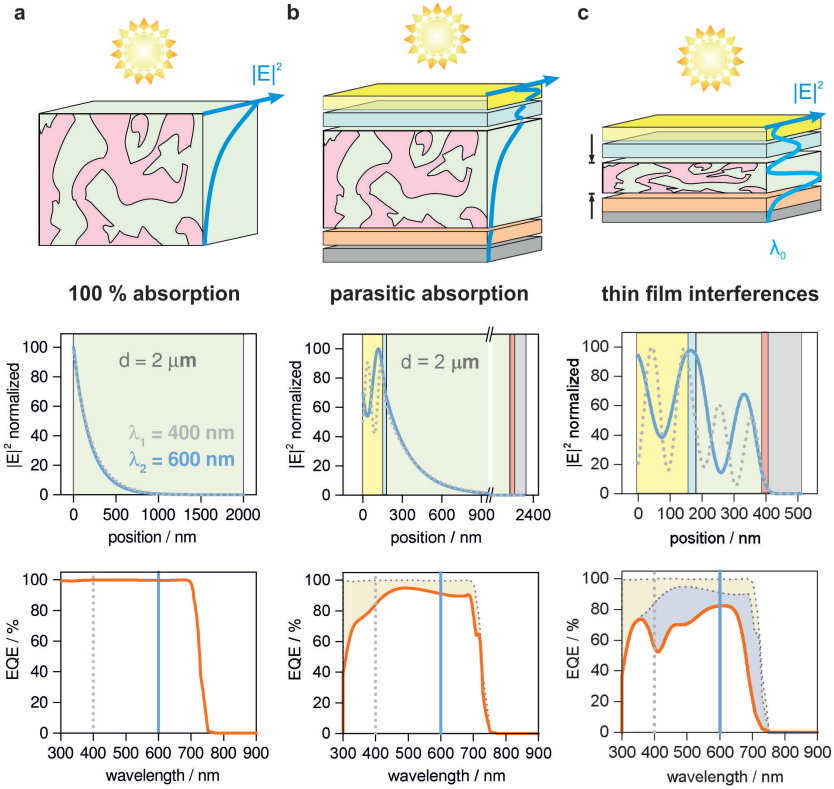

Figure 2.2: From thick layer absorption towards OPV device optics. **a** According to the Lambert-Beer law, an only 2 μm thick slab of active material is able to absorb almost 100% of the incident light (reflections neglected), which with $\eta_{IQE} = 1$ leads to a maximum external quantum efficiency (EQE). **b** Some parasitic absorption is introduced by other functional layers of a photovoltaic device, thus reducing the EQE. **c** Finally, the thickness values of all layers give rise to an interference pattern, which results in position dependent field intensity and consequently further reduced absorption in the active layer.

2.2.2 Thin film interference

These considerations hold for various types of conventional solar cells and have since long dominated the perception of light absorption in PV. However, the fundamental optics change, when the film thickness of the absorber becomes smaller than the coherence length of the incident light and the ray-tracing considerations are no longer valid (see Chap. 4). Light, which experiences multiple reflections at the interfaces inside the layer-stack, interacts with itself and thus gives rise to a complex interference pattern. The resulting time-averaged electric field $|E(z)|^2$ (Figure 2.2c) can only be described in a wave optics picture (see Section 3.2). Furthermore, the absorption in each layer j is defined through integration of $|E(z_j)|^2$, which is governed by the thicknesses of all constituting layers of the stack and their permittivity $\varepsilon(\lambda)$. Consequently, the electric field $|E(z)|^2$ becomes strongly wavelength dependent compared to thick absorbers, which can be seen for the differences in $|E(z)|^2$ for $\lambda = 400$ nm (dotted grey curve) and $\lambda = 600$ nm (blue curve) in Figs. 2.2a-c. This further results in large differences in the EQE at those wavelengths for thin film devices.

2.3 Light management

This wavelength dependency has some important consequences: Even if the optical layer thicknesses are carefully optimized for an ideal $|E(z)|^2$ and a maximum output current, it will always be a compromise among different wavelength regions, i.e. the layer thicknesses that give best constructive interference in the active layer for one wavelength cannot yield the same optimum for other wavelengths.

Consequently, to improve the device performance, it becomes necessary to introduce additional light management structures that are able to influence the optical field distribution in the device. Moreover, a light management solution should exhibit a wavelength dependent optical response to account for a broadband optimization of $|E(z, \lambda)|^2$. With this the light management can be designed to address the enhancement potential in the active layer ant to minimize the optical losses, which are indicated by the blue shaded area in Fig. 2.2c.

In this thesis, dielectric periodic nanostructures are proposed as a light management solution. They are transparent photonic structures that exhibit wavelength dependent diffraction and can thus address the above mentioned field distribution in the active layer, by changing the propagation angle of the light before it enters the thin film stack. It can be even located outside of the device and thus constitutes an external solution, that is usually preferred to interior

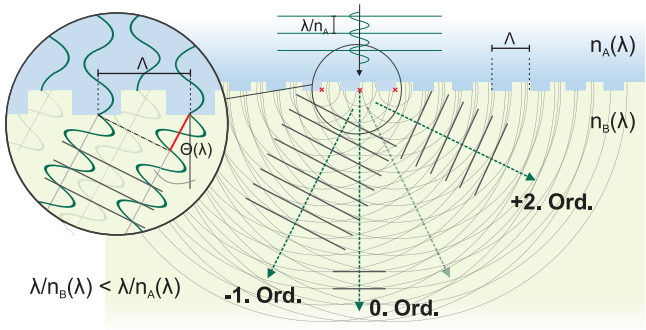

Figure 2.3: Diffraction visualized with the Huygen-Fresnel principle. Upon reaching an interface to a different material, an incident plan wave gives rise to spherical secondary waves. For directions $\theta(\lambda)$ where the optical path of two adjacent secondary waves matches a multiple of their wavelength (phase matching, inset), constructuve interference leads to the formation of a diffraction order which is visible in the far field.

structuring. Moreover, their spectral response can be influenced by engineering their structural parameters, which is why their potential for thin film light management is exploited in the following thesis.

2.4 Diffractive nanostructures

Diffraction

Diffraction is a wave-optics phenomena, which can occur at the interface between two optical media, when the dimension of the objects are in the order of the wavelength of the incident light.

The most prominent example of diffraction is the propagation of monochromatic light through a thin slit. In the far field behind the slit, the illuminated area shows a diffraction pattern that expands over a much wider region than expected from a classical perception of light rays. A periodic array of such slits forms a diffraction grating and corresponds to the structures used in this thesis, which exhibit an interface of periodically alternating materials A and B with refractive indices n_A and n_B, respectively (see Fig. 2.3). Since for the present structures, the extension of their unit cell is below one micron, they will be described in the following as periodic nanostructures in order to avoid confusion with larger period diffraction gratings, which are used since long time for various applications in optics.

2.4.1 Periodic nanostructures

Periodic nanostructures are present in our daily life for instance on DVD or Blue-ray Discs™ and can be recognized by their colorful appearance, which arises from the wavelength dependent diffraction at their structured interface. In order to understand this effect, a monochromatic plane wave $\mathbf{E} = \mathrm{E}_0 \cdot \exp i(\mathbf{kr} - \omega t)$ is considered, which is impinging on the structured interface of two media (Fig. 2.3). The wave propagates in medium A according to the dispersion relation of light, which relates the norm of the wavevector $k = |\mathbf{k}|$ to the the angular frequency $\omega = 2\pi\nu$ and defines its phase velocity v_{ph} and its wavelength in the medium λ_A [101]

$$|\mathbf{k}| = \frac{2\pi n_A}{\lambda} = \frac{n_A \omega}{c}; \quad v_{ph} = \frac{\omega}{|\,\mathbf{k}\,|} = \frac{\lambda}{n_A} \cdot \frac{\omega}{2\pi} = \lambda_A \cdot \nu, \tag{2.10}$$

where $c = 2.998 \cdot 10^8$ m/s is the speed of light and n_A is the index of refraction of medium A. In a medium B with higher refractive index, the light will thus propagate with lower $v_{ph} = c/n$ and will have a shorter wavelength λ_B than in medium A.

The light diffraction produced by a periodic nanostructure is best explained and understood with the classical description of the Huygen-Fresnel principle [102]. Every point of the light's wave-front is origin of a secondary spherical wave, which interferes with all its counterparts. Hence, also at every point of the interface secondary waves will be created (see Fig. 2.3), which, according to Eq. (2.10), exhibit a different λ_B upon propagation in medium B. Since the structure is periodic, for each of these origins there will be a wave at a distance equal to multiples of the period Λ (red crosses), for which constructive interference of the wave-fronts occurs under certain angles. These angles are determined by the condition that the optical path between such a pair of waves has to be a multiple of $\lambda_B = \lambda/n_B$ (see inset of Fig. 2.3). For integers $m = [\ldots -2, -1, 0, 1, 2 \ldots]$ and angles $\theta_m(\lambda)$ the condition

$$\sin(\theta_m(\lambda)) = \frac{m\lambda_B}{\Lambda} = \frac{m\lambda}{\Lambda n_B} \tag{2.11}$$

defines the diffraction orders of the nanostructure in transmission T_m. For arbitrary incident angles $\theta_I \neq 0$ in the plane of Fig. 2.3, Eq. (2.11) transforms into the grating equation

$$\sin(\theta_m(\lambda)) = \frac{1}{n_B}\left(n_A \sin(\theta_I) - \frac{m\lambda}{\Lambda}\right). \tag{2.12}$$

For zeroth order transmission $m = 0$ or flat interfaces $\Lambda \to \infty$, Eq. (2.12) describes only the refraction of light at the interface between the two media,

which is known as Snell's law

$$n_B \sin(\theta_B) = n_A \sin(\theta_I), \tag{2.13}$$

with θ_B being the refracted angle in medium B.

As can be derived from the inset of Fig. 2.3, the diffraction angle described by Eq. (2.12) becomes larger with increasing wavelength, thus for an observer the diffracted white light of every order m is perceived as individual colors (i.e. rainbow).

One dimensional periodicity

A basic nanostructure with a periodicity in $\vec{x}$-direction is a binary (rectangular) line array with a duty cycle (ratio of line width/period) of 0.5 (Fig. 2.4a). Accounting for experimental imperfections, such sharp edges are hardly achievable and can sometime be successfully approximated by a more rounded shape. However, the amount of light that is coupled into each diffraction order is determined by the precise shape of the periodic structure (see Sec 2.4.2) and hence simulations have to be well adapted to the actual fabricated structures in order to obtain good results (see Sec 3.2.2).

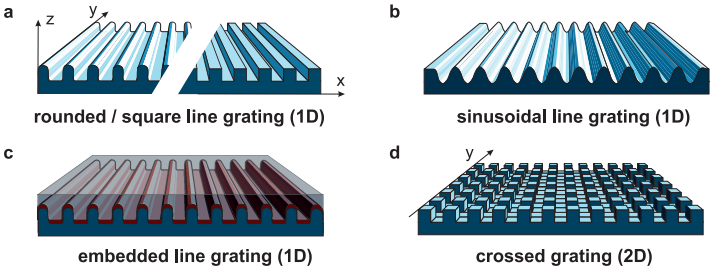

Figure 2.4: Examples of differnet nanostructure geometries used in this thesis. **a** line array with rectangular or rounded edges, **b** sinusoidal lines, **c** embedded line array with rounded edges and **d** two dimensional crossed nanostructure.

If fabrication techniques allow for it, more complex one dimensional shapes can be fabricated - for example a sinusoidal variation of the material along the $\vec{x}$-direction (Fig. 2.4b). Additional variations in depth or duty cycle can be used in order to obtain a diffraction pattern that fits the requirements of the underlying device.

Embedded structures

Besides the variations in the shape, the choice of a surrounding medium with a different refractive index offers another degree of freedom to change the diffraction properties (see Sec 2.4.2). More commonly, in order to preserve a high contrast in the refractive index, a third material with very high or very low n is introduced as a thin coating between the two surrounding materials, as depicted in Fig. 2.4c. If the second method is used, the same material can be used for bottom (substrate) and top (superstrate) material (see Sec. 5.3).

Embedding a nanostructure offers the possibility to have it protected against environmental factors (see Sec. 1.3). With the resulting flat surface it provides the same robustness as a plastic substrate and the diffractive optics of the high index layer inside the film cannot be modified by external factors.

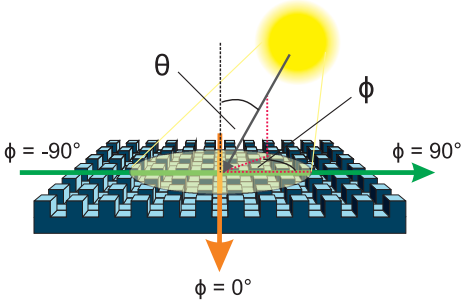

Figure 2.5: Definition of the polar angle (angle of incidence) θ and azimuth angle ϕ of incident light. For one dimensional periodicities the lines are defined parallel to $\phi = 0°$. The angle of incidence θ is always defined with respect to the surface normal.

Two dimensional periodicity

Mostly during a year, the illumination is incident from various directions, which can be described by a polar angle (angle of incidence) θ and an azimuth angle ϕ, which are defined in Fig. 2.5. The azimuth angle is important for nanostructures, which are not rotationally symmetric, and where $\phi = 0°$ is defined parallel to the periodic lines of the previously described nanostructures.

For reasons of a higher independence on irradiation under various angles during the year (daylight movement), crossed nanostructures, which have an additional periodic structure in the $\vec{y}$ direction, are favored for light harvesting (see Fig. 2.5) and are thus investigated in Chap. 5. Equation (2.12), which

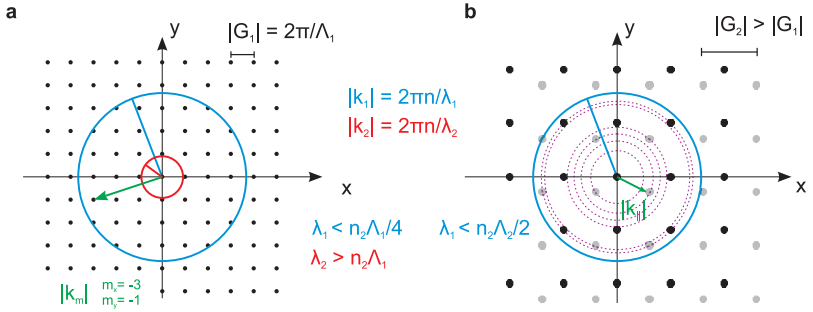

Figure 2.6: Coupling of incident light to transmission orders in reciprocal space. **a** Straight incident light can couple to all propagating diffraction modes in medium 2 within a circle with radius $|\mathbf{k}_0|$. **b** Situation for a smaller period $\Lambda_2 < \Lambda_1$ (grey dots) and for oblique incidence $k_\parallel \neq 0$ (black dots). In the second case, the diffracted light is distributed over even more propagating angles, indicated by the dotted purple lines.

describes the diffraction angles, however, is only valid in the case of one dimensional periodicity and is not sufficient to describe a two dimensional system. If crossed structures are considered, the various waves in medium B can be obtained by their incident wavevector $|\mathbf{k}_I| = (k_z^2 + k_\parallel^2)^{1/2}$ and the grating vectors $|\mathbf{G}| = 2\pi/\Lambda$ for both periodicities. Whereas, the out-of-plane component k_z^2 only undergoes refraction, the in-plane component of the incident wave $k_\parallel$ is extended by $|\mathbf{G}|$ of the respective direction and order. The wavevectors of the diffracted light are then obtained by

$$|\mathbf{k}_{m_x,m_y}| = \left[\left(\frac{n_B}{n_A}\right) k_z^2 + \left(k_\parallel + m_x \frac{2\pi}{\Lambda}\vec{x} + m_y \frac{2\pi}{\Lambda}\vec{y}\right)^2\right]^{1/2}. \tag{2.14}$$

Equation (2.14) can be visualized in the reciprocal space (k-space) [60], which is shown in Figure 2.6a for straight incident light. Every point in the plane refers to a diffraction order in transmission, i.e. one combination of m_x and m_y from Eq. (2.14), separated by the grating vector $\mathbf{G}$. An incident wave defines a circle around the origin with radius $|\mathbf{k}_0| = 2\pi n_B/\lambda$. The incident light, can couple to all orders that lay within this circle and for straight incident light ($k_\parallel = 0$) the onset wavelength for the appearance of the first transmission order ($m = 1$) is defined via

$$|\mathbf{k}_0| \geq 2\pi/\Lambda \quad \text{or} \quad \lambda < n_B\Lambda. \tag{2.15}$$

If the period of the nanostructure is decreased (Fig. 2.6b), this will lead to a larger separation of the transmission orders in k-space $|\mathbf{G}_2| > |\mathbf{G}_1|$ (grey dots) and for a given wavelength, the number of possible diffraction orders is

decreased. Furthermore, for obliquely incident light there will be an additional in-plane momentum $k_{\parallel}$, indicated in Figure 2.6b by the green arrow, which, according to the second term in the square root of Eq. (2.14), leads to a shift of the availible diffraction orders (grey dots) [60].

2.4.2 Diffraction pattern & light management

The dependence of the diffraction properties from the shape of the nanostructure provides one key-advantage of periodic nanostructures for light management. It offers an almost unlimited freedom in the design of light management structures and consequently a high versatility. In contrast to other external light redirection approaches (see Table 1.3), the light distribution behind the diffractive nanostructure can be influenced through its shape for each wavelength.

In Fig. 2.7, this distribution is shown for nanostructures with the same period (700 nm) and duty cycle (0.5) but different shapes corresponding to Fig. 2.4. The emergent angle for different wavelengths is shown as well as the portion of the incident light that is diffracted to the respective order. A comparison of the sinusoidal shape (Fig. 2.7a) with the embedded rounded line nanostructure (Fig. 2.7b) already reveals a huge difference in the almost complementary wavelength dependent first order diffraction T_1. The diffraction pattern of

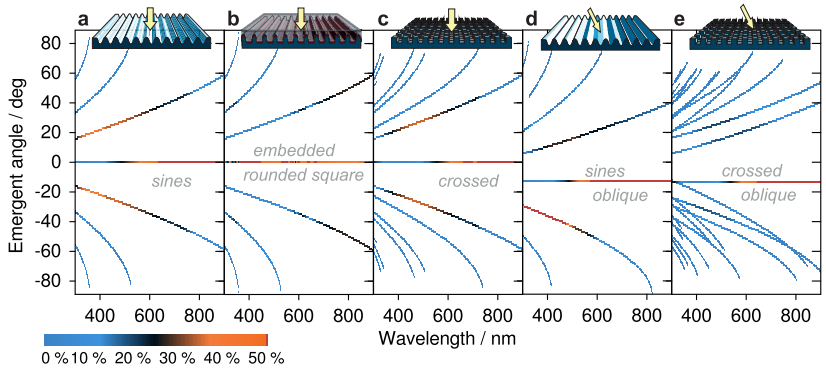

Figure 2.7: Transmitted diffraction pattern of various nanostrucure geometries. The intesity of light that is diffracted into a certain diffraction angle is indicated by the color scale for **a** one dimensional sinusoidal shape, **b** embedded rounded rectangular and **c** rectangular two dimensional crossed. The diffraction pattern changes for oblique illumination for **d** sinesoidal (a) and **e** crossed nanostructures (c) if incident azimuth and polar angle are both set to 20° (see. Fig. 2.5)

a crossed nanostructure (Fig. 2.7c) exhibits additional mixed orders and the light is distributed over more emergent angles than in the one dimensional case.

For a cost-effective light management, the angle dependence is important to optimize the yearly performance (see Chap. 7). Naturally, the diffraction pattern of a given nanostructure will change with respect to straight incidence (Fig. 2.7a and d). In contrast to one dimensional structures, this effect is much more pronounced for crossed nanostructures, as can be seen already from Fig. 2.6b. The large number of transmission orders $|\mathbf{k}_m(\lambda)|$ with different radii in the k-space increases (purple circles through grey dots) corresponds to the number of different emergent angles in the diffraction pattern (see Figs. 2.7e). Especially for planes of incidence that do not coincide with $\vec{x}$ or $\vec{y}$, this leads to a much richer diffraction pattern in terms of emergent angles, which can be used for an angle optimized light redirection.

3

Experimental methods & optical modeling

In the following chapter, the details of the experimental methods used in this thesis are discussed, starting with the fabrication of the solar cells and the light management structures. Secondly, the characterization of both the solar cells (with and without light management) and the nanostructures is introduced, including discussion of uncertainties and error sources in the measurements.

In the second part of this chapter, the simulation models are introduced, which describe the nanostructures (RCWA) and the solar cells (TMM) as well as the combination of both. The latter is thereby handled by a commercial software or by a script developed in this thesis, depending on the nature of the nanostructure.

3.1 Experimental methods

3.1.1 Solar cell fabrication

In order to investigate the effect of the proposed light management solution on the solar cells, the same device architecture and fabrication conditions for multiple devices with and without the light management nanostructures are required. As it will be discussed in the following Chap. 4 the solar cell layer stack, the materials used and the processing conditions were kept the same throughout this thesis.

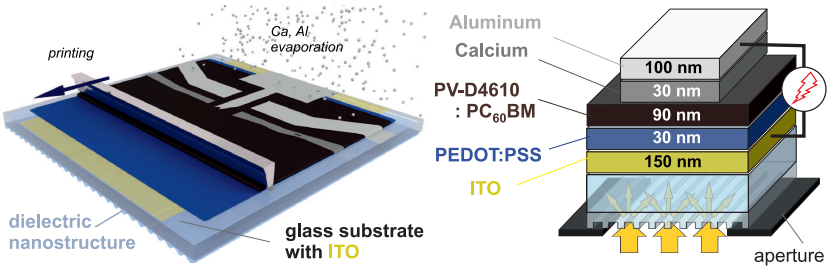

Figure 3.1: Solar cell fabrication. The polymer solutions are deposited onto the ITO-coated substrates with and without light management by doctor blading, followed by an evaporation of the ETL and the electrode, which results in the layer stack described in Sec. 4.1.

All devices are prepared on 2 inch glass substrates, which are pre-coated with a 150 nm layer of indium-tin-oxide (ITO), which is the transparent electrode of the device. In the majority of experiments, the light management structure is additionally attached to the glass substrate on its pristine side, prior to the device fabrication as sketched in Fig. 3.1. The substrate with the ITO side on top is shortly exposed to an ozon plasma, before a 30 nm layer of poly(3,4-ethylenedioxythiophene)/poly(styrene sulfonic acid)(PEDOT:PSS) and the absorber layer are deposited by doctor blading. As absorber ink, the commercial semiconductor polymer lisicon® PV-D4610 (Merck Chemicals) was chosen, blended with $PC_{60}BM$ in a ratio of 2:1 and dissolved in *o*-dichlorobenzene. The choice of the active layer thickness (90 nm) will be discussed in Chap. 4. To ensure that the desired layer thickness is homogeneous over the 2x2 inch substrate, a profilometer scan is carried out to control and adjust the coating parameters. In a last step, Calcium (30 nm) and Aluminum (100 nm) layers are evaporated in a vacuum chamber at a pressure of $\tilde{1}0^{-6}$ mBar with the thicknesses being controlled by a quartz oscillator. The devices that can be characterized independently on each substrate are defined by a shadow mask consisting of eight 3 mm wide fingers. If not stated otherwise the lines of the nanostructures are orientated perpendicular to these fingers (see Fig. 3.1).

3.1.2 Nanostructure fabrication

Periodic nanostructures have the great advantage, that they can be fabricated by laser interference lithography (LIL) [103], an optical method that enables the creation of large-area one- or two-dimensional periodic nanostructures with

different geometries. Sub-micrometer strcutures are already commercially fabricated by this method on square meter areas [104] and periods below 200nm have been reported [105]. Besides direct patterning of large areas, another technique used for the fabrication of up-scalable nanostructures is the replication from a master template. Once created on a sufficiently large area with LIL ,the master can be used for a repeated or continuous embossing of the final material. As this is the technique used in this thesis, the fabrication of the master is shown in Fig. 3.2.

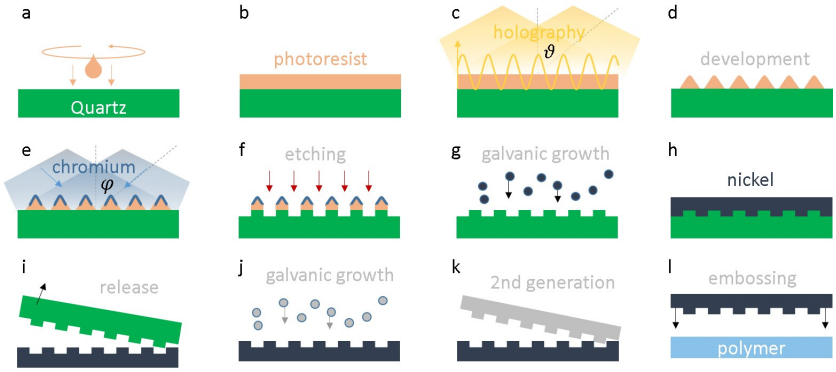

Figure 3.2: Fabrication of periodic nanostructures using laser interference lithography. Two laser beams can generate the sinusoidal interference pattern, which is transferred into photoresist. The resulting periodic structure is modified in depth and ridge width to create a template with the nanostructure (see text for details).

A film of photoresist is coated onto a quartz substrate (a,b) and brought into the LIL setup. Here, a laser is split up into two beams, which are guided through a pinhole and subsequently interfere on the substrate surface under an angle $\pm\vartheta$. Through the periodically varied electromagnetic field strength of the resulting interference pattern, its shape is transferred into the photoresist. The wavelength, the angle ϑ and the exposure time define the precise shape of the structure that results after the development of the (positive or negative) photoresist (d). In a next step, the depth and the duty-cycle (ridge width/period) will be determined. For that purpose, a thin protection layer of chromium is deposited on the part of the structure, which should remain as ridge, which is done by oblique evaporation (e). Through self-shadowing of the photoresist hills, the evaporation angle φ thereby determines the duty cycle of the structure and the desired depth can easily be transferred into the quartz substrate by a successive etching step (f). The final structure is now imprinted in a quartz master, from which next generation masters can be cre-

ated by galvanic growth (g-i). All even generations thereby exhibit the exact shape of the quartz master (j-k), which means that odd number generations are used in the final embossing step (l).

Once the master is created, the replication can be performed by soft- or hot-embossing as shown in Fig. 3.3, whereas the latter is only applicable to thermoformable substrates. In the soft-embossing process the nanostructure master is coated with an anti-adhesive layer and imprinted into an UV-curable polymer (sol-gel) which is dispensed on a transparent substrate (Fig. 3.3a). Exposure with a UV lamp induces the cross linking of the sol-gel monomers and forms a transparent and rigid film, which remains when the master is released. Through the choice of an appropriate sol-gel material, the elasticity and the refractive index can be optimized to best match the properties of the substrate.

For fabrication on plastic substrates, it is more convenient to imprint the nanostructure directly into the material of choice by the hot-embossing technique (Fig. 3.3b). In order to be deformable, the plastic substrate has to be heated slightly above its glass transition temperature. The master is then pressed into the plastic under a load, while the plastic is cooled down and relaxes with a nanostructured surface. Again, the material properties play a crucial role and the choice of the plastic is important for the quality of the structures.

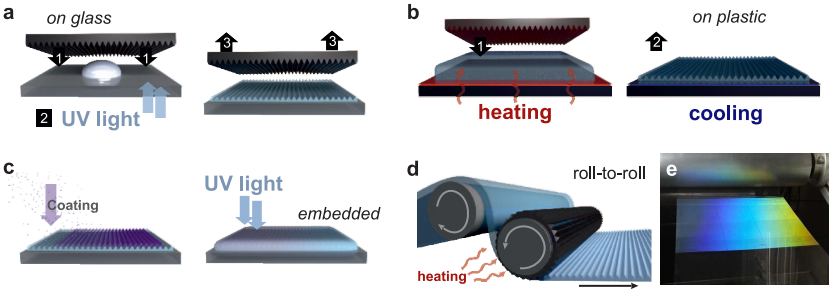

Figure 3.3: Replication of periodic nanostructures on glass and plastic a by using an sol-gel, which is hardened through UV illumination or **b** by hot-embossing into a thermoformable substrate. **c** In a second step, a coating can be evaporated and with a dispension of the UV-polymer the structure can be embedded into the polymer matrix. **d** The hot-embossing technique can be well up-scaled by continous patterning in a roll-to-roll line. **e** Sheets of 500 cm^2 were fabricated for this thesis.

Embedded structures

After the embossing, it is possible to create a burried nanostructure embedded into a polymer matrix. This is done by evaporation of a transparent and high refractive index material (indicated on the left side of Fig. 3.3c), like zinc sulfide (ZnS), on the periodically modulated interface of the molded nanostructure. After the deposition of another layer of the UV-curable polymer, the structure becomes a self-standing, embedded diffractive film.

Up-scalable production

The techniques described above have the potential to be replicated on large area plastic substrates, which fully correlates with the production of printed PV. A thin nickel master of a nanostructure can be bent around a cylinder of a roll-to-roll line (Fig. 3.3d) and enable serial embossing of large area plastic substrates. Fig. 3.3e, shows an 20 cm wide embossed foil with a periodic nanostructure produced by a pilot line, which will be used in Chap. 5.

3.1.3 Solar cell characterization

The efficiency of a solar cell is measured by ramping the externally applied voltage from -1.5 V to 1.5 V under illumination and continuously measuring the generated photocurrent. With the known device area A this is converted into a current density and V_{OC}, J_{SC} and FF are derived from the resulting JV-curve. However, both the incident power P_{inc} and the short-circuit current density J_{SC}, which define the final device efficiency, are dependent on the illumination conditions (Eqs. (2.8) and (2.5)). Hence, for a correct characterization the properties of the light source have to be known exactly. Moreover, in order to compare eith device efficiencies reported in the literature, the measurement conditions and in particular the illumination have to be standardized and carefully controlled during the measurement [106]. Overestimation of device efficiencies upon incorrect measurement is a serious issue in the community of emerging PV technologies [107], since the impact of a publication is often coupled to the reported solar cell efficiency.

Standard test conditions (STC)

For that purpose, a terrestrial reference spectrum (AM1.5G) is given in International Electrotechnical Commission (IEQ) Standard 60904-3 and the American Society for Testing and Materials (ASTM) Standard G173. It is defined as the spectrum that is transmitted through 1.5 times the atmosphere thickness (air-mass $AM = 1.5$, zenith angle of 48.2 ∘) including absorption according to

the 1976 U.S. Standard Atmosphere [108] and is shown in Fig. A.1. A measurement using this spectrum with an integrated power density of 1000 W/m^2 (often referred to as "one sun") at a device temperature of 25° and straight incidence ($\theta = 0°$) defines the standard test conditions (STC) for photovoltaic characterization, which are also applied in this thesis.

A sciencetech SS2.5kW solar simulator equipped with several filters served as the light source exhibiting a high collimation of ±3°. The power density of 1000 W/m^2 was ensured using a calibrated silicon photodiode (by VLSI Standards) at a given measurement distance. The xenon arc lamp was switched on at least 30 minutes prior to a measurement, in order to stabilize the emission. Since nevertheless certain deviation from the reference spectrum is inevitable (see Fig. A.1), a spectral mismatch factor was determined in Appendix A for some measurements. For each substrate, eight devices with an area of $A = 0.04$ cm^2 are defined by a metallic aperture, which is placed above the center of the 3 mm wide metal fingers of the back electrode (Sec. 3.1.1).

Stability

Despite a careful alignement of the sample and the light source, there are several factors that can affect the measured photovoltaic parameters:

1. Changes in device performance with time (degradation) or illumination
2. Dependence on the temperatur of the device
3. Fluctuations in local light intensity
4. Variations of local layer quality and film thickness between devices

The first effect refers to the stability of organic solar cells in general, since several layers of the device are sensitive to humidity or oxidation. The devices thus have to be protected by encapsulation or measurement has to be carried out in nitrogen atmosphere. In the experiments reported in this thesis, a N_2-filled housing is used, which is considered to provide sufficient protection for the duration of the measurement. However, due to the quartz window of the housing ($n \approx 1.5$), a correction factor has to be introduced to account for the additional reflections.

The second effect, leads to a decrease in the open-circuit voltage and in the fill factor after several successive measurements (see Fig. 3.4b). The voltage decrease is attributed to a temperature rise in the sample housing through long term illumination, which is known to affect the V_{OC} [88]. The effect can be reduced when a dwell time of 60 second is kept between two successive measurements.

The third effect can be provoked by the lamp itself, by its power source or by

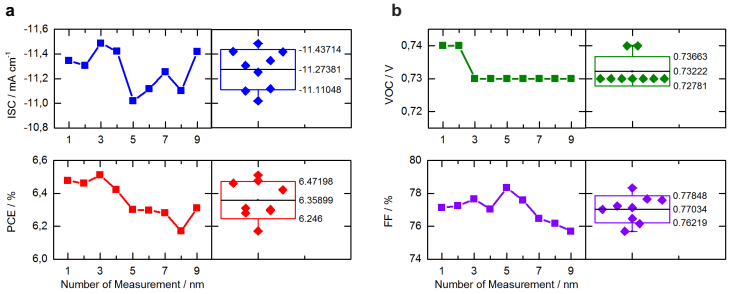

Figure 3.4: Multiple measurements of a reference device were performed under the given test conditions and the main photovoltaic parameters are shown. The standard deviaition σ of these parameters was used to determine an addtional systematic error of the measurement. For the voltage resolution, $\Delta V_{OC} = 0.01$ is larger than σ and hence is set to the same value.

a changed measurement environment, which may introduce additional reflections that alter the light intensity distribution. This error can be estimated by taking the standard deviation σ of multiple measurements of the same solar cell without changing the measurement configuration (see Fig. 3.4).

The fourth effect can be related to minor deviations in the printing and evaporation conditions within one substrate, caused by small local differences in surface energy, ink volume, drying conditions after coating or in the evaporation rate. These variations cause errors, which are partly systematic and partly statistic of nature and which can at best be accessed by a large number of devices. This enables a statistical determination of the average and the variance. Since the evaporation step is limited to four substrates (two with light management, two without) with eight devices each, in each direct comparison 16 devices are compared. If more devices are compared, a second evaporation round could additional yield differences in the metal thickness, which would introduce another uncertainty and thus is avoided if possible.

Angle dependent measurements

To maintain the calibrated power density, for angle dependent measurements, a constant distance to the light source is ensured for all angles of incidence by a home-build holder for the N_2-filled housing. The rotation axis is set to coincide with the plane of the samples, which can be aligned to the axis by a linear stage. The tilt angle of the samples with respect to the illumination direction is however adjusted manually to a scale, which yields an uncertainty of $\pm 0.2°$.

External quantum efficiency

External quantum efficiency (EQE) is measured without white light bias in a N_2-filled glovebox using the light of a xenon lamp passing through a monochromator and guided towards the masked ($A = 0.04$ cm^2) sample through an optical fiber. As a reference for the successive measurement, the wavelength dependent intensity of the monochromatic light is recorded by a calibrated silicon photodiode with a known spectral response. The short circuit current densitiy J_{SC} can be calculated for the measured η_{EQE} and the AM1.5G reference spectrum by Eq. (2.5). As described in Appendix A, a comparison with the values obtained from J-V measurements (see Fig. A.2) can further provide a control for the spectral match of the illumination conditions.

3.1.4 Nanostructure characterization

As mentioned in Sec. 2.4.2, the precise shape of the nanostructure has a strong impact on its diffraction properties, hence, the characterization of the fabricated structures is very important. Verification of the period and depth of the master is usually done by atomic-force-microscopy (AFM), while the shape of a replicated structure is best observed through scanning electron microscopy (SEM). It is possible that due to variations in the shape, the final structure will have a different optimum period and depth than those obtained by the initial simulations. Hence, it might take several iterations of simulation and fabrication until the desired optical properties are obtained. During this optimization step, the simulation model as well as the LIL parameters have to be continuously adjusted.

Diffraction efficiency measurement

With the optical setup shown in Fig. 3.5, the diffraction efficiency of the final nanostructure can be measured and compared to the simulations. The nanostructure is replicated on one half of a glass substrate. Using an index matching gel, a cylindrical lens is attached to the pristine glass backside, which provides a constant out-coupling angle for the diffracted light. The sample is then mounted with the nanostructure facing a collimated light source. In order to measure the wavelength and angle dependent diffraction intensity, both the sample and the light source are rotated in steps of 2° and the transmitted light is collected by a fixed spectrometer. By shifting the lens to the part of the substrate without any nanostructure, a reference measurement $S_{ref}(\lambda)$ can be recorded. The diffraction efficiency for each wavelength λ can thus be calculated. Dividing the measured angle dependent spectrum $S(\theta, \lambda)$ by the

reference (see inset of Fig. 3.5).

For a correct execution, special care has to be taken for the alignment of the setup. Due to the rotational movement during the measurement, one has to make sure that at $\theta = 0°$ the following conditions apply:

- the light source, the center of rotation and the camera are aligned parallel to the same (optical) axis.
- the axis of rotation lays within the plane of the nanostructure and both are orthogonal to the optical axis
- the cylindrical lens is aligned parallel to both the groves of the nanostructure and the rotational axis
- the center of the lens is coinciding with the optical axis to avoid refraction at its surface

The adjustment is performed manually through a set of translation and rotation stages, which induce small measurement errors. Additionally, due to structural imperfections the diffracted light of a single wavelength is distributed over 2-3 angular measurements (see Fig. 3.5). This leads to an underestimation of the diffracted light if only the light under one emergent angle is compared to the reference. Stray light or unwanted reflections can consequently induce further sources of error.

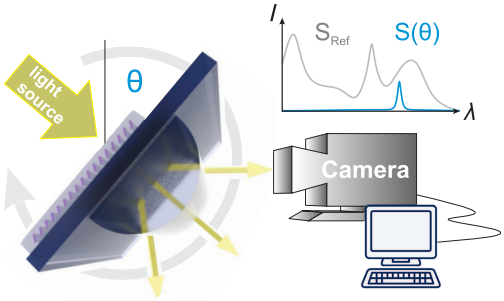

Figure 3.5: Setup for diffraction efficiency measurement. The diffracted spectrum behind the nanostrcutre at each angle $S(\theta)$ is compared to a reference transmission recorded at straight incidence without nanostructure.

To reduce this errors and obtain results that are comparable with the simulations, some post-processing needs to be performed on the data. Firstly, since

the simulation data of emergent angles is symmetric, the efficiencies of positive and negative diffraction orders can be averaged to account for small alignment errors. Secondly, intensities of single wavelengths distributed over adjacent angular measurements, are summed up and assigned to its central emerging angle, which as well provides an increased alignment robustness. Thirdly, in order to provide a clearer comparison with the simulations in Fig. 4.11c, it is accounted for stray light: the recorded data points with an intensity lower than a given threshold are neglected, which is determined by the highest values between the diffraction orders, where no light is expected from diffraction.

3.2 Optical modeling

Since in the present approach, the light management structure is separated from the solar cell layers by a thick (incoherent) and transparent substrate, the optical modeling consists of three separate parts as shown in Fig. 3.7.

(I) The most elementary part is the calculation of surface transmission T^{SF} and reflections R^{SF} for the air interface of material A (which in the case of A = air is redundant).

(II) The second part is the numerical calculation of the wavelength dependent diffraction efficiencies and emergent angles of the nanostructure sandwiched between material A and material B for both reflection and transmission (R, T) and for both directions of incidence (top, bottom).

(III) Finally, the third part is the optical simulation of the solar cell stack, starting with light incident from material B. As for opaque OPV $T^{opv} = 0$, the remaining magnitude of interest (besides the reflection R^{opv}) is the absorption in the absorber layer Abs^{opv}.

After these quantities are calculated separately for various angles of incidence as described in the following Sec. 3.2.1–3.2.3, they can be combined (incoherently) by matrix multiplication (Sec. 3.2.4), accounting for the absorption-free propagation through material A and B.

3.2.1 Surface reflections

Angle dependent reflection and transmission coefficients at the interface between material i and material A are given by the Fresnel-Equations. In case of non-magnetic media these read for s-polarized (TE) and p-polarized (TM)

light respectively [101]

$$r_s = \frac{n_i \cos(\theta_i) - n_A \cos(\theta_A)}{n_i \cos(\theta_i) + n_A \cos(\theta_A)} \qquad t_s = \frac{2n_i \cos(\theta_i)}{n_i \cos(\theta_i) + n_A \cos(\theta_A)}, \tag{3.1}$$

$$r_p = \frac{n_A \cos(\theta_i) - n_e \cos(\theta_A)}{n_A \cos(\theta_i) + n_i \cos(\theta_A)} \qquad t_p = \frac{2n_i \cos(\theta_i)}{n_A \cos(\theta_i) + n_i \cos(\theta_A)}, \tag{3.2}$$

with θ_A defined by θ_i and SNELL's law (Eq. (2.13)) and with the refractive indices, which for our case are $n_i = 1$ and $n_A = n_A(\lambda)$ for air and material A, respectively.

3.2.2 Periodic nanostructures

The amount of light that is diffracted by a periodic array of nanostructures cannot be determined analytically, but necessitates numerical treatment. Since the diffraction of periodic nanostructures depend strongly on their exact shape, screening of various structural parameters demands rapid calculation of a single structure. For this purpose, rigorous coupled wave analysis (RCWA) has proven to be a very powerful method for the optical simulation of periodic structures [109, 110]. Since RCWA makes use of the periodicity of the structure Λ to rigorously solve MAXWELL's equations, its computation speed outperforms other differential (FDTD, FE) and integral (VIE, SIE) numerical methods [111].

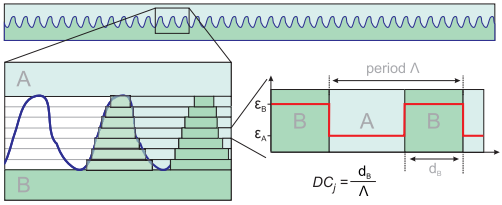

Figure 3.6: Simulation of periodic nanostructures. The periodic variation of the permitiivity is treated seperately for different slices through the structure and approximated by a Fourier expansion of both permittvity and electromagnetic field.

Rigorous coupled wave analysis

In summary, the region that is composed of different materials is divided into slices parallel to the surface (see Fig. 3.6). Since the permittivity in each of

these layers j is periodically modulated, it can be expanded as a Fourier series around an average ε_{avg}

$$\varepsilon_j(x) = \underbrace{[\varepsilon_A \cdot DC_j + \varepsilon_B \cdot (1 - DC_j)]}_{\varepsilon_{avg}} + \sum_{h=1} \varepsilon_h \exp\left(i\frac{2\pi h}{\Lambda}x\right). \tag{3.3}$$

where DC_j is the local duty cycle in layer j (see Fig. 3.6) and ε_h is the hth Fourier component. In order to solve the wave equation for the modulated region

$$\nabla^2 E + (2\pi/\lambda)^2 \varepsilon_j(x) E = 0 \tag{3.4}$$

the field for both polarizations is likewise expressed by a Fourier expansion for the electric and the magnetic field, respectively [110]. The coefficients of $S_i(z)$ and $U_i(z)$ can then be determined by the boundary conditions of the fields at the interfaces of all layers in order to satisfy MAXWELL's equations. For a deeper understanding the reader is referred to Ref. [112] and Ref. [110]. In the following, a commercial software based on the RCWA model was used to predict the diffraction efficiencies for a given geometry, supported by a graphical user interface, which was created during this thesis.

3.2.3 Thin film solar cells

As discussed in Sec. 2.2.2, optical waves in organic solar cells can generally be described by the transfer matrix method (TMM), which is described in the following based on the work of Pettersson et al. [113] and Ref. [114].

Transfer matrix method

At every point of the solar cell stack, the electric field is treated as an superposition of left- and rightwards traveling waves. Along the z-direction orthogonal to the layer interfaces this reads

$$\mathbf{E}(z) = \mathbf{E}(z)^+ + \mathbf{E}(z)^- \quad \text{with} \quad \mathbf{E}(z)^\pm = A^\pm \cdot e^{\pm i k_z \cdot z} \tag{3.5}$$

where the amplitudes $A^\pm$ are defined by reflection, transmission and attenuation in the multi-layer system and have to be determined. To account for propagation through the layers, two matrices can be derived - an interface matrix $I_{i,j}$ that accounts for propagation from layer i to j, as defined by the boundary condition of the Maxwell equations (continuity of the tangential components of electric and magnetic field) as well as a propagation matrix L_j (also layer matrix or phase matrix), describing the phase difference that is accumulated while traveling through a layer j with thickness d_j

$$\begin{bmatrix}\mathbf{E}_i^+ \\ \mathbf{E}_i^-\end{bmatrix} = I_{i,j}\begin{bmatrix}\mathbf{E}_j^+ \\ \mathbf{E}_j^-\end{bmatrix} \qquad \text{and} \qquad \begin{bmatrix}\mathbf{E}_{j0}^+ \\ \mathbf{E}_{j0}^-\end{bmatrix} = L_j\begin{bmatrix}\mathbf{E}_{jd}^+ \\ \mathbf{E}_{jd}^-\end{bmatrix} \tag{3.6}$$

with

$$I_{i,j} = \frac{1}{t_{ij}} \begin{bmatrix} 1 & r_{ij} \\ r_{ij} & 1 \end{bmatrix} \qquad \text{and} \qquad L_j = \begin{bmatrix} e^{-i\zeta_j d_j} & 1 \\ 1 & e^{i\zeta_j d_j} \end{bmatrix} \tag{3.7}$$

where r_{ij} and t_{ij} are given by Eqs. (3.1) and (3.2) and $\zeta_j = 2\pi\tilde{n}_j \cos(\theta_j)/\lambda$, with complex index of refraction $\tilde{n}_j$. For propagation through several layers these matrices can be multiplied to obtain a system transfer matrix $\mathbf{S}$. For the simple case of a slab of two layers in air, this would read

$$\begin{bmatrix} \mathbf{E}_0^+ \\ \mathbf{E}_0^- \end{bmatrix} = \underbrace{I_{0,1} L_1 I_{1,2} L_2 I_{2,3}}_{\mathbf{S}} \begin{bmatrix} \mathbf{E}_3^+ \\ \mathbf{E}_3^- \end{bmatrix} \qquad \text{with} \qquad r = \frac{S_{21}}{S_{11}}, \quad t = \frac{1}{S_{11}}, \tag{3.8}$$

being the reflection and transmission coefficients for the full layer system, respectively. The same approach can be applied to only part of the layer stack in order to obtain the left and right propagating electric field within a layer j [113]. With the respective reflection and transmission coefficients of the two sub-parts, the spatial electric field profile can be determined and $|\mathbf{E}|^2$ can be calculated, as shown in Sec. 2.2, Fig. 2.2c.

Absorption in the active layer

The spatial energy dissipation $Q_j(z)$ of the electromagnetic field, which is proportional to $|\mathbf{E}|^2$ and defines the number of created excitons in layer j, can be calculated as

$$Q_j(z) = \frac{1}{2} c\epsilon_0 \alpha n_j |E_j(z)|^2 = \frac{\alpha n_j}{2\eta_0} |E_j(z)|^2 \tag{3.9}$$

where ϵ_0 is the vacuum permeability and $\eta_0 = 1/c\epsilon_0$ the vacuum impedance. By integration over the extend of the active layer, finally the absorption spectrum can be obtained. By using $\eta_{IQE} = 1$, the external quantum efficiency η_{EQE} can eventually be estimated.

Optical anisotropy

Although the above described one-dimensional model can be extended for oblique incident light [115–117], it still assumes optical isotropic materials. However, many organic materials show anisotropy [118, 119], which means that their dielectric function will change for oblique light propagation. Besides changes in the absorption coefficient between light propagating in-plane $\alpha^{\parallel}$ and out-of-plane $\alpha^{\perp}$, anisotropy will give rise to an error in the accumulates phase in layer j.

This error was reported to be proportional to the optical path and the difference in the refractive indices $\delta \propto (d_j/\lambda) \cdot (n_j^{\parallel} - n_j^{\perp})$ [120]. It is thus expected to have only minor effects for thin film devices with $d_j < 100$ nm and $\lambda > 400$ nm. Since despite large internal propagation angles, good agreement with the experimental enhancement is obtained by this model, this assumption is considered acceptable for the devices used in this thesis.

3.2.4 Combination of RCWA and TMM

Commercial software: setfos

A combination of the various optical systems can be obtained by the use of the commercial TMM software setfos by FLUXiM, which is dedicated to the simulation of thin film optoelectronic devices and offers the possibility to integrate a diffractive (or scattering) interface (II in Fig. 3.7). This interface, represented by a bidirectional scattering distribution functions (BSDF) has to be located between (thick) layers, which are treated incoherently by the software [121]. This condition is fulfilled for the structures investigated in this thesis. The BSDF(λ,θ_{in},θ_{out}) thereby provides the portion of light that is redirected into each emergent angle for every wavelength and incident angle. The resolution thereby is usually set to $\Delta\lambda = 1$ nm and $\Delta\theta = 2$ degree, respectively.

To create the BSDF of a given nanostructure, a Matlab based program performs the RCWA calculations for 45 incident and emergent angles and for both directions of incidence (top and bottom) and stores the results in a text file, which can be imported into setfos. Finally, the absorption in the OPV with an integrated nanostructure can be calculated and compared to the reference without light management.

Limitations

With this procedure, the screening of various parameters of the nanostructure becomes extremely time-consuming, since for every set of parameters (shape, period, depth, dc, coating) a new BSDF text file has to be created and fed into the software. Although this can be improved by a repeated execution of the software with a successive exchange of the BSDF file, still a huge number of BSDF has to be created in advance.

A further limitation of this method is given by the fact that setfos does not distinguish between different polarizations in the BSDF, although it considers the polarization in the inherent TMM formalism. Additionally, the BSDF is

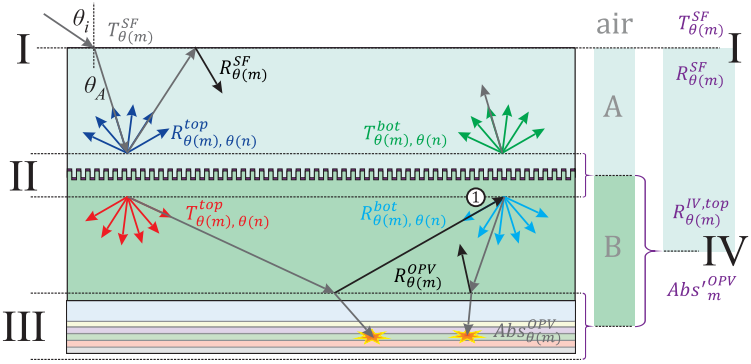

Figure 3.7: Simulation model. The coherently coupled parts (nanostructure and solar cell) are calculated independently and approximated as interface with angle and wavelength dependent reflection and tranmission coefficients. The same can further be done for two incoherently linked interfaces (II and III) to further simplify the problem.

only capable of incident and emergent angles between 0°–90°, and is treated to have rotational symmetry. For light that is incident on simple binary nanostructures (Fig. 2.4a-c) from a plane perpendicular to the nanostructure grooves (planar diffraction; defined by the azimuthal angle $\phi = 0°$), this still delivers correct results, because the diffracted light impinging on the nanostructure from below lays in the same plane (see 1 in Fig. 3.7). However, for conical diffraction as well as for two-dimensional or asymmetric nanostructures as treated in Chap. 5, this model is not anymore valid.

Although for some two dimensional calculations (Chap. 7) it is convenient to use this approach by averaging the BSDF over various (typically 3) azimuth angles ϕ, the general modeling of non-symmetric nanostructures necessitates a 360° simulation of diffracted light. Recently, a new model on optical properties of textured optical sheets (OPTOS) was developed for general light management for solar cells [122–124], which inspired the development of the following alternative model.

Own model

As shown in Fig. 3.7, for every wavelength λ the calculation in each of the above discussed parts yield reflection, transmission or absorption matrices that assign an efficiency to any emergent angle with respect to any incident angle. However, in contrast to a general treatment (OPTOS) the number of possible propagation angles can be drastically reduced due to its diffractive nature [125]. Through the initial incidence of light onto the nanostructure, the allowed

diffraction orders $m = -N \dots N$ (see Fig.2.6) define a set of m possible polar and azimuth propagation angles $[\theta(m), \phi(m)]$ for every λ, which determine the dimension of the calculated matrices: RCWA calculations of part II are performed up to $N = 4$ and hence the resulting 9×9 matrices $(4m + 1)$

$$R^{top}_{\theta(m,\lambda),\lambda}, T^{top}_{\theta(m,\lambda),\lambda}, R^{bot}_{\theta(m,\lambda),\lambda}, T^{bot}_{\theta(m,\lambda),\lambda} \tag{3.10}$$

are sufficient to fully describe the optics of the nanostructure.

Since θ_{in} and θ_{out} are the same for flat interfaces (I and III), they will have only diagonal matrix elements, which are calculated by Eqs. 3.1–3.2 and by setfos, respectively. From the layer thicknesses and permittivies of the OPV stack, the latter is used to calculate

$$R^{opv}_{\theta,\lambda}, Abs^{opv}_{\theta,\lambda} \tag{3.11}$$

for all incident angles in steps of 1°, which serves as a reference table for the entries of the 9×9 matrix, which depend on λ and $[\theta(m), \phi(m)]$ of the respective nanostructure.

By this means, for each interface, polarization and wavelength, a set of matrices is constructed, which subsequently can be used to calculate the optics of the whole system. Since for the connecting media A and B loss-less and incoherent propagation is assumed, this can be done by matrix multiplications[124]. Furthermore, using the Neumann series (geometric series for matrices), an Airy summation [126] can be performed to merge the interfaces II and III, yielding four effective matrices for a virtual interface IV [122]. Since light is incident only from the top on this interface and due to the opaque electrode, this further reduces to only two matrices,

$$R^{IV,top} = R^{top} + T^{bot} \cdot \left[I - R^{opv} \cdot R^{bot} \right]^{-1} \cdot R^{opv} \cdot T^{top} \tag{3.12}$$

$$Abs' = Abs^{opv} \cdot \left[I - R^{bot} \cdot R^{opv} \right]^{-1} \cdot T^{top}, \tag{3.13}$$

with I beeing the 9×9 unity matrix. With this, the problem is reduced to two interfaces (I and IV) that are connected incoherently by a transparent medium A and the final absorption in the photoactive layer Abs'' can be calculated again by using the Neumann series to account for the infinite number of reflections within the two interfaces

$$Abs'' = Abs' \cdot \left[I - R^{SF} \cdot R^{IV,top} \right]^{-1} T^{SF}. \tag{3.14}$$

Validation

The results of this model were compared to those obtained by setfos for an embedded line nanostructure (Fig. 3.8a) and almost perfect agreement was obtained (only small polarization-related effects can bee seen). However, as soon as a two dimensional periodicity is modeled, setfos does not account for the full angular information of the diffracted light and deviations are observed between the models (Fig. 3.8b).

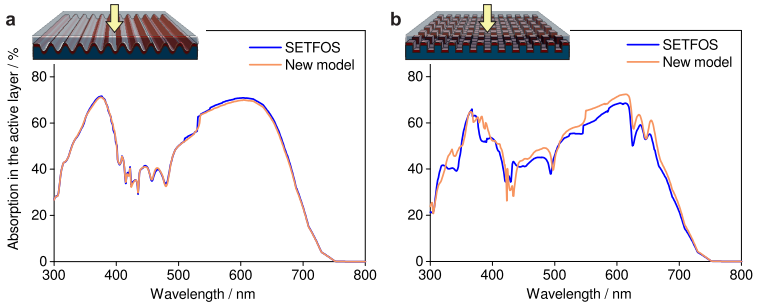

Figure 3.8: Comparisson of setfos with the new model. **a** Good agreement is found for one-dimensional and symmetric embedded nanostructures. **b** For embedded two-dimensional structures deviations are observed even for straight incidence.

Besides the polarization dependent calculation and the consideration of azimuthal angles, the time needed for computation and screening of the nanostructure parameters can be reduced significantly with the new model. In the future, this program could easily be expanded to have a shape optimization routine.

4 Proof of principle

In the first section, a reference stack for organic solar cells is introduced, which serves as basis for following simulations and experiments. Since light redirection at the surface is a very common approach for light management in OPVs (see Sec. 1.2.1), the effects that govern the light-propagation under large internal angles and their influence on the absorption in organic solar cells are reviewed.

In the second section, the experimental validation of external nanostructures for light management is presented. The resulting spectral absorption enhancements are analyzed and related to the diffraction properties of the nanostructures.

4.1 Reference device

In advance of this work a device architecture had to be defined to serve as the basis for computational analysis and for optimization of the nanostructure diffraction. Furthermore, this reference device enables the comparison of various light management configurations.

It is constituted by the following layers (see Fig. 4.2a)

1) A **glass** substrate pre-coated with 150 nm of **ITO** is used as a reliable transparent electrode.

2) Commercial **PEDOT:PSS** (Heraeus Clevios™ P VP AI 4083) was used as the hole transport layer (HTL).

3) A commercial donor polyme (Merck lisicon® **PV-D4610**[1]) was chosen as the absorber, which shows promising up-scaling properties [127]. It is mixed with **$PC_{60}BM$** with ratio (2:1) and dissolved in orthodichlorobenzene (ODCB).

4) **Calcium** is evaporated as electron transport layer (ETL)

5) **Aluminum** is evaporated as opaque back electrode

Optical properties of the used materials

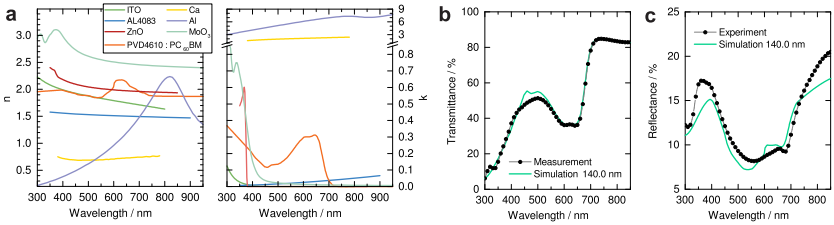

Figure 4.1: Optical properties of the used materials. **a** Real and complex part of the refractive index of the used materials. **b** Transmittance and **c** Reflectance of a 140 nm layer of the absorber blend compared with optical simulations.

For the optical simulations, the software setfos is used (see Sec. 3.2.4). It provides a database for the optical constants of commonly used materials, like standard metals (Al, Ca) as well as various organic and inorganic transport layers like PEDOT:PSS AI4083 or zinc oxide (ZnO), which are all shown in Fig. 4.1a. Additionally, the data for ITO is provided by the supplier of the substrate and MoO_3 was taken[2] from Ref. [128]. The optical properties of the absorber blend were determined by ellipsometry of doctor bladed samples at a project partner and agreed with values obtained on pure PV-D4610 [127] for $\lambda > 450$ nm. The values were further confirmed by comparing the measured transmittance (Fig. 4.1b) and reflectance (Fig. 4.1c) spectra of a dry, 140 nm thick layer of the blend, with the corresponding simulated spectra.

[1] preferably fabricated in the standard configuration, http://www.merck-performance-materials.com/merck-ppf/detailRequest?source=PRONET&docId=201407.288, accessed on 06.12.2016

[2] provided through http://refractiveindex.info/?shelf=main&book=MoO3&page=Lajaunie-%CE%B2, accesed in August 2015

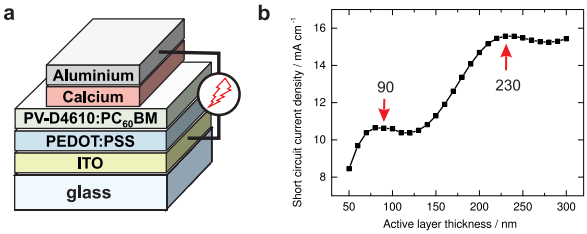

Figure 4.2: Reference device for the light management studies. **a** The standard configuration is preferable for the chosen commercial donor polymer PV-D4610. **b** Its thickness has two performance maxima, from which the thinner layer thickness $d = 90$ nm is chosen.

Active layer thickness

Whereas the thickness of the transport layers (Pedot, Ca) was set to 30 nm (see Sec. 3.1.1), the thickness of the active layer was optimized though optical simulation. Figure 4.2b shows the predicted maximum current density for different absorber thicknesses, which reveal two local maxima at 90 nm and at 230 nm provoked by the interference conditions in the stack (Sec. 2.2.2). Since thinner layers usually exhibit higher fill factors (see Sec. 2.1.2), the first maximum at $d = 90$ nm is chosen. Moreover, the layers with the highest homogeneity over the extend of the substrate were obtained by blade coating of the thinner layer, since a slower blade speed provides a more controlled deposition.

4.2 Angle dependent modeling

In the following, the optical properties of the introduced OPV device are analyzed in detail. As mentioned in Sec. 4.1 the software is used to calculate the absorption in the photoactive layer, when the device is illuminated with the standard sun spectrum (see Fig. A.1). Using Eq. (2.5) with $\eta_{IQE} = 1$ a maximum current density can be predicted for the device. In this section, the dependence of the current generation in the absorber layer with respect to the illumination angle is investigated.

Figure 4.3a shows the simulations of the maximum current density in the active layer as a function of the incident angle θ_I. Upon increasing θ_I, the generated current density likewise increases until the surface reflectance approach unity at very large angles (see Fig. A.3) and thus the absorption and the current in the active layer vanishes. Since a photovoltaic device is always illuminated from air, the highest accessible angle in the glass substrate ($n_S = 1.5$) is re-

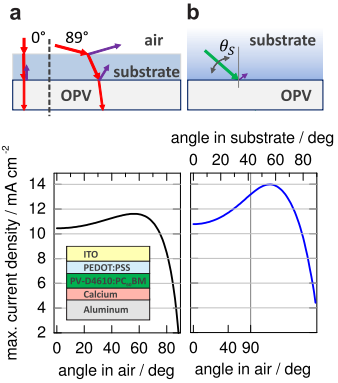

Figure 4.3: Modeling of the generated photocurrent under oblique light propagation in the OPV. a Light incident from air can only access propagating angles below $\theta_S \approx 42°$ in the substrate of the device. The resulting photocurrent increases until high surface reflection leads to a decline. **b** If the light was propagating at larger angles ($\theta_S > 42°$) in the same device, a higher current density could be obtained.

stricted by SNELL's law (Eq. (2.13)) to $\theta_{S,max} = 41.8°$.

However, if a light management structure is applied at the surface, this refraction limit can be overcome and steeper propagation angles in the substrate become accessible ($\theta_S > 41.8°$). Figure 4.3b shows the simulation result for light propagating directly in the substrate, ignoring the angle dependent refraction and reflections at the first interface of the device. The maximum current density value at $\theta_S = 56°$ (14 mA cm^{-2}) is 30% higher than at $\theta_S = 0°$. This emphasizes that it will be desirable to guide light into these steep angles using additional optical structures, as it was proposed by many of the works discussed in Sec. 1.2.1. However, the principles governing this enhancement have not yet been fully analyzed and will be further investigated in the following

4.2.1 Optical path length

In order to explain the strong angle dependent absorption observed in Fig. 4.3b, the enhancement is commonly attributed to an increased optical path length in the absorbing layer [68–71, 73, 76, 77]. In devices that contain a reflective opaque metal back electrode, incident light is assumed to undergo a double pass through the multi-layer structure for straight incidence. If the light is impinging under an angle, the optical path length L in the absorbing layer with thickness d increases from $L_0 = 2d$ to $L_\vartheta = 2d \cdot \cos(\vartheta_A)^{-1}$, where ϑ_A is the propagation angle inside the active layer. In case of a perfectly reflecting

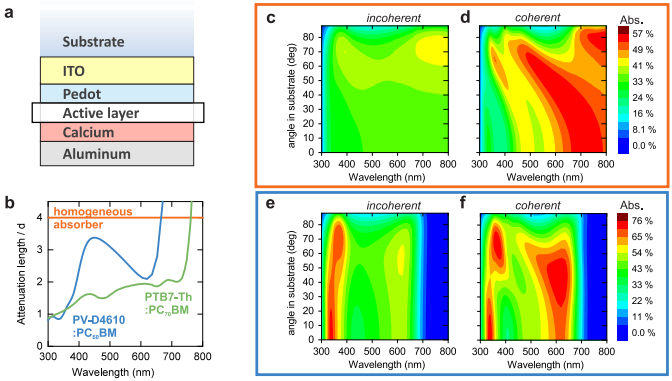

Figure 4.4: Competition of path-length enhancement and thin film interference in the OPV. a Two absorber materials are simulated embedded in the reference stack. **b** Attenuation length of three materials in multiples of the active layer thickness $d = 90$ nm. **c** Absorption in the homogeneous absorber, dependent on the wavelength and the propagation angle θ_S in the substrate, for an incoherent and **d** for a coherent active layer. **e** Absorption in PV-D4610:$PC_{60}BM$ blend in the same device simulated for incoherent and **f** coherent light propagation.

back electrode, the attenuation $Att = 1 - I(L)/I_0$ in an arbitrary thick active layer, mainly caused by absorption, will increase with L according to Eq. (2.9), i.e. the Lambert-Beer law (see Fig. 2.2).

To visualize this effect for an active layer embedded in the solar cell stack (Fig. 4.4a), a fictitious absorber is introduced, which exhibits a wavelength independent attenuation length $\ell_A = 4d$ (Fig. 4.4b) and a constant refractive index of $n = 1.95$. According to Eq. (2.9), $\ell_A = \alpha(\lambda)^{-1}$ is the distance in the medium, after which light is attenuated to $1/e$ of its initial intensity and $d = 90$ nm is the thickness of the active layer. Considering the active layer as incoherent in the software, interference effects are neglected in the transfer matrix calculation. Hence, for increasing angles, only the effect of the enlarged path length is revealed. Figure 4.4c shows the absorption in this modeled active layer at different wavelengths and for all possible angles in the substrate $Abs(\lambda, \theta_S)$. For all wavelengths an increased absorption is observed for enlarged propagation angles, as expected from an enlarged optical light path in the absorbing layer. Although the absorber was modeled to have optical properties that do not depend on the wavelength, a slight dependence is introduced by the other layers of the stack, in which the interference effects are still considered and contribute to the light intensity in the active layer.

If the 90 nm thick absorber layer is treated coherently, interference of trans-

mitted and reflected light in the active layer is taken into account (Fig. 4.4d) and Eq. (2.9) is no longer sufficient to describe the angle dependent absorption. The absorption is not only further increased for all angles (even at straight incidence), but also large differences are obtained for different wavelength regions, despite the constant attenuation length of the modeled absorber. Especially for larger $\theta_S > \theta_{S,max}$ the absorption is dominated by thin film interference effects.

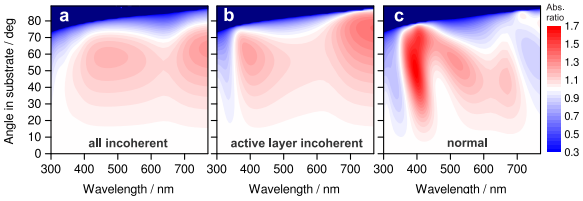

Figure 4.5: Absorbtion ratio with respect to straight light propagation. **a** All layers of the stack are treated incoherently. **b** All thin layers but the active is treted coherently. **c** All thin layers are treted coherently. The absorption enhancement for large propagation angles changes drastically in regions where ℓ_A of the absorber is large.

Intuitively, in the case of PV-D4610:$PC_{60}BM$ the improvements arising from a longer optical path should be stronger at wavelengths for which the absorption is weak (large ℓ_A), and negligible at those, where light is already fully absorbed in one round-trip. If the interference effects are neglected in the whole layer stack (Fig. 4.5a), the enhancement maxima coincide with the maxima in the absorption length (see Fig. 4.4b) following the Lambert-Beer law for an increased path. However, if coherence effects are considered in all layers but the absorber (see Fig. 4.5b), the path length enhancement around $\lambda \approx 500$ nm is compromised by the resulting field distribution.

Finally, if the device is simulated with coherent light propagation in all layers (Fig. 4.5c), the angle dependent absorption changes completely. Steep angles above $\lambda = 700$ nm, where the absorber is weak and consequently the path length theory predicted one of the strongest relative enhancement, are now disadvantageous with respect to straight propagation. Moreover, the shifted maximum suggest an enhancement of 70%, which is much higher than the 38% achievable though path length enhancement only.

Fig. 4.5 directly provides the information whether for an incoming wavelength it is advantageous (red) or disadvantageous (blue) to be diffracted into a specific propagation angle θ_S. Furthermore, once this ratio is calculated for a given thin film PV device, it can be used to define an upper limit of the ab-

sorption enhancement: if the highest value is chosen for every λ, the integral will yield the maximum absorption enhancement that is theoretically attainable in a given device through light redirection.

It can be concluded, that in all cases a larger propagation angle enhances the overall absorption. However, the increased path-length which is usually attributed for this enhancement plays only a minor role in the case of thin film solar cell. Although the path of the light in the active layer is indeed enhanced by a factor $1/\cos(\vartheta_A)$ (Fig. 4.5a), which is known to be a dominant enhancement mechanism in classical weak absorbing silicon solar cells [129], its contribution is outbalanced by interference effects that dominate the field distribution in the active layer and thus the overall enhancement. Consequently, the absorption increase under large angles becomes wavelength dependent (see Sec. 2.3), which provides an even higher potential for optimization than currently exploited by the wavelength independent light redirection strategies, listed in Tab. 1.3.

4.2.2 Interference effects

Since the above analysis emphasized the importance of interference effects in the OPV stack, more simulations were performed to reveal the effects that govern the spatial distribution of the field in the OPV at different incident angles. In Fig. 4.6a, light propagation inside the substrate and the OPV stack is sketched. Since the photon absorption rate is proportional to the energy dissipation $Q(z)$, the modulus squared of the electric field $|E(z)|^2$ can be reconstructed with Eq. (3.9), if the material permittivities are known.

Fig. 4.6b shows the angle dependent field $|E(z)|^2$ of both polarizations for two selected wavelengths ($\lambda_1 = 410$ nm and $\lambda_2 = 620$ nm), which are located in the spectral regions of lowest and highest absorption under straight incidence, repectively (see Fig. 4.4f). Upon reflection at the aluminum layer, the light experiences a phase shift of 180°, which leads to destructive interference and a vanishing field intensity at the back electrode and to a field maximum in the adjacent layer.

As discussed in Sec. 2.2.2, the area under $|E(z)|^2$ in the active layer is proportional to the absorbed light. Figure 4.6b shows that, for straight incidence (black curve), the position of the field maxima is much better centered in the active layer in the case of $\lambda_2 = 620$ nm than for $\lambda_1 = 410$, which consequently leads to an absorption of 67% compared to 33% (Fig. 4.6c). With increasing angles the maxima slightly shifts away from the electrode, which can be explained by a combined spatial and temporal shift in the phase difference of incident and reflected light [115]. In the blue wavelength regime, this leads

to a more preferred field distribution for all studied angles and consequently the absorption is enhanced (see Fig. 4.6c). For red light the field amplitude and the absorption increase for $\theta_S = 25°$ and $\theta_S = 50°$, although the maxima shift from the center towards the PEDOT layer. An increase in $|E(x_j)|^2$ is observed in both cases for large angles and is strongest for $\theta_S = 50°$. This is likely caused by changed Fresnel interface reflections at large angles.

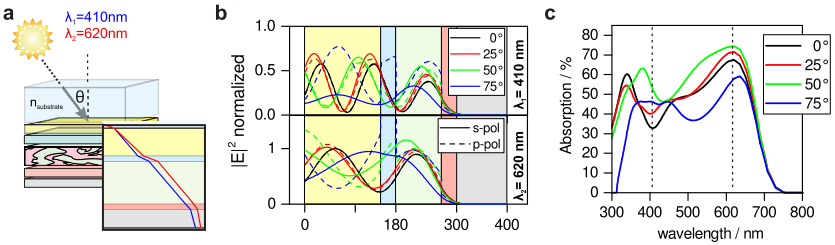

Figure 4.6: Angle dependent field distribution. **a** An increased propagation angle inside the substrate leads to wavelength dependent propagation in the succesive layers. **b** For $\lambda = 410$ nm and for $\lambda = 620$ nm the field distributions in the stack are shown for four angles of incidence. **c** Angle dependent absorption in the active layer, which is either enhanced or decreased for different wavelength regions.

All things considered, the angle dependent current enhancement is originating from the interplay of thin film interference and reflections at the interfaces within the OPV stack. The latter effect provides particularly strong absorption for large propagation angles in the substrate, which are only accessible through the coupling to higher diffraction orders. The first effect introduces an increased wavelength dependence to the absorption. Both effects can be obtained by the design of diffractive nanostructures.

4.2.3 Influence of device architecture

Obviously, if the layer configuration or the materials used are changed, also the interference conditions will be affected and the angular dependent absorption (Fig. 4.4f) will consequently change. To confirm the general applicability of the conclusions drawn above, the same simulations were performed for different device architectures and absorbers.

In Fig. 4.7, three different active material blends are compared: a) the homogeneous absorber from the previous simulation, b) the blend PV-D6410:$PC_{60}BM$ and c) poly [4,8-bis (5-(2-ethylhexyl)thiophen-2-yl) benzo [1,2-b:4,5-b'] di-thio phene-co-3-fluorothieno [3,4-b] thiophene-2-carboxylate] (PTB7-Th) blended

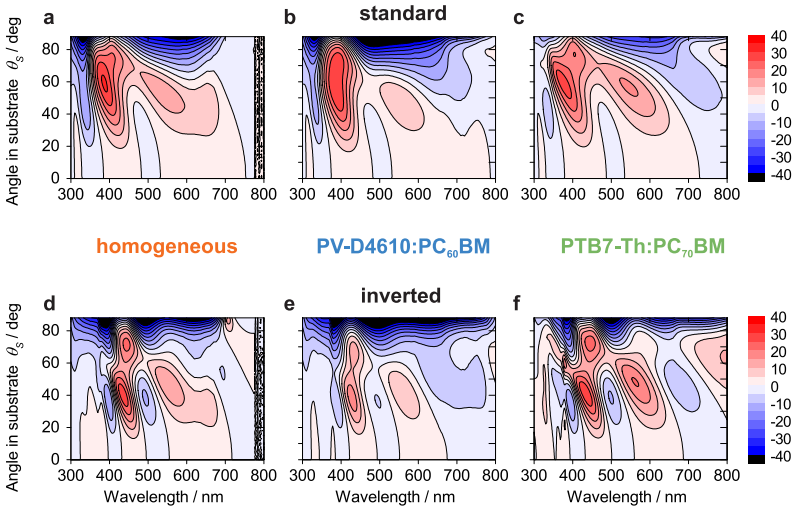

Figure 4.7: Investigation of different absorber materials in two device configurations a-c Angle dependenet absorption spectra in the respective active layer for the standard device configuration and **d-f** for the inverted device configuration.

with $PC_{71}BM$. All three are modeled in two device configurations: standard (see Fig. 4.2) and inverted (glass/ITO/ZnO/Active/PEDOT:PSS/Ag). Figures. 4.7a-c and 4.7d-f show the differences in absorption $\Delta Abs(\lambda, \theta_S)$ with respect to straight propagation $Abs(\lambda, 0)$.

As appears from Fig. 4.7, the angular dependent absorption is rather defined by the layer configuration than by the chosen semiconductor material. The device stack hence mainly determines the angular response of the OPV, since it includes materials, layer thicknesses and consequently the available interference conditions (see Fig. 4.7). Moreover, functions $\Delta Abs(\lambda, \theta_S)$ will be similarly improved by the same light redirection approaches. In conclusion, the efficiency of the device can be enhanced by optical light management independently from the choice of the absorber material. This is especially important for OPV development, since beside optimizing the coating and processing conditions, developing new absorber materials is the most common reason for an advance in efficiency.

4.3 Experimental validation

4.3.1 Optimization of the diffractive nanostructures

Using the simulation methods described in Sec. 3.2.4, an optimization procedure was developed to scan the parameter space for the best performing configuration of a diffractive nanostructure to optimize the device absorption, when it is applied on the light-incident side of the solar cell.

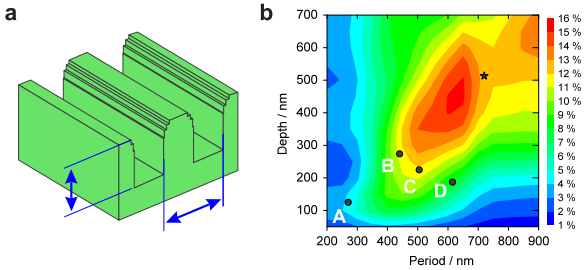

Figure 4.8: Optimization of a nanostructure for the OPV device. a The geometry is chosen to have a rounded rectangular profile for which the period and depth is varied. **b** Color map of the increase in J_{SC} depending on these structural parameters. The black marks indicate the structures, tested in the following.

For a first demonstration, the most simple nanostructure from Fig.2.4, the rectangular line array with equal filling (duty cycle = 50) is chosen for optimization. Since upon replication, the shape is usually slightly altered, a geometry with rounded edges is modeled(see Fig. 4.8a), in agreement with the SEM picture of the final nanostructure (Fig. 4.10a). BSDF functions are created for a range of different nanostructure parameters and included in the TMM software, from which the maximum generated current is obtained for every combination of depth and period. Figure 4.8b shows the absorption enhancement with respect to the reference device, for different period and depth values.

4.3.2 Period dependence

To study the dependence on the period, existing rectangular nanostructures with different periods and depth were tested (see Fig. 4.8b, A-D). For each light management configuration, several devices were fabricated with the nanostructures replicated on the glass side of the ITO substrates. A corresponding number of reference devices was prepared on pristine ITO substrates using the same polymer solutions and evaporation steps. Fig. 4.9a shows the measured

distribution of current densities of the devices, where the boxes frame the 25 and 75 percentile, respectively, while the colored bars indicate the median and the yellow boxes mark the mean value.

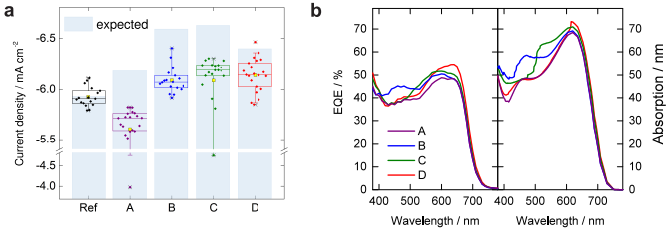

Figure 4.9: Period dependent enhancement. **a** Generated current density for devices with different nanostructures and the expected performance due to simulations (blue bars) with respect to the average value of the reference devices **b** Measured EQE and simulated absorption of the four light management configurations

The enhancement with respect to the reference average value, is indicated by the light blue bars in the background of Fig. 4.9a. Except the small period nanostructure (A), the generated current measured for all devices with nanostructures exceeds that of the reference in average, although their performance stays behind the expectations. As can be seen from Fig. 4.9b, both in experiment and simulations the maximum of the enhancement shifts to larger wavelengths with increasing period .

For a higher enhancement, the simulations of Fig. 4.8 suggest that deeper structures are more favorable, at least for periods $\Lambda > 400$ nm. For this reason, another nanostructure was tested, which is marked by the black star in Fig. 4.8 (depth $d > 500$ nm, period $\Lambda = 720$ nm). An increase in the generated current in the order of 12.7% is predicted for this light management. 21 devices were fabricated with this nanostructure replicated on the OPV surface, while 19 unstructured devices served as a reference.

4.3.3 Efficiency improvement

Figure 4.10a shows a SEM picture of the replicated nanostructure with $\Lambda = 720$ nm. In Fig. 4.10b, the current-voltage characteristics of the two best devices of the two sets are shown. For the device with the light management, a significantly higher current is obtained, while preserving the electronic properties of the solar cell, thus yielding an increase in efficiency from 5.21% to 5.84% (+12%). For all fabricated devices with and without the nanostructure, the

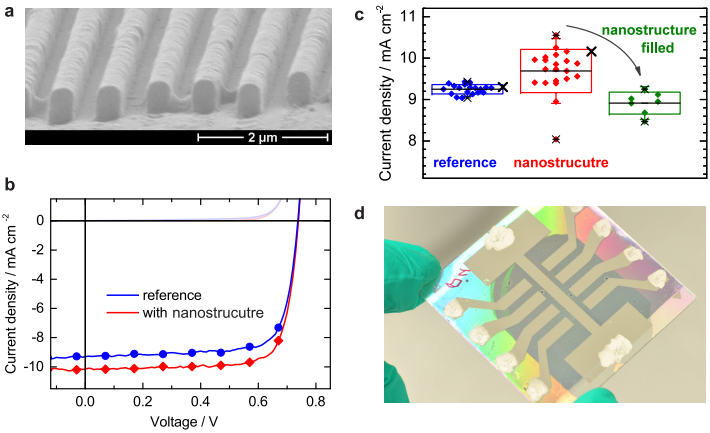

Figure 4.10: Experimental validation of the line nanostructure. **a** SEM picture of the nanostructure at the air-glass interface of the OPV. **b** Current density versus voltage characteristics of the two best devices without (blue) and with (red) the light management. **c** A set of blade-coated devices shows higher average current densities with the nanostructure applied. The boxes denote the standard derivation σ, the outer wiskers indicate 1.5σ and the mean value is highlighted by the black bar. The devices shown in **b** are marked with a black cross. **d** Image of the device: the diffraction properties in the active area are lost, when the nanostructure grooves are filled with another flat sol-gel layer.

current densities are obtained by integration of the measured EQE curves using Eq. (2.5) and are compared in Fig. 4.10c. The two best performing devices, which are plotted in Fig. 4.10b are marked by a cross. The black bars indicate the average current densities: a 4.8% higher value is measured for the light management cells with respect to the reference (Tab.4.1).

Table 4.1: Mean values, standard deviation σ and maximum values for the current densities obtained from EQE measurements for different configurations.

Configuration	reference	light management	filled structure
mean $\pm$ σ [mA cm^{-2}]	9.25 $\pm$ 0.11	9.69 $\pm$ 0.52	8.92 $\pm$ 0.26
max [mA cm^{-2}]	9.43	10.55 (+11.9 %)	9.25 (-14.1%)
number of samples	19	21	7

4.3.4 Spectral analysis

The EQE spectra for the two best devices are shown in Fig. 4.11a. If the difference ΔEQE of the curves is considered (Fig. 4.11b), the impact of the nanostructure can be divided into two spectral regions: a strong increase is obtained in the blue (region **I**), while a broadband enhancement can be observed

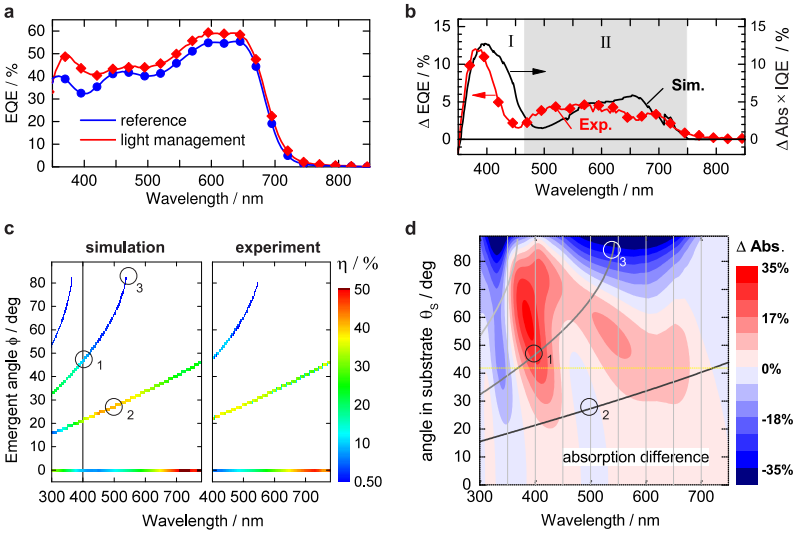

Figure 4.11: Analysis of the absorption enhancement. **a** External quantum efficiency (EQE) spectra of the two devices of Fig. 4.10b without (blue) and with (red) the light management. **b** The experimental values obtained from the EQE spectra (red curve) are compared with the simulated absorption difference (black curve). **c** Simulated and experimental wavelength dependent diffraction efficiencies of the nanostructure. **d** The difference in simulated absorption for different wavelength and angles inside the substrate θ_S reveals areas of improved (red) and decreased (blue) absorption with respect to $\theta_S = 0°$. Overlayed are the angles of the three diffraction orders of the nanostructure as grey lines.

for longer wavelengths (region **II**). To resolve this spectral differences in the EQE, the propagation angle and the diffraction efficiency of the nanostructure are measured by a separate experiment (see Sec. 3.1.4). The measured diffraction efficiency is shown in Fig. 4.11c and compared to the RCWA simulations. In the range, accessible to the measurement ($400 < \lambda < 780$ nm), the diffraction efficiency as well as the emergent angles agree well with the predicted values. As described by Eq. (2.12) the diffracted blue light propagates at smaller angles $\theta_S(\lambda)$ than red light and with different intensities with respect to the incident light. Since also the response of the device is inherently different in different spectral regions (see Fig. 4.4), the measured ΔEQE is strongly wavelength dependent.

In Fig. 4.11 the measured diffraction angles are overlayed onto the wavelength dependent absorption $\Delta Abs(\lambda, \theta_S(\lambda))$. The high values of ΔEQE in region **I** can be well understood by the light that is coupled into the second order

diffraction at angles $\theta_S > \theta_{S,max}$, indicated by position 1 in Figs. 4.11c and 4.11d. At wavelengths $\lambda \approx 500$ nm a lower enhancement is observed because the light is efficiently diffracted into the first order $\eta_{1,-1} > 30\%$, which propagates at angles that do not enable an enhanced absorption (position 2). Finally, in region **II**, where the second order is extinct (position 3), the obtained enhancement can be attributed to the light, which propagates in the first order at angles $\theta_S > 25°$, where the absorption is slightly higher than for $\theta_I = 0$.

The impact of this particular nanostructure on the EQE enhancement in the OPV can hence be well explained when the diffraction and the angle dependent absorption in the active layer are taken into account.

4.3.5 Testing the light management

The contribution of the light-management to the increase in the generated current can be further highlighted, if the diffraction properties of the light management structure are neutralized by a post-treatment. This can be achieved by filling the groves of the nanostructure after the measurement with the same polymer, which is subsequently cured by UV light. As it can be seen from the picture in Fig. 4.10d, the nanostructure and the light diffraction is lost and the nanostructure converts into a thin transparent layer. As consequence, for a particular device equipped with the nanostructure, the current is about 14.1% higher compared to the measurement after this filling procedure.

Influence of the UV-tretament

To confirm that this drop in the current originates from the vanished light diffraction, it was tested, if the UV curing has any additional influence on the observed current. For that purpose, three reference cells are illuminated through their glass substrate and are exposed to the UV light dose (2x 120 sec, $P \approx 15$ mW/cm^2) that is used for cross-linking the sol-gel polymer. The EQE spectrum is measured before and after (Fig. 4.12a). The obtained UV-induced degradation reveals a decrease in the measured currents of ≈3.7% in average.

However, in this experiment, an additional layer of uncured sol-gel was introduced to the treatment, which is expected to absorb a large portion of the UV light. A second experiment was therefore performed to test the impact of a thin sol-gel layer. A flat layer of the material is deposited on the glass side of the device and hardened with UV light under nitrogen atmosphere inside the glovebox for 30 seconds. This corresponds to the same dose that was used for the filling of the devices in Fig. 4.10c, which was chosen shorter than for the

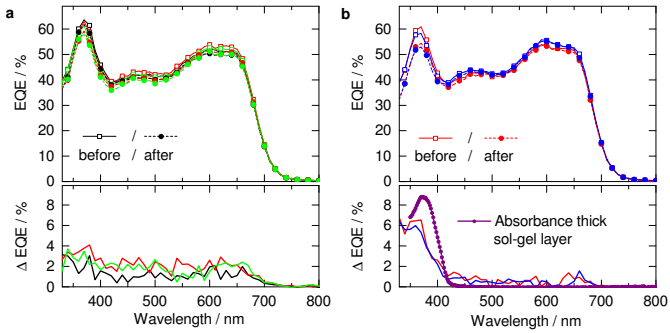

Figure 4.12: Impact of UV treatment on device performance. a An UV illumination with the duration of 2 × 120 sec through the substate of three reference devices yields an average degradation of ≈ 3.7% in the EQE. **b** When a sol-gel film is cured on the same surface, the degredation is reduced, owing to the absorption of the additional surface film.

usual curing process in order to prevent the device degradation observed in Fig. 4.12a. Since the treatment leaves many monomers unlinked a difference of ≈ 6% for the EQE curves is observed below $\lambda = 400$ nm, i.e. the region where the sol-gel absorbs. The attribution of this absorption to the additional sol-gel layer is obtained when compared to the measured absorbance of a flat sol-gel layer of comparable thickness on glass, which is exposed to the same UV treatment (purple line in Fig. 4.12b). This can explain the lower currents that are obtained for the filled devices with respect to the references.

These experiments confirm that the nanostructure itself is responsible for the increase in absorption and the resulting photocurrent density. The experimental values are in agreement with the value predicted by the simulations reported in Fig. 4.8b.

PART II

APPLICATIONS

5 Advanced structures

After the the proof of concept introduced in the previous chapter, it will be shown in the following how the application requirements (see Sec. 1.3) can be met by the present light management solution. Crossed nanostructures, roll-to-roll embossed foil lamination as well as embedment of the nanostructure are investigated to enable a higher angular acceptance, up-scalable fabrication and environmental resistance of the light management, respectively.

Further, it will be also shown that embedded nanostructures can provide additional light trapping, which can be amplified with an asymmetric coating, which is deposited on the nanostructure.

5.1 Crossed nanostructures

In Chap. 4 the performance enhancement was demonstrated under straight incidence, since this is the most common condition used to compare simulations and experiment. However, in the final application, the device will be exposed to continuously changing illumination angles during a solar year (Chap. 7.

If the performance of the device with the nanostructure is modeled for various incident angles (Fig. 5.1a), it is necessary to define the orientation of the plane of incidence with respect to the nanostructure periodicity. Simulations

are thus done for the two extreme cases shown in Fig. 5.1b, which are described by two azimuth directions $\phi = 0°$ and $\phi = 90°$, i.e. for a plane of incidence either perpendicular (planar diffraction) or parallel to the nanostructure lines (conical diffraction), respectively.

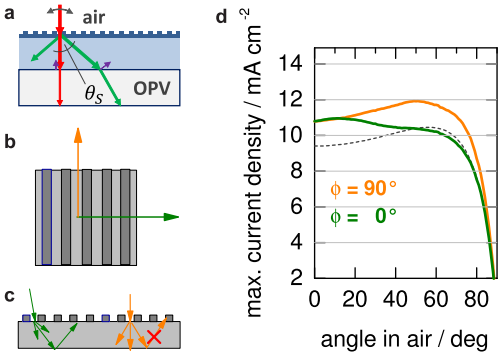

Figure 5.1: Orientation dependence of line nanostructures. **a** The performance of the nanostructure on top of the OPV is not only modeled for straight but also for oblique incidence. **b** For this case at least two azimuth directions have to be distinguished for increasing angles of incidence. **c** In contrast to $\phi = 0°$ the following diffraciton events are not occuring in the same plane of incidence for $\phi = 90°$, which puts a challange to the modeling. **d** Finally the predicted current generation differs strongly for the two azimuth directions for large angles of incidence.

After few ray-optical considerations it becomes clear that the diffraction behavior is inherently different for the two cases: whereas in the case of $\phi = 0°$ the diffracted light propagates always in the same plane (Fig. 5.1c) and higher orders vanish for large incident angles, for conical diffraction, the higher orders exhibit a component perpendicular to the plane of incidence. On the one hand, this makes them more independent on the incident angle but on the other hand this leads to individual azimuth angles for every order, which changes the efficiency of following diffraction events, respectively. Already in this case the simulation with the previously used commercial software becomes difficult and the alternative model of Sec. 3.2.4 has to be applied.

The calculated angle dependent current generation for both cases is shown in Figure 5.1d and compared to the unstructured device (dotted line). As expected, the performance differs strongly between the two azimuth directions, especially when larger angles of incidence are considered. Whereas for straight incidence the current density of both curves is higher than the unstructured substrate (dotted line), the curve for $\phi = 0°$ shows even less current than the reference between $\theta = 50 - 80°$.

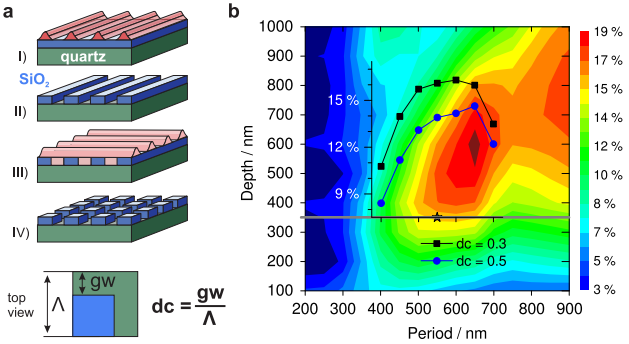

Figure 5.2: Fabrication and optimization of a crossed nanostructure. a The fabrication of a crossed nanostructure is done here in two etching steps and the use of a sacrificial layer of SiO_2 in order to obtain a homogeneous depth. In contrast to line structures, the duty cycle (dc) is hence defined in two directions. **b** Performance of various uniperiodic crossed nanostructures and dc = 0.3. For a depth of $d = 350$ nm as defined by the SiO_2 layer, different duty cycles are tested.

In order to avoid this dependence on the orientation of the nanostructure for oblique illumination, a second perpendicular periodicity can be introduced , which creates a crossed nanostructure. If the same period and duty cycle is chosen, the differences between $\phi = 0°$ and $\phi = 90°$ can be eliminated and only smaller deviations are expected for values of ϕ in between. The fabrication of such structure is done by a repetition of the initial structuring process (Sec. 3.1.2) after a sample rotation of 90°. In order to avoid a double-etching of the quartz substrate in overlapping regions of the two periodicities, a sacrificial SiO_2 layer has to be introduced as shown in Fig. 5.2a. The depth of the resulting structure is thereby limited by the SiO_2 thickness, which in the present case is $d = 350$ nm. It has to be noted that, in contrast to line structures, the duty cycle (dc) for crossed nanostructures is defined here as the ratio of groove width to period (Fig. 5.2a, bottom), for both directions, respectively.

As for the line nanostructures, a variation of period and depth is done in the simulations to obtain the optimal parameters. The results are shown in Fig. 5.2b, which reveal an enhancement of up to 19% for crossed nanostructures with a depth of $d = 600$ nm and a period of $\Lambda = 650$ nm. A value of $\mathrm{dc} = 1 - 1/\sqrt{2} \approx 0.3$ was chosen to ensure an equal volume filling of ridges and groves (see Fig. 5.2a bottom), as it was the case for line nanostructure with dc = 0.5. The dependence on the duty cycle is further modeled for the experimentally realized depth of $d = 350$ nm, which is shown in an overlaid graph for different periods and for dc = 0.3 and 0.5.

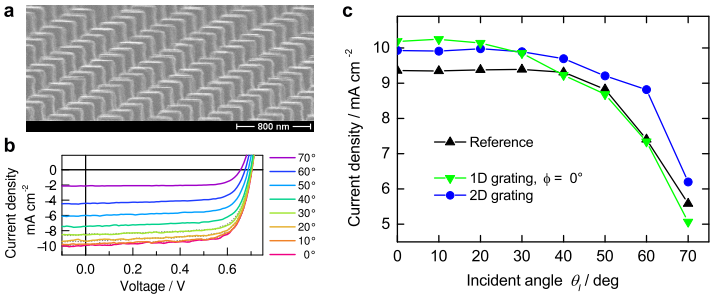

Figure 5.3: Angular dependency of different structure geometries. **a** SEM picture of the crossed nanostructure **b** Angle dependent JV-curves under 1 sun illumination for the device with crossed light management **c** Normalized current densities $J^{\star}_{SC}$ of a reference and of devices equipped with a line and a crossed nanostructure.

A master of the crossed nanostructure is fabricated into the SiO_2 coated substrates with a dc of 0.3 and a period of $\Lambda = 550$ nm, which according to the simulations suggest an enhancement of $\approx 16\%$. A SEM picture of the resulting nanostructure master is shown in Fig. 5.3a. After replication onto the solar cell substrate, angle dependent measurements at standard illumination conditions (1 sun) are performed for the device equipped with the crossed nanostructure for various incident angles. The raw data is shown in Fig.5.3b, from which the short circuit current density J_{SC} is extracted. Since for a tilted device the effective area and hence the power density is reduced by a factor $\cos(\theta)$, the current can be multiplied by this factor to obtain a normalized current density $J^{\star}_{SC}$ [130]. In Fig. 5.3c, $J^{\star}_{SC}$ is compared to corresponding measurements of a reference and a device with a line nanostructure (at $\phi = 0°$).

For the line nanostructure, the resulting angle dependency reveals that the enhancement in the generated current persists only up to $\theta_I = 40°$, where the performance becomes comparable to the device without the light management. Although this is in good agreement with the simulations, both experimental curves are weaker in the performance at higher angles than predicted in Fig. 5.1d, which results in an almost constant current for the reference device. The missing increase in $J^{\star}_{SC}$ for larger angles as observed previously [131] is not fully understood but could arise from differences in the film thickness [132] or from an unbalanced distribution of s and p polarized light [117].

The measurement of the device with the crossed nanostructure reveals a little lower current for straight incidence than the line structure, but it still exceeds the reference aby bout $\approx 6\%$. Moreover, it shows a much broader enhance-

ment, which outperforms the reference for all angles of incidence and yields an enhancement as high as 20% at an angle of $\theta_I = 60°$. Whereas according to Eq. (2.12) the T_{+1} diffraction order of the line nanostructure will start vanishing for $\theta_I > 40°$ and $\lambda > 630$ nm, the crossed nanostructure provides a richer diffraction pattern with more possible diffraction orders at large angles (see Fig. 2.7e). The additional periodicity introduces not-vanishing conical diffraction orders in the direction perpendicular to the incident plane, which is the same effect that enables the better performance for $\phi = 90°$ in Fig. 5.1d.

5.2 Plastic lamination

The light management in Chap. 4 was fabricated onto the photovoltaic substrate by UV nanoimprint lithography. Since glass substrates are used, a sol-gel with a refractive index $n \approx 1.5$ could be chosen, matching well with the glass and thereby minimizing reflections at its interface to the glass (see Eqs. (3.1) and (3.2)). However, high-throughput printed photovoltaics will presumably be fabricated on flexible substrates via roll-to-roll, which necessarily requires also flexible external light-management. In this case, the replication of the nanostructure can be performed by hot-embossing, a technique, which transfers the master structure directly into a plastic film (see Sec. 3.1.2). The light management can then be applied either through a lamination process, through direct patterning of the substrate or even be integrated in the outer barrier foils, which are needed to protect the functional layers from moisture and oxidation.

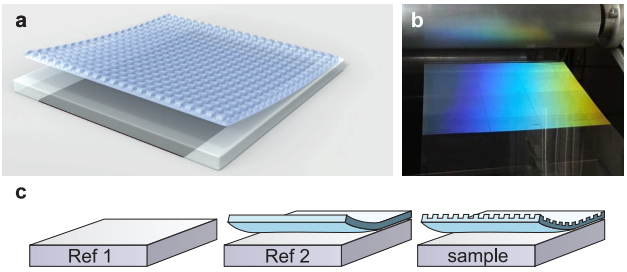

Figure 5.4: Lamination of a light management film. **a** The Motivation is an efficiency enhancing light management film that can be laminated onto a finished PV-device. **b** A sufficiently large master is equipped in a roll-to-roll line and the nanostructure is embossed in a foil. **c** For testing, both pristine and nanostructured foil are laminated onto an OPV substrate for subsequent layer coating.

The lamination approach is shown in Fig. 5.4a. The master for the crossed nanostructure from Sec. 5.1 is up-scaled and used in a pilot roll-to-roll machine

to emboss large sheets of PET, which was coated with an embossable resin. The resulting foils were continuously patterned over an area of 500 cm^2 (see Fig. 5.4b). From these sheets, pieces were cut and laminated onto the glass PV substrate. To rule out any optical effects introduced by this treatment, besides a pristine reference (Ref 1) the resulting devices were additionally compared to a reference (Ref 2), where an unstructured PET film of same thickness was laminated onto the PV substrate (see Fig. 5.4c).

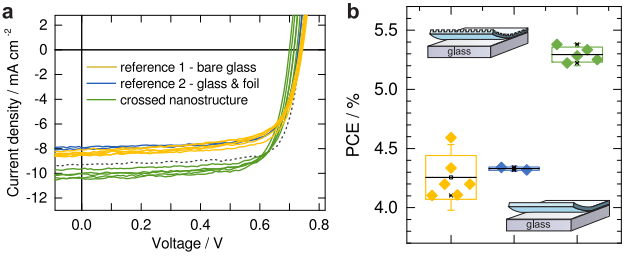

Figure 5.5: Enhancement through a laminated film. **a** The solar cell characteristics reveal a strong efficiency enhancement of the device with the laminated nanostructure, when compared to the reference with bare glass and the reference with the pristine foil. The dotted line shows the reference device of Fig. 4.10b for comparisson. **b** Multiple devices show similar enhancements, when equipped with the laminated crossed nanostructure.

The ITO side of the three substrates were cleaned and the functional layers were deposited by doctor blading. As always, the evaporation of calcium and aluminum was done at the same time for all samples and the resulting devices were characterized under simulated sunlight in respective measurements (Fig. 5.5a). It is observed that both types of reference devices exhibit only currents around 8 mA cm^2, which is less than previous devices of the same architecture (reference from Fig. 4.10b shown as dotted line for comparison). The reference with the applied unstructured plastic film shows little lower currents as expected due to increased reflections, which are due to the mismatch in refractive index at the air-PET surface as well as at the PET-glass interface. If the reference is compared to the device with the nanostructured PET film, a strong increase in the generated current up to 22% is obtained, accompanied by a small reduction in V_{OC}. Although this enhancement is obtained in relation to a rather weak reference, the obtained current density is still 11.6 % higher than the reference from former experiments.

If the efficiency of the devices is extracted and plotted (Fig. 5.5b), an enhancement of the same order as for the current density is observed. The devices with the laminated nanostructure reach an average η_{PCE} of 5.3 % compared to ≈

4.3 % for both reference devices. From this relative increase compared to the laminated unstructured PET film, it can be concluded that the enhancement effects from the previous chapters can be reproduced by the lamination of a light management foil.

5.3 Embedded nanostructures

Besides a better angular acceptance and a flexible and device-independent fabrication, protection from environmental influences is another important requirement for outdoor operation of external light-management strategies. Fine dust or water drops, that accumulate on any air-faced light management will deteriorate its optical properties. Moreover, in applications on portable objects, for which lightweight plastic-based photovoltaics are well suited (see Chap. 1), they are exposed to mechanical stress, scratches and abrasion.

In the following section, it is demonstrated how diffractive nanostructures can be fully embedded into a sol-gel matrix, while maintaining their light management performance. A self-standing diffractive film is created, which is surficial flat and thus enables handling without damage or contamination of the optical nanostructure. Although, an unstructured film does not exhibit any anti-reflection effect as it is provided by wavelength scale surface structures, the embedment introduces further beneficial optical properties. Moreover, as for any other flat (glass) surface, anti-reflection structures [84] can be applied additionally or even imprinted in the outer cladding of the light management film.

The embedded light managent film is fabricated as described in Sec. 2.4.1: the transparent and high index-of-refraction material zinc sulfide (ZnS) is evaporated onto the replicated nanostructure[1] and subsequently covered with another planar sol-gel layer, which is then hardened under UV-light. The underlying periodic nanostructure is thereby transfered into the ZnS coating, which ensures transmitted light of non-zero diffraction orders $\eta^T_{\pm1,\pm2,\ldots}$, propagating at angles $\theta_S(\lambda)$ in the substrate (see Fig. 5.6a). Whereas $\theta_S(\lambda)$ still depends on the period Λ of the initial nanostructure, the amount of light coupled to a diffraction order at a certain wavelength is controlled by the material and shape of the coating and can hence be widely adapted to a given device type. Furthermore, if the evaporation angle is oblique, an asymmetry is introduced to the coating through self-shadowing of the previously molded pattern [133].

[1] A SEM picture of the lorentzian line shape nanostructure is shown in Chap. 6, Fig. 6.3

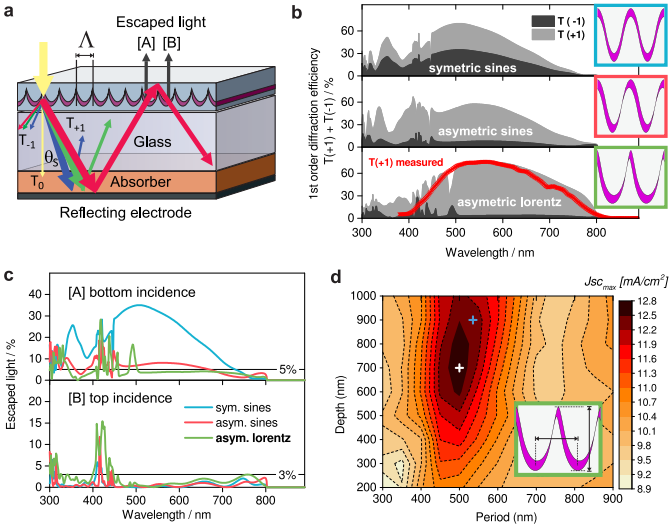

Figure 5.6: Design of the embedded photonic nanostructure. **a** Sketch of the light path in the device with an embedded diffractive film. For $\Lambda \leq \lambda < n\Lambda$ the transmitted light of the first diffraction order T_{+1} propagates with angle $\theta_S(\lambda) > \theta_{TIR}$ in the substrate and undergoes total internal reflection at the polymer-air interface **b** The sum of positive and negative first transmission orders and their ratio is strongly influenced by the shape of the nanostructure. **c** In contrast to symmetric shapes, the successive escape channels (A and B) can be suppressed with an asymmetric coating. **d** Dependent on period and depth of the nanostructure the structure can be optimized for highest current generation in the solar cell. The white cross marks the maximum, while the light blue cross indicates the structure fabricated in this work.

5.3.1 Optimization of light trapping

In contrast to periodic structures exposed to air, diffracted light of an embedded coating cannot easily escape the device after reflection from the solar cell. For wavelengths $\Lambda \leq \lambda < n\Lambda$ the propagation angle of light of the first diffraction order exceeds the critical angle for total internal reflection θ_{TIR} at the polymer-air interface and light is largely hindered from escaping the device. Instead, it is redirected back onto the diffractive layer and the PV stack as long as it leaves the device through a successive diffraction event ([A] or [B] in Fig. 5.6a).

Fig. 5.6b shows the summed transmission efficiency $\eta^T_{\pm 1}$ of the positive and negative first diffraction order for three nanostructure geometries. Starting with an ZnS coating that symmetrically follows a sines profile, a total efficiency of up to 70% equally split into both orders is obtained. In this case,

however, due to reciprocity, the light will escape the device upon incidence on the nanostructure from below ([A]) as efficient as it is couples to the initial diffraction order (blue curve in Fig. 5.6c). Introducing an asymmetry into the coating gives rise to two effects: on the one hand, the light is diffracted more efficiently into the T_{+1} order than into T_{-1} and, on the other hand, the loss of this light is suppressed at the second diffraction event. The efficiency of this loss is indicated by the red line in Fig. 5.6(c) and corresponds to the light, which after diffraction into T_{+1}, is reflected from the solar cell and escapes by another diffraction when impinging the nanostructure from below ([A] in Fig. 5.6a). For straight incidence, this equals the inverse process for light, which is initially coupled into the weak T_{-1} order (Fig. 5.6b, middle).

This asymmetry of η^T_{+1} and η^T_{-1} can be further enhanced by optimizing the shape of the nanostructure. This is achieved by changing the underlying periodic structure, indicated in Fig. 5.6b (bottom, yielding a lorentzian lineshape) or the ZnS coating parameters,. Through additional variation of period and depth, the nanostructure is optimized to yield the highest current density when applied to the reference device. The fabricated structure slightly deviates from the theoretical maximum and is indicated by the blue cross in Fig. 5.6d. In Fig. 5.6b the measured T_{+1} diffraction efficiency is shown, which reveals a maximum of $\eta^T_{+1} = 75\%$ and an average of $\eta^T_{+1} \approx 60\%$ between 450 nm$< \lambda <$750 nm in good agreement with the simulation. Despite the total amount of light in $T_{\pm 1}$ is increased with respect to both sines shapes, the efficiency η^T_{-1} is further reduced at the same time, which also reduces the loss through the escape path [A] below 5%. For a third diffraction event, the portion of the light diffracted towards the surface ([B] in Fig. 5.6a and 5.6c) remains below 3% for 450 nm $< \lambda <$ 800 nm for all three geometries.

5.3.2 Experimental results

When controlling the thicknesses of the fabricated devices, a value of 130 nm is obtained for the active layer, deviating significantly from the targeted 90 nm. Since this is expected to be the same for all reference and light management devices all simulations in this section were adjusted accordingly, which led to a shift in optimum period Λ i(see Fig. 5.6d) and thus a small offset with respect to the fabricated structure.

Fig. 5.7a shows the electronic characterization of the fabricated devices with and without the light management. An average 10% increase in the short circuit current density J_{SC} of devices with the light management film is obtained with respect to the reference devices. Since other electrical properties of the device remain unchanged (see Tab. 5.1), this leads to a direct translation of the enhancement onto the PCE of the device. The J-V curves of the best solar

cells of each set are shown in Fig. 5.7b, which yield a representative 10.7% increase in PCE, close to the average efficiency enhancement of 10.5%.

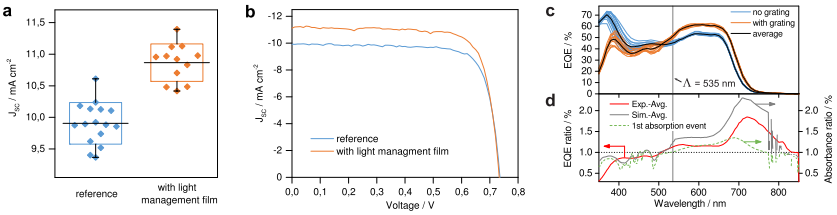

Figure 5.7: Photovoltaic device characterization. **a** Enhanced absorption through the light management film yields an increased short circuit current density J_{SC} compared to the same device on an untreated substrate. **b** The JV-characteristics of the best device of each set reveal that the improvement in the current is directly converted into an enhanced overall output power of the device. **c** External quantum efficiency (EQE) of the solar cells with and without the attached light management layer. The vertical line indicates the nanostructure period $\Lambda = 535\ nm$. **d** Resulting averaged EQE enhancement ratio is in good agreement with the simulated absorption enhancement in the active layer.

Fig. 5.7c shows the EQE for all devices with (orange) and without (blue) the light management layer. The average of the two sets is displayed as black line on top of the curves. A distinct enhancement in EQE is observed for $\lambda \geq \Lambda$, where the diffraction efficiency reaches a maximum and the diffraction angles exceed θ_{TIR} at the surface, which both leads to a more efficient light absorption. The ratio of the two black curves is shown as red line in Fig. 5.7d. It reveals a broadband enhancement starting at around 500 nm and exhibiting a maximum (+85%) close to the band-edge of the photoactive layer at 720 nm, which is in good agreement with the prediction of the optical model (grey curve) even though the measured enhancement is a little lower for $\lambda > \Lambda$.

Table 5.1: Photovoltaic parameters under AM1.5G illumination (100 mW cm^{-2}).

Substrate	V_{OC} **[mV]**	**FF** [%]	J_{SC} **(max)** **[mA cm^{-2}]**	**PCE (max)** [%]
Reference	720 ±10[a)]	76.4 ±1.7	9.9 ±0.5 (10.57)	5.46 ±0.25 (5.70)[b)]
with optical film	730 ±10	75.8 ±2.3	10.8 ±0.46 (11.37)	6.03 ±0.43 (6.31)[b)]
Enhancement			↑9.8% (↑7.5%)	↑10.5% (↑10.7%)

[a)] The stated error is the sum of the standard deviation σ of the sets of 19 and 16 samples for reference and nanostructured substrate, respectively and the systematic error, which is estimated as σ of multiple measurements of the same cell; [b)] Shown in Fig. 5.7b

Using the optical model, it is possible to reveal two enhancement mechanisms of the embedded nanostructure. If only the first diffraction and absorption event is taken into account and all reflected light is neglected, the dotted green curve in Fig. 5.7d is obtained. This situation is comparable to air-faced nanostructures, where no light trapping is present. It matches the experimental data well in regions where the materials absorption is strong and where most of the light is absorbed in one round-trip ($580 < \lambda < 680$ nm), but it is not sufficient to reproduce the enhancement for larger wavelengths. If the successive diffraction events, however, are taken into account, the predicted enhancement increases and shifts towards the band-edge of the absorber (+130% at 710 nm), representing the trapped light in the device. It therefor contributes to the absorption as long as it travels within the geometric extend of the charge collecting electrode area. However, the shape of the electrode was not considered in our model and may be the reason for the lower experimental enhancement in Fig. 5.7d.

5.3.3 Angle dependency

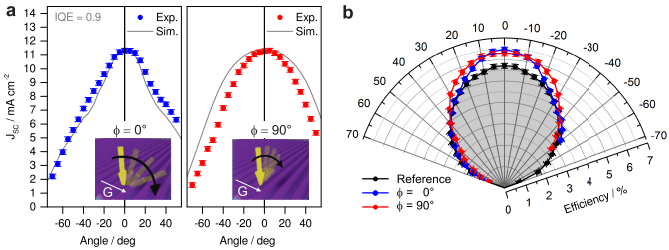

Figure 5.8: Angle dependent performance of the embedded nanostructure. **a** Short circuit current J_{SC} of the device with the light management film, measured for two azimuth angles ϕ with respect to the grating vector G and compared with the respective simulations. **b** Angle dependent efficiency for the two directions under simulated 1 sun illumination, compared to the reference device (shaded).

In order to estimate the impact of the light management for realistic operation conditions, angle dependent JV-measurements were performed in steps of 5 degrees. Fig. 5.8a shows the measured J_{SC} for incident angles in the directions of planar and conical diffraction, respectively. The customized optical model was used to simulate the angle dependent absorption from which a current density is predicted (grey curves in the graphs, $\eta_{IQE} = 0.9$). It is observed, that the simulation matches very well the experimental angular response for $\phi = 0°$, whereas for $\phi = 90°$ the experimental currents are lower than expected for increasing angles. As for the contribution of the trapped

light in Fig. 5.7d, this is attributed to the geometrical design of the device, which has a reflective electrode aligned parallel to the grating vector $\vec{G}$. Large diffraction angles thus redirect the light out of the charge collecting zone and the generated current cannot be extracted in the measurement.

The final power conversion efficiency at various angles of incidence is shown in Fig. 5.8b for both azimuth directions of the light management device and for the reference. It is observed, that along both directions the PCE enhancement through the light management can be kept over $\Delta\theta_{\phi=90^\circ} = \pm 40^\circ$ and $\Delta\theta_{\phi=0^\circ} = \pm 30^\circ$, respectively. This enhancement range is already sufficient to account for the most relevant seasonal sun positions [78] and in Chap. 7 it will be shown, how the yearly harvesting can consequently be enhanced with this structure.

6 Application to optimized devices

In the previous chapter different configurations were successfully tested on the reference device from Sec. 4.1. In the following, the present light management solution will be applied to optimized organic photovoltaic devices of both single-junction and double-junction (tandem) devices of various layer architectures.

In the first part, state-of-the-art devices of standard and inverted architecture are investigated, including experiments on an inverted device with thin ($d < 200$ nm) and thick ($d > 300$ nm) absorber layer. Two light management structures designed in Sec. 4.3.3 and Sec. 5.3 are separately replicated on glass and then attached onto the finished devices.

The second part introduces the tandem structure for solar cells. The light management samples are applied to the encapsulated tandem using an index matching gel, which allows to select the best device as reference and directly compare it with and without the light management.

6.1 Single-junction devices

6.1.1 Different device architectures (simulation)

In order to show the potential impact of diffractive nanostructures, the light management will be tested in the following on the two common device architectures described in Sec. 4.2.3. For that purpose two optimized single-junction devices, which use PTB7-Th as a photoactive material and for which record efficiencies were reported in the literature, are simulated with and without the light management.

Standard & crossed nanostructure

For the standard architecture, the cell reported by Zhang et al. is one of the few OPV devices that reaches an efficiency of 9% in this configuration [2]. Since the ITO thickness was not reported, this parameter was optical optimized in order to assure that the best possible device is considered. With η_{IQE} set to 0.9 and ITO and active layer thickness being 125 nm and 94 nm, respectively, a maximum photocurrent density of 16.6 mA cm^{-2} is obtained, which is reasonable compared to the measured current density of 16.9 mA cm^{-2} (see Tab. 6.1). By optimizing and applying a crossed nanostructure (see Sec. 5.1), the simulated photocurrent in this device can be increased up to 18.8 mA cm^{-2} with a relative enhancement of 12.9%. While the reported cell had an efficiency of 9.0%, this absorption enhancement would thus yield a PCE value exceeding 10%, which would be among the highest values for a single junction solar cell in the standard configuration.

Table 6.1: Comparison of reported and simulated short circuit current densities with and without light management structures.

	Zhang et al. [2] (standard)	Kong et al. [134] (inverted)
Reported J_{SC} [mA cm^{-2}]	16.86	18.40
Reported PCE [%]	9.00 %	9.74 %
Simulated* J_{SC} [mA cm^{-2}] no LM	16.60	18.56
Simulated* J_{SC} [mA cm^{-2}] with LM	18.75	21.37
Simulated Enhancement	+ 12.9 %	+ 15.1 %

* with the assumption of a constant $\eta_{IQE} = 0.9$.

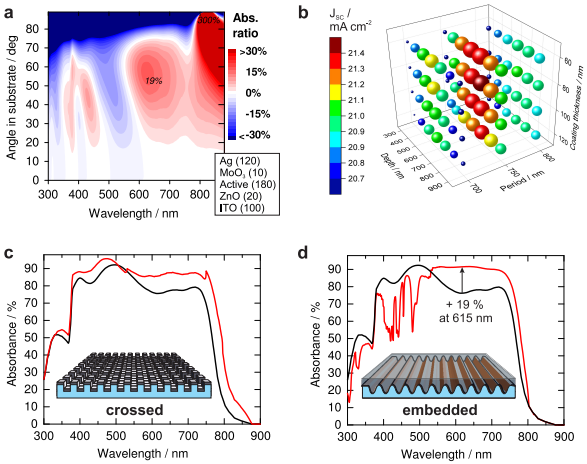

Figure 6.1: Theoretical assessment of light management solutions for an optimized inverted device. **a** The increase or decrease in the absorption is simulated at various incident angles for the stack listed below with thickness in nm. A high potential is observed for oblique light above $\lambda > 550$ nm. **b** Simultaneous variations of period, depth and a MgF_2 coating thickness of a crossed nanostructure for this device yields a maximum absorption increase of 15% in the device (brown ball). **c** The enhancemed in the absorption spectrum with this crossed nanostructure is especially pronounced for large wavelength. **d** Enhancement in this spectral region can also be obtained by an embedded nanostructure with a simulated absorption increase of 8%.

Inverted & crossed nanostructure

For the inverted architecture, a state-of-the art organic solar cell with a reported efficiency of 9.74% was considered [134]. The simulation yields a short circuit current of 18.8 mA cm^{-2}, again comparable to the measured 18.4 mA cm^{-2} using $\eta_{IQE} = 0.9$.As can be seen from the angle dependent simulations in Fig. 6.1a, even for this highly optimized device, it is possible to obtain a performance enhancement above $\lambda > 550$ nm, which can be addressed by the application of a diffractive light-management solution. The crossed nanostructure geometry introduced in Sec. 5.1 was used for parameter optimization to maximize the photocurrent. It is observed, that an over coating with the low index of refraction material magnesium fluoride (MgF_2) as an additional anti-reflection layer can further increase the generated current and a variation of its thickness was included in the optimization routine (see Fig. 6.1a). The simulated absorption efficiency provided by the best nanostructure configuration with respect to the unstructured device is shown in Fig. 6.1b, which translates into a 15.1% higher J_{SC} of 21.4 mA cm^{-2}. Assumed that the electronic properties remain unaltered, as it was the case in the experiments of

previous chapters (see Figs. 4.10b and 5.7b), this enhancement through light management would yield a PCE above 11% (see Tab. 6.1), which has not yet been achieved with this material in a single-junction device.

Inverted & embedded nanostructure

As discussed in Sec. 5.3, embedded light management is highly desirable for outdoor applications of printed photovoltaics and hence a similar light management configuration is tested on the inverted device. Despite the predicted enhancement between 550 nm $< \lambda <$ 750 nm could be fully exploited by an optimized embedded asymmetric nanostructure (Fig. 6.1d), the overall improvement is simulated to be only 8.9% and thus little lower as for the air-faced nanostructure. As discussed in Sec. 5.3 this can partly explained by additional $\approx$4% reflection losses at the cladding surface, which could however be partly addressed by a MgF_2 coating.

6.1.2 Different active layer thicknesses (experimental)

After the application of the light management was investigated theoretically for both optimized device architectures in the preceding section, an experimental validation on an inverted device will be tested in the following. Moreover, the influence of different absorber thicknesses in the reference device will be investigated, which is why a different absorber material is chosen. For that purpose, two structures from the preceding chapters are chosen and replicated on a separate glass, which can then be attached to the device substrate (see Fig. 6.2a).

The recently developed absorber material poly[(5,6-difluoro-2,1,3-benzothiadiazol-4,7-diyl)-alt-(3,3000-di(2-octyldodecyl)-2,20;50,200;500,2000-quaterthiophen-5,5000-diyl)], PffBT4T-2OD, which was introduced by Liu et al. [1] and reported to enable single-junction efficiencies exceeding 10%. Recently, the same group published a record efficiency of 11.7% [5] using a blend of the related polymer PffBT4T-C_9C_{13} and $PC_{71}BM$ dissolved in eco-friendly solvents. Furthermore, a ternary blend of PffBT4T-2OD with both $PC_{71}BM$ and $PC_{61}BM$ reported by Czolk et al. [33] yielded an efficiency above 10% and a remarkable 6.5% on fully printed flexible and semi-transparent devices. Note that the reported devices have active layers with thicknesses larger than 250 nm [1] or even exceeding 350 nm [5, 33] but still exhibit fill factors above 70%. Such high film thicknesses are desirable for up-scalable coating techniques, but were so far considered to be accompanied by losses in the electronic properties originating from a poor charge extraction (see Sec. 2.1.2).

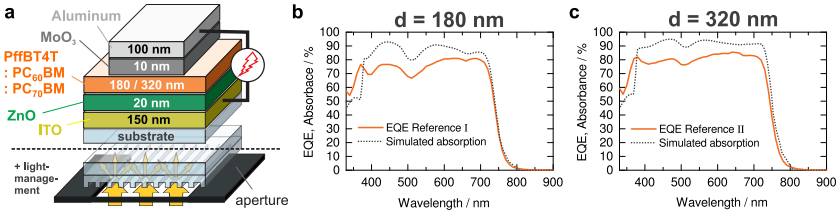

Figure 6.2: High performing devices made from PffBT4T-2OD polymer. **a** Device design with two different active layer thicknesses. **b** The measured EQE is compared to the simulated absorbance for the 180 nm thick and **c** the 320 nm thick active layer.

Devices were fabricated as shown in Fig. 6.2a with two different active layer thicknesses (180 nm and 320 nm). Zinc oxide (ZnO) and the absorber material were spin-coated in N_2-atmosphere to ensure the highest layer quality. The best device for each film thicknesses was selected and compared to simulations in Fig. 6.2b and 6.2c. The simulated absorption agrees with the experimentally measured EQE according to Eq. 2.4, where η_{IQE} slightly increases towards higher λ. As expected, the EQE measurements yield high current densities of 17.9 mA cm^{-2} and 19.7 mA cm^{-2} for the 180 nm and 320 nm thick active layers, respectively (see Tab. 6.2).

Solar characterization of the devices under simulated sunlight yields a power conversion efficiency $> 9\%$ for both active layer thicknesses. However, successive measurements reveal a distinct degradation of these devices, i.e. a decreasing performance with time, which was not observed for previous device configurations. Figure 6.3a depicts the performance versus time, obtained from several measurements of both devices and with the first measurement set to $t = 30$s, respectively.

The two light management samples used in Sec. 4.3.3 (rounded rectangular profile) and in Sec. 5.3 (lorentzian profile) are replicated on a separate glass substrate (see Fig. 6.3b and 6.3c), which are then attached to the respective device as depicted in Fig. 6.2a. Since the devices were not encapsulated, the equipment with the light management structure and its removal had to be done in the glovebox, which introduced a time delay to the preceding and successive measurements. The determined performance of both devices with the attached light management is included as red dots in the time dependent graph of Fig. 6.3a.

In order to assess the effect of the nanostructure with respect to the performance without light management, the preceding measurements were chosen as reference, which are indicated by the grey arrows in Fig. 6.3a. Since a fit to the

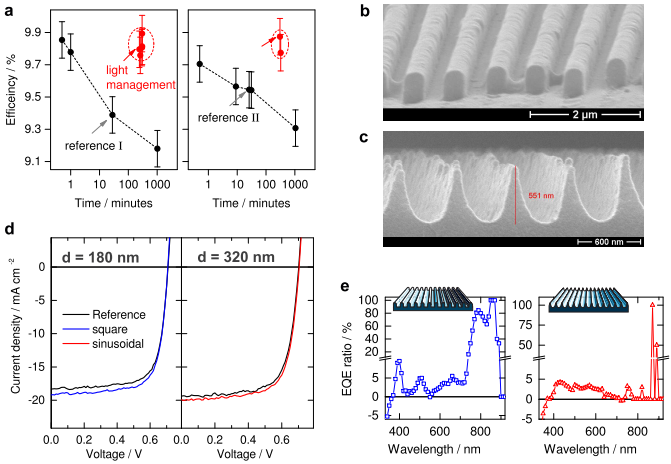

Figure 6.3: Light management experiments on PffBT4T-2OD devices. **a** Since degradation of the devices after the first measurement is observed, the light management is compared to the preceding reference measurement (marked by arrows) to avoid overestimation. **b** SEM pictures of the line and **c** crossed nanostructures from the previous chapters, that are applied on the devices. **d** The efficiency of both devices is enhanced in successive measurements with and without an attached nanostructure. **e** The enhancement ratio of the measured EQE for both device compared with the respective reference device.

time dependent performance of the reference would yield a lower PCE for the reference, this comparison rather underestimates the obtained enhancement. The photovoltaic parameter of this reference and the respective light management measurement (red arrow in Fig. 6.3a) are obtained from the JV-curves shown in Fig. 6.3d and are listed in Tab.6.2.

Table 6.2: Improvements obtained on optimized single-junction devices.

Device	η_{PCE} ⋆ [%]	J_{SC} ⋆ [mA cm^{-2}]	V_{OC} [mV]	FF [%]	EQE [mA cm^{-2}]
Reference I (180 nm)	9.39	-18.32	710	72.2	17.88
+ rectangular LM	9.80	-18.73	720	72.6	18.61
	+4.3 %	+2.2 %	+1.4 %	+0.6 %	+4.1 %
Reference II (320 nm)	9.55	-19.40	700	70.3	19.34
+ lorentzian LM	9.87	-19.92	700	70.8	19.68
	+3.4 %	+2.7 %	+0.0 %	+0.7 %	+1.8 %

⋆ no spectral mismatch calculation; errors are ±0.11 and ± 0.16 for η_{PCE} and J_{SC}, respectively (see Sec.3.1.3).

Finally, the external quantum efficiency was determined in the glovebox and the spectral enhancement for both structures is shown in Fig. 6.3e. In particular, the rectangular nanostructure on the thinner cell can enhance the absorption in the weak absorbing regime ($\lambda > 700$) much more successful than the lorentzian nanostructure on the thick cell. Note that, the performance in the visible is comparable for both cases.

6.2 Tandem devices

While record efficiencies in single-junction cells have recently reached 11% (see Tab. 1.2), the tandem concept has the potential to theoretically double this value [41], which originates from

1. the summation of operating voltage of the series-connected subcells
2. a complementary and thus wider spectral coverage and a reduction of thermalization losses (in the case of hetero tandems [135, 136])
3. a higher optical density (in the case of homo tandems [137, 138]).

In particular the latter concept of two absorbers of the same material, enables a more effective charge extraction by using thinner layers in each junction, while exhibiting an optical density that is comparable to that of a single thick active layer.

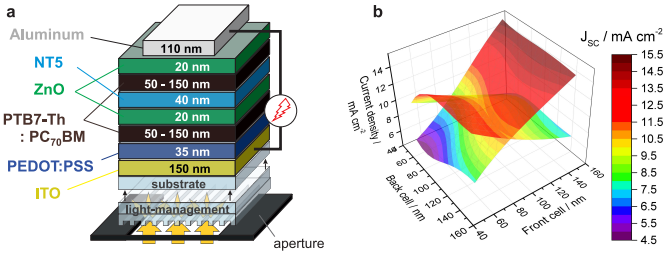

Figure 6.4: Optimization of layer thicknesses in the tandem stack. **a** Layer architecture and thicknesses of the printed tandem device with only aluminum being evaporated in vacuum. **b** Simulations of the two generated currents for both absorbers dependent on their thicknesses are used to find the best current matching conditions.

As discussed in Section 2.3 various surface structures have been demonstrated to successfully give rise to an absorption enhancement in single-junctions, which originates from the redirection of incident light into steep propagation angles [131, 132]. However, reports on external light management solutions for tandem devices are still rare [57], which may be based on the observation

of a rather angle independent performance in organic tandem cells [139]. In homo tandems this effect has been attributed to a balancing of the subcell currents, based on their complementary angle dependent spectral responses [130]. Hence, a wavelength independent light management strategy cannot enable an improved optical field distribution inside the devices. In the following it is shown how this limitation can be overcome by the wavelength dependent diffraction of periodic nanostructures.

6.2.1 Optical simulations of multi-junction cells

The current density of a serial tandem device is limited by the generated current in the weaker subcell, which means that a sophisticated optical design is required to match the photocurrents of the two absorbers [140]. Typically, this is achieved by a thinner top absorber to provide enough transmitted sunlight for the back cell. Since experimental testing of every combination of absorber thickness would be very time consuming, this is usually done through optical simulations [141]. Figure 6.4b shows such a simulation for the tandem stack shown in Fig. 6.4a. Each contour plots represents the current generated in one of the subcells, dependent on both absorber thicknesses. The intersection of the two planes yields the isoline for a matched current, whose maximum has to be found. In the present case, a front and back cell thickness of ≈ 80 nm and ≈ 130 nm, repectively, yields the highest current density value of 10.4 mA cm^{-2}. Note that, besides the chosen absorber material, this optimum combination of layer thicknesses is also determined by the materials and the thicknesses of the other layers in the tandem stack [49].

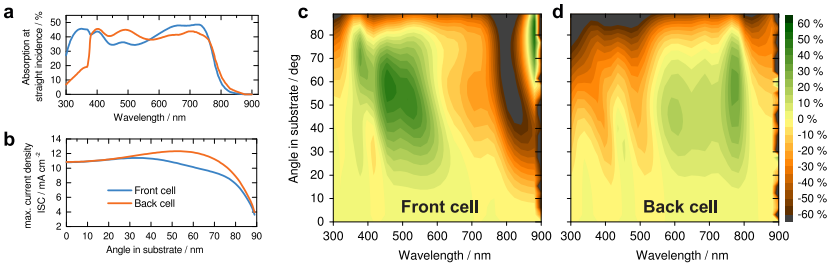

Figure 6.5: Angle dependent absorption in the subcells. **a** Simulated absorption of the two sub-cells in the tandem stack and **b** the respective angle dependent current generation. **c** Absorption in-/decrease for redirected light for the front cell and **d** for the back cell with respect to straight incidence

6.2.2 Light management in tandem devices

Figure 6.5a shows the simulated optical absorption in the two active layers of the tandem device with the layer thicknesses defined above. As in Chap. 4 the potential for light-redirection is examined by simulating the propagation of light at angles θ_S inside the substrate, which is shown in Fig. 6.5b. Since the layer thicknesses were optimized for straight incidence, the resulting currents match at $\theta_S = 0°$, however, the performance upon larger incident angles is predicted to be superior for the back cell. Because the same current must flow through both junctions, the final current of the device is limited by that of the weaker subcell. Consequently, although if light is redirected to angles $\theta_S > 30°$, the absorption enhancement in the back cell cannot contribute to a larger J_{SC} since the absorption in the front cell is even lower than for $\theta_S = 0°$.

However, the wavelength dependent simulations of the absorption reveals that the absorption of the front cell can be improved for larger propagation angles below 600 nm, but that this enhancement is compensated by a drastically reduced absorption at larger wavelengths (see Figs. 6.5c). Moreover, light redirection at wavelengths that are preferable for the front cell will simultaneously decrease the absorption in the back cell, which is only enhanced for oblique light of larger wavelength (see Fig. 6.5d).

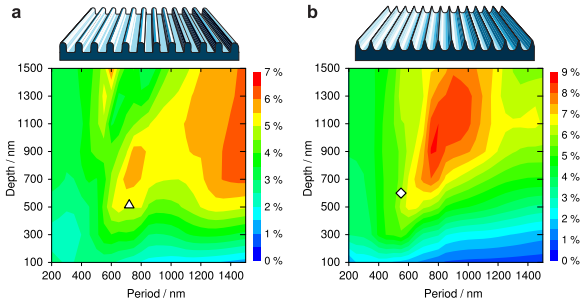

Figure 6.6: Enhancement in the generated short circuit current J_{SC} , simulated for two different light management geometries dependent on their period and depth. a Up to 7% increase can be obtained by a periodic nanostructure with a rounded rectangular profile and **b** up to 9% increase in the absorption can be expected when using a lorentzian lineshape.

To overcome this compromise, diffractive light management can be optimized for a wavelength dependent light redirection that takes into account both subcells to reach an overall gain in the short current density J_{SC} of the device. For this purpose, the least photocurrent of both absorber layers is taken as a

measure for different nanostructure configurations, which are compared to the J_{SC} of the pristine tandem. The calculated increase in the current density is shown in Fig. 6.6 for various periods and depths of two different nanostructure geometries. Simulations suggest an enhancement in the current density of 7% for a rounded rectangular nanostructure (Fig. 6.6a) and up to 9% for a lorentzian line nanostructure (Figure Fig. 6.6b). From the differences of the two graphs it can be seen once more how the shape of the nanostructure influences its diffraction properties and hence its light management performance.

6.2.3 Experimental

For each of the shown geometries, the respective light management sample from the previous section (see Fig. 6.3a and 6.3b) is indicated in Fig. 6.6 by the white triangle and the diamond, which will be tested in the following. According to the simulations, a current enhancement greater than 5% is expected for both configurations.

As in Sec. 6.1, the nanostructures were fabricated on a separate glass substrate which can then be attached to the device by a small amount of index matching gel. According to the device design described in Sec. 6.2.1, the tandem is fabricated by doctor blading all layers but the final aluminum electrode. After glass encapsulation of the best devices, the J-V characteristics are measured with and without the attached light management samples (see Fig. 6.7a). For both nanostructures an increase in the device efficiency is observed, provoked through the enhanced absorption and a larger J_{SC}.

Moreover, in contrast to previous experiments, the light management here is fixed on a glass substrate, which is attached to the encapsulated device only by an optical gel. Consequently, the nanostructures can readily be removed after a measurement to characterize the same device without light management, which enables a better assessment of its performance. Fig. 6.7b shows three such successive measurements on four devices, in which the lorentzian light management structure was fist attached to the tandem, secondly removed (with the glass carefully cleaned) and finally attached a second time. For all four devices the enhancement in efficiency with respect to the reference measurement is between 7-11% and is reproduced when the light management is attached a second time.

The measured increase in efficiency is larger than expected from the preceding simulations. This suggests that the currents in the fabricated tandem were not perfectly matched for straight incidence, which can be attributed to deviations in the experimental layer thicknesses with respect to the simulation of Sec. 6.2.1. The light management simulations predict a stronger enhancement

for the front cell than for the back cell by the lorentzian nanostructure, which would explain a higher total increase, if the front cell exhibited an initially lower current.

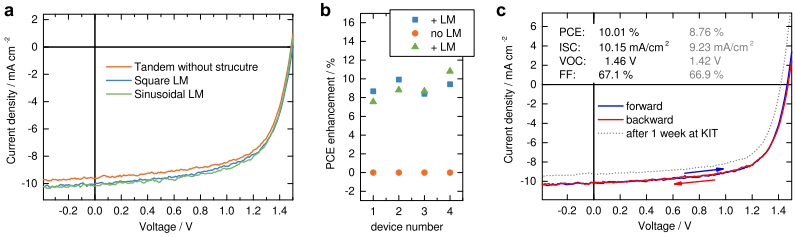

Figure 6.7: Experimental validation of light management for tandems. **a** The attachment of two different light management nanostructures to a finished tandem device yields an enhanced current generation and increases the efficiency. **b** Subsequent measurements with and without the attached nanostructure for four different tandem devices yield an enhanced efficiency of 7-11%. **c** The power conversion efficiency of the best device with light management was measured to be 10%. A following measurement with another solar simulator after one week revealed some degradation in the current and in the V_{OC}.

Finally, Fig. 6.7c shows the best obtained tandem device for which the efficiency was improved by 9% from 9.2% to 10.0% by the present light management solution. Although special care was taken to adjust the measurement and illumination conditions with the same precision as for previous single-junction measurements, a correct characterization of tandem devices requires a more elaborate procedure[142]. The spectral responses of both subcells deviate even in the homo tandem configuration (see Fig. 6.5a), which necessitates the calculation of separate mismatch factors based on the EQE of both subcells. Since this requires an advanced measurement setup for determining the spectral response of the individual cells [136], no mismatch calculation was performed to correct the measurement in Fig. 6.7c.

However, to control the measured enhancement, the device was additionally measured after 7 days by an independent research institute (dotted curve in Fig. 6.7c), where a PCE of 8.8% was obtained. The reduced V_{OC} and a lower short circuit current density are attributed to photo-degradation effects, which were observed for the tandem devices in successive measurements. However, the relative enhancement of the light management was preserved, which was confirmed by the same measurement procedure as in Fig. 6.7b.

7 Yearly energy harvesting

The good agreement of experimental and simulated enhancement that was obtained in the previous chapters of this work (see Figs. 4.11b, 5.7d and 5.8a) motivated the simulation of more complex light conditions, which cannot readily be tested by experiments.

In the first part different illumination conditions are compared, which are relevant for the characterization and the operation of photovoltaic devices. In consequence, the light management properties that are required for a successful energy harvesting are highlighted.

The second part considers a more detailed modeling of the yearly illumination conditions, combined with the angle dependent and spectral response of the photovoltaic device with and without different light management solution. Consequently, a better estimation of the yearly energy reward can be assessed, which is tested on different structural configurations of nanostructures introduced in the previous chapters

7.1 Illumination conditions

Standard test conditions

Solar cells are usually measured under standardized test conditions (STC) in order to provide comparable measurement of their performances (see Sec. 3.1.3). The used illumination is chosen to reflect the conditions, which are assumed to be representative for the average operation of the PV modules. The used reference spectrum takes into account a wide range of possible locations, the time-dependent light path through the air-mass (AM = 1.5) of the atmosphere and the related spectral changes (see Fig. A.4).

The solar year

Besides the above listed spectral specifications, standard test conditions are only defined for straight incident illumination, which for a stationary devices will only be attained in one single moment during a full year of operation. The power harvested during a year will hence not be accessible by a single measurement, but will be determined by the sum of many (hourly) contributions, each of which has its own individual illumination conditions.

These illumination conditions are mainly defined on the one hand by the location (latitude Λ), which together with the time-dependent declination $\delta(t)$ and the hour angle $\omega(t)$ defines the distribution of zenith angles $Z(t)$ [117]

$$\cos(Z) = \sin(\Lambda)\sin(\delta) + \cos(\Lambda)\cos(\delta)\cos(\omega) \tag{7.1}$$

and on the other hand by the device orientation (tilt angle[1] T), which defines the angle of incidence (AOI) distribution $\theta(t)$

$$\begin{aligned}\cos(\theta) = &\cos(Z)\cos(T) - \sin(\delta)\cos(\Lambda)\sin(T) \\ &+ \cos(\delta)\sin(\Lambda)\sin(T)\cos(\omega).\end{aligned} \tag{7.2}$$

Whereas the AOI is always defined with respect to the surface normal of the device, the zenith angle determines the air-mass that the light has to travel through the atmosphere. Consequently, the latter will define the illumination spectrum and consequently the solar power density that is available for harvesting:

$$\text{Latitude / tilt} \longrightarrow \text{AOI / air-mass} \rightarrow \text{spectrum} \rightarrow \text{power density}.$$

For a horizontal device orientation ($T = 0°$), for which in Eq. (7.2) $\theta = \text{Z}$, the time-dependent distribution of the zenith angle (seasonal movement), azimuth

[1] tilt direction is assumed southwards

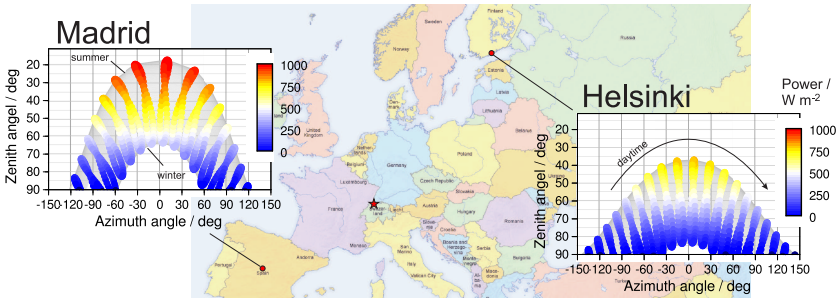

Figure 7.1: Latitude dependent solar radiation during the year. Already for locations accross Europe, the angular distribution of the incident sun light differs strongly for different daytimes and seasons. The power densitiy delivered by the sun is related to the zenith angle, which defines the path length through the earth's atmosphere (calculated with the Bird Simple Spectral Model [143], picture by San Jose[2].

angle (daylight movement) and the respective power density during a year is shown in Fig 7.1 for Helsinki and Madrid. It gets apparent how the location will influence the illumination conditions already across Europe: whereas in Madrid solar power density approaches 1000 W m^{-2} at noon in summer [3] exhibiting small zenith angles ($\approx 18°$), the maximum power density in Helsinki is only around 800 W m^{-2} at much larger zenith angles ($\approx 38°$). Moreover, compared with Madrid the time during a year where solar light is incident with angles larger than 65° is prevalent in Helsinki.

Taking into account these illumination conditions sets advanced requirements for a maximal harvesting to both photovoltaic devices and light management solution, since for example light harvesting at large incident angles will be much more important in Helsinki than in Madrid. However, due to the increased path length and the atmospheric absorption in the first location also different spectral regions have to be considered (see Apx).

[3] This number corresponds to the power density on a horizontal plane. For $T = 18°$, the power can reach >1040 W m^{-2} in Madrid and >1000 W m^{-2} in Helsinki for $T = 38°$.

[3] By San Jose (map), Hayden120 (retouch) [GFDL (http://www.gnu.org/copyleft/fdl.html) or CC-BY-SA-3.0 (http://creativecommons.org/licenses/by-sa/3.0/)], via Wikimedia Commons)

Light management

Naturally, these illumination conditions deviate strongly from standard test conditions, which significantly raises the importance of light management in the scope of a yearly energy harvesting. Since especially for printable photovoltaics the targeted low costs exclude any use of sun-tracking systems [117], cost-effective light management that can cover a broad angular range will be highly desirable.

Furthermore, a solution is required that can be easily adapted to the different irradiation conditions that are occurring in different locations or for various device orientations. Whereas the spectral response of a photovoltaic device itself cannot be modified for all of those applications, this is possible for an additive light management film. Provided that its fabrication costs are low, it could provide a location and application dependent expansion.

As discussed in Sec. 2.4.2, diffractive nanostructures thereby constitute a suitable candidate due to their freedom of design and their versatility: through variation of their structural parameters, the nanostructures can be tuned and tailored to meet the requirements for different illumination conditions, which is demonstrated in Sec.7.2.1 for printable photovoltaic application.

7.2 Modeling the yearly performance

The modeling of the yearly performance of a light management solution is composed on the one hand by the time-dependent illumination conditions, which were described in the preceding section, and on the other hand by the simulated angular response of the light management, which have to be calculated to the same detail.

This problem will be approached by a stepwise increase of the level of complexity of both parts, which are successively considered in the following four sections. Further, for each of the following stages, an application example is calculated for at least one nanostructure:

Sec.	Illumination condition	response of the device with light management	
7.2.1	hourly angle of incidence (AOI)	AOI	$\Delta\theta = 10°$
7.2.2	hourly spectrum and AOI	AOI 2 azimuth angles	$\Delta\theta = 1°$, $\Delta\phi = 90°$
7.2.3	hourly spectrum and AOI	AOI averaged azimuth angle	$\Delta\theta = 1°$, $\Delta\phi = 45°$
7.2.4	hourly spectrum, θ and ϕ	AOI and azimuth angle	$\Delta\theta = 1°$, $\Delta\phi = 1°$

Since more complex modeling will increase the computational effort, an op-

timization procedure by screening various nanostructure parameters within a reasonable amount of time, is only feasible in the first stage. However, the best obtained light management solutions will be tested and verified by the more sophisticated modeling stages of the following sections.

In order to further simplify the problem, for all following simulations Basel (Switzerland) is chosen as a representative location for central Europe (red star in Fig 7.1). This choice defines the yearly illumination conditions (Fig. 7.2), which can hence only deviate by the use of a different tilt angle T, as indicated in Fig. 7.2c for $T = \Lambda$. Note that, in all cases clear sky conditions are assumed.

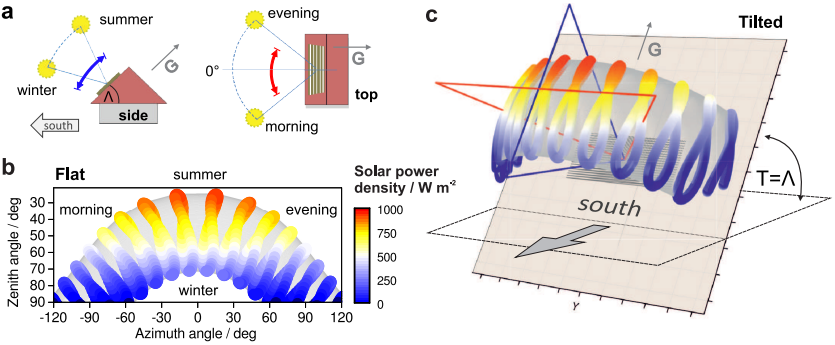

Figure 7.2: Yearly light harvesting with the light-managment. **a** Sketch of the seasonal and daylight angles of incidence of the sun and **b** the corresponding solar power density of the respective position of the sun throughout the year calculated for Basel, Switzerland. **c** 3D visualization of the solar angles that are incident on a device with tilt $T = \Lambda$. The times of high power can be covered in this case by a rather small angular response.

7.2.1 Hourly angle

In this first stage, only the angle of incidence of the sunlight will be considered as well as the question, which is the most important AOI for energy harvesting, measured by the delivered power versus the angle of incidence.

For that purpose, the Bird Simple Spectral Model [143] is used to screen all hours of one year and collect the respective AOI and the related power density. For each angular range ($\theta \pm 5°$), the total power that is incident under one of these angles during one year is calculated by summation. This results in an angle dependent weight $w_T(\theta)$, which indicates how much power will be incident under a certain angle.

Application cases

Since besides the location of the device, its orientation with respect to the surface will define further requirements on the photovoltaic performance, the aforementioned weight function $w_T(\theta)$ is calculated for various tilt angles T. Four scenarios were therefore selected as relevant application cases for printable photovoltaics (see Fig. 7.3).

a Shadings ($T = Z$) - Due to low-cost and lightweight of OPVs, they may be used as energy harvesting sun protection or mobile chargers, which are always pointed directly towards the sun.

b Façade/ windows ($T = 90°$) - Light weight and semi-transparency motivate an application on large building-façades in a vertical orientation (facing south).

c Ceiling / portables ($T = 0°$) - Conformal integration of printed PV into products is possible due to its flexibility and free-form producibility. Rooftops of cars and portable devices, thereby are preferably charged in a horizontal orientation.

d Best tilt ($T = \Lambda$) - For building integrated colorful OPV devices of off-grid applications, also the tilted orientation can be of importance. Here the tilt angle for maximum yearly sun collection is chosen as an example.

The resulting angular weights are depicted in Fig. 7.3a-d and show strong differences with maxima at 0°, 60°, 40° and 20°, respectively. Note that, only for case **a**, incident light at $\theta = 0°$ will be of importance for energy harvesting.

In order to evaluate the performance of any light management with respect to the four application cases, a generated current $J_{i,\theta}$ is calculated for each nanostructure configuration and for all 9 angles ($\Delta\theta = 10°$) from Fig. 7.3. A figure of merit g_i^T is then obtained by multiplying $J_{i,\theta}$ with the respective angle dependent weight of each application case, which yields

$$g^T_{i=1,\ldots,432} = \sum_{\theta=0°}^{\theta=80°} J_{i,\theta} \cdot w_T(\theta). \tag{7.3}$$

With this calculation, an estimation for the optimal parameters of the light management can be evaluated for each case within a reasonable calculation time.

Figure 7.3: Various application planes and their irradiation. **a** Shadings, which are always pointed towards the sun (picture taken from Ref. [54]) **b** South-oriented facade or window blind (demonstrator of the SUNFLOWER project at LOPE-C conference, 2016) **c** Horizontal ceiling of buildings or cars (picture by Morio[4]) **d** South-oriented building-elements, installed with a tilted angle. (Famous foyer glas ceiling by Otto Piene at the University of Konstanz)

Example: Rectangular line nanostructures

For demonstration purposes, the simple rectangular line structure (Fig. 2.4a) is chosen to be optimized for each of the aforementioned application cases. The investigated parameter space includes periods ranging from 250 to 1000 nm in steps of 50 nm, duty cycles of 20, 50 and 80 and a depth ranging from 200 to 1000 in steps of 100 nm, thus yielding 432 possible configurations.

The results of this optimization routine are listed in Tab. 7.1. Since case **a** corresponds to requirements that were investigated in previous chapters, the obtained parameters are matching the maximum predicted in Fig. 4.8, whereas the optimum period for all other cases are either higher or lower.

The calculated current densities for the nine angles are shown in Fig. 7.4 for the four optimized configurations of Tab. 7.1, with the angular response of the unstructured device added as dashed line. In all cases an enhancement with respect to the reference is observed for angles that correspond to the angular distributions of Fig. 7.3.

These results demonstrate, how an additive light management solution can be

[4]By Morio (Own work) [CC BY-SA 3.0 (http://creativecommons.org/licenses/by-sa/3.0)], via Wikimedia Commons

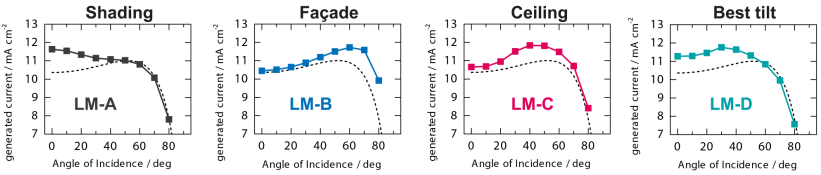

Figure 7.4: Performance of optimizted rectangular line nanostructures. The angular response is following the irradiation conditions of the respective application case, defined in Fig. 7.3.

Table 7.1: Nanostructure parameters from optimization to different application cases

Case	period [nm]	depth [nm]	duty cycle
a LM-A (Shading)	600	400	50
b LM-B (Façade)	250	200	20
c LM-C (Ceiling)	1000	200	50
d LM-D (Best tilt)	1000	400	50

used to customize a PV device for various orientations, locations or applications. Furthermore, with this approach, universal high throughput printable photovoltaics could be equipped with the most suitable light-management film for different application cases.

7.2.2 Hourly spectra

In the second stage of yearly simulations, the time-dependent spectrum will be additionally considered to evaluate the yearly performance of the obtained optimized nanostructures in more detail. Whereas in the previous stage, the standard solar spectrum (AM1.5G) was used in Eq. (2.5) to calculate $J_{i,\theta}$, a separate calculation for every hour is applied here in order to obtain a yearly power output.

For this purpose the same model as in Sec 7.2.1 is used to collect the respective angle of incidence $AOI(h)$ and the spectrum $S(h,\lambda)$ for every hour h of the year and for each of the above application cases (Fig. 7.3a-d). Using Eq. (2.5), a current density $J_{SC}(h)$ is calculated for every hour (24×365) with

$$\eta_{EQE} = \eta_{IQE} \cdot Abs(AOI(h),\lambda)_{\phi} \quad \text{and} \quad S(\lambda) = S(h,\lambda) \tag{7.4}$$

and with η_{IQE} set to unity. The angle dependent absorption in the device $Abs(\theta,\lambda)_{\phi}$ is calculated with an increased angle resolution of $\Delta\theta = 1^{\circ}$ and has

to be determined for the reference device and for each device with a different light management. Using $J_{SC}(h)$, the generated energy per square meter and year E_{yr} is then determined by a summation of the generated power of each hour of the year

$$E_{yr} = \sum_{h=1}^{24\times365} FF(h) \cdot V_{OC}(h) \cdot J_{SC}(h), \tag{7.5}$$

where $FF = 70\%$ and $V_{OC} = 0.7\ V$ are approximated to be constant throughout all angles of incidence and irradiation powers. It has been shown experimentally that within illumination intensities between 1000 W m^{-2} and 100 W m^{-2} [39] this approximation is reasonable for organic photovoltaics and the angle dependent measurements from Sec.5.1 suggest the same (see Fig. 5.3 with only a minor decrease in V_{OC}.

Example: Rectangular line nanostructures

For each application case, the first row of Tab. 7.2 shows the calculated total amount of incident solar energy during one year and the fraction that would be harvested by the reference device. In the following the predicted energies harvested with the application of the four nanostructure configurations from Tab. 7.1 are listed, where bold numbers indicate the highest values in each application case.

In the previous stage, the plane of incidence for the angle dependent simulation of the light management was $\phi = 0°$, which assumed that its orientation always followed that of the sun. However, as can be seen from Fig. 7.1 the light is incident from various azimuth directions during a year. For this reason, both cases of $\phi = 0°$ or $\phi = 90°$ are calculated, which will give the opportunity to estimate an average enhancement from both contributions (see Tab. 7.2).

As previously observed for the angle dependent behavior of rectangular nanostructures (Fig. 5.1), in some cases the harvested energy differs drastically for the two azimuth orientations. For case **c** this even leads to an average enhancement which is higher for LM-D than for the initially optimized structure LM-C. The same is observed for case **b**, where the enhancement of LM-D exceeds that of LM-B due to its strong harvesting performance at $\phi = 90°$.

Moreover, for this case even the value for of LM-C at $\phi = 0°$ is slightly higher than for LM-B, although the latter was evaluated better suited in the preceding optimization. This can only explained with the differences in their angle dependent spectral response, which for LM-C apparently matches better to

Table 7.2: Estimated energy generation with and without different light managements in two orientations and for the different application cases. The bold values state the best light management performance at $\phi = 0°$ and the best average enhancment for each orientation.

(in kWh m^{-2} a^{-1})	**a** Shading	**b** Façade	**c** Ceiling	**d** Best tilt
Total energy	3182.0	1590.3	1789.9	2239.6
Reference	146.8	76.2	92.8	111.3
LM-A, $\phi = 0°$	**166.6**	77.14	94.1	116.5
LM-A, $\phi = 90°$	166.6	87.3	106.5	127.8
Enhancement [%][1]	**13.5**	7.9	8.1	9.8
LM-B, $\phi = 0°$	148.1	81.7	99.0	115.3
LM-B, $\phi = 90°$	148.1	80.3	97.2	114.1
Enhancement [%][1]	0.9	6.3	5.7	3.1
LM-C, $\phi = 0°$	151.4	**81.8**	**100.0**	118.8
LM-C, $\phi = 90°$	151.4	86.2	104.3	119.3
Enhancement [%][1]	3.1	10.2	10.1	7.0
LM-D, $\phi = 0°$	161.5	79.1	96.8	**119.7**
LM-D, $\phi = 90°$	161.5	89.7	108.7	126.2
Enhancement [%][1]	9.9	**10.7**	**10.8**	**10.5**

[1] obtained with the average for both azimuth directions.

case **b** than for LM-B, when the more detailed spectra $S(h)$ are considered instead of the standard spectrum (AM1.5G) as in Fig. 7.4.

Accounting for the strong performance deviations at different ϕ, the azimuth direction has to be considered in more detail in order to predict the yearly performance of a line nanostructure, which will be addressed in Sec. 7.2.4. However, as discussed in Sec. 5.1, the azimuth angle dependence can be strongly reduced with the use of a crossed nanostructure, which is demonstrated in the next stage.

7.2.3 Averaged azimuth response

In this third stage, additionally to the use of hourly illumination conditions, the azimuth response of the nanostructure will be considered by averaging the

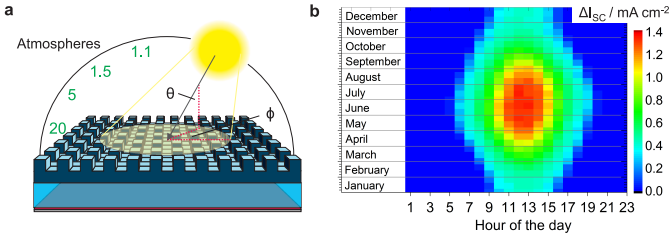

Figure 7.5: Simulated yearly current enhancement of the crossed nanostructure. **a** Shematic visualisation of the variable test conditions for the OPV throughout a year. **b** Increase in generated current of a device equipped with the crossed nanostructure for every hour in the year.

response of the light management. For that purpose, the bidirectional scattering distribution functions (BSDF) of the nanostructure (see Sec. 3.2.4) is calculated for three different azimuth angles $\phi = 0°, 45°, 90°$ and the results are then averaged in order to yield a BSDF, which can be considered as rotation symmetric response of the light management for various AOIs.

As in the previous stage, $AOI(h)$ and $S(h)$ are used to calculate the hourly current densities of the light management device $J_{SC}^{LM}(h)$ and the reference $J_{SC}^{Ref}(h)$ with the use of the commercial software. By introducing the enhancement factor f of the light management with respect to the reference

$$f = \frac{E^{LM} - E^{Ref}}{E^{Ref}} = \frac{\sum_h \left(J_{SC}^{LM}(h) - J_{SC}^{Ref}(h) \right)}{\sum_h J_{SC}^{Ref}(h)}, \tag{7.6}$$

constant FF and V_{OC} of Eq. (7.5) can be eliminated. The enhancement of the harvested energy can thus be directly approximated based on the generated current density.

Example: Crossed nanostructures

As discussed in Sec. 5.1, the dependence on ϕ can be even more suppressed if a crossed nanostructure is chosen as light management and the error made by the averaging of the BSDF can hence be reduced with respect to line structures. Since, the experimentally observed angular performance of the crossed nanostructure shown in Fig. 5.3 is well suited for the yearly solar harvesting, it is used in the following for a calculation of f.

As sketched in Fig. 7.5a, case **c** with the orientation of the device parallel to the ground is chosen to evaluate the performance of the light management. The

numerator of Eq. (7.6), which yields the additional current generation obtained through absorption enhancement of the nanostructure, is shown in Fig. 7.5b for every hour of the year. In total an enhancement factor of $f = 1.121$ is obtained, which suggest that the harvested energy with the use of this crossed nanostructure is increased by $f = 12.1\%$ with respect to the reference device.

7.2.4 Extrapolated azimuth response

In the fourth stage, it is attempted to assess the full azimuth information of both the incident illumination and the response of the device. Whereas $\phi(h)$ can be extracted from the NREL model as the other illumination parameters (see Fig. 5.8b), the second is more challenging since a calculation of $Abs(\theta, \lambda)$ for 90 possible azimuth angles would require several days on a average desktop PC for one single symmetric nanostructure configuration.

To reduce the computational effort, simulations of the angle dependent absorption $Abs(\theta, \lambda)_\phi$ are done only for $\phi = 0°$ and $90°$, however, absorption of intermediate azimuth angles $0° < \phi < 90°$ are approximated to be linearly related to these extreme values. For that purpose a factor is defined as

$$k(\phi) = \begin{cases} |\phi/90°| & \text{for } |\phi| \leq 90° \\ |(\phi - 180°)/90°| & \text{for } |\phi| > 90°, \end{cases} \tag{7.7}$$

with $0 < k(\phi) < 1$, which defines the ratio of intermixing the two azimuth contributions. For a crossed or asymmetric nanostructure, Eq. (7.7) has to be adapted, since it has to be distinguished only between $\phi = 0°$ and $45°$ for the first and between positive and negative ϕ for the latter. The current density can then be calculated by

$$\begin{aligned} J_{SC} = \frac{e}{hc} \int_\lambda \eta_{IQE} \cdot [k(\phi) \cdot Abs_{\phi=90°}(\lambda, \theta) \\ + (1 - k(\phi)) \cdot Abs_{\phi=0°}(\lambda, \theta)] \cdot S_{\phi,\theta}(\lambda)\ \lambda\ d\lambda. \end{aligned} \tag{7.8}$$

As previously defined, e is the elementary charge, h is Plank's constant and c is the vacuum speed of light.

With this approximation the full distribution of azimuth angles can be taken into account by using the respective interpolated azimuth angle to calculate its respective angular response (given in Eq. (7.8) in brackets) and to determine J_{SC}. This is demonstrated in following for two examples of embedded nanostructures.

Example: Embedded crossed nanostructures

With the yearly enhancement of the crossed nanostructure from Sec. 7.2.2, which was fabricated on large-area foils in Sec. 5.2, a light management film with a yearly reward could be established. In order to meet the last missing property of the light management requirements listed in Sec. 1.3, a cost-effective yearly performance should be demonstrated for an embedded crossed nanostructure, as depicted in Fig. 7.6a.

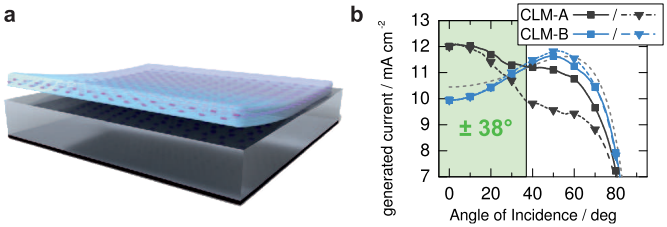

Figure 7.6: Embedded crossed nanostructure film for a yearly harvesting. **a** A self contained film with an buried crossed nanostructure can be laminated onto a finished OPV. **b** For application case **a** (CLM-A) and case **b** (CLM-B) two strucutures are optimized, whose angular responses under AM1.5G illumination are shown for $\phi = 0°$ (squares) and $\phi = 45°$ (triangles). Compared to the reference (grey dashed line) CLM-A exhibits a broad enhancment range of $\pm 38°$ for $\phi = 0°$.

Since a parameter optimization in this stage of yearly calculation would be too elaborate, the routine from Sec. 7.2.1 is used to find a suitable nanostructure configuration for case **a** and **b** ($\phi = 0°$). The angular dependent J_{SC} obtained with the standard spectrum (AM1.5G) for the two best embedded crossed light management configurations CLM-A and CLM-B are shown in Fig. 7.6b. As expected from the requirements of case **a**, CLM-A exhibits a large enhancement at $\theta = 0°$ with respect to the reference. For $\phi = 0°$ this enhancement is maintained over an angular range of $\pm 38°$ (green area), however, the angle dependent performance of CLM-A along $\phi = 45°$ is decreasing fast for larger angles. In contrary, the angular response of CLM-B shows a inferior performance compared to the reference at $\theta = 0°$, but shows an enhancement for larger angles $35° < \theta < 55°$.

In a next step, the detailed calculation of the angle dependent absorption $Abs(\theta, \lambda)_\phi$ is performed for $\phi = 0°$ and $\phi = 45°$, which are then used in Eq. 7.8 with the time-dependent spectra to determine the yearly energy harvesting (again using $FF = 70\%$ and $V_{OC} = 0.7\ V$). The resulting performance of the two light management configurations CLM-A and CLM-B are shown in Tab. 7.3, calculated for the application cases from Fig. 7.3.

Table 7.3: Estimated energy generation with and without different embedded crossed nanostructures and the enhancment expected for each orientation.

(in kWh m^{-2} a^{-1})	**a** Shading	**b** Façade	**c** Ceiling	**d** Best tilt
CLM-A	170.7	72.3	88.5	113.8
Enhancement [%]	16.3	-5.1	-4.6	2.3
CLM-B	141.3	79.3	96.6	113.8
Enhancement [%]	-3.8	4.1	4.2	2.2

As expected the strongest enhancement is obtained for CLM-A in the case of straight incidence over the year. Furthermore, this light management can provide an enhancement for a fixed installation with the best tilt (case **d)**, originating from the broad angular span of the enhancement along both directions (see Fig. 7.6b). Since independent on the location on earth, at noon the zenith angle span between summer and winter equals twice the equator's tilt with respect to the ecliptic ($Z = \Lambda \pm 23.4°$) [5], the enhancement range of $\theta = \pm 28°$ is already sufficient to improve the performance for all seasons if oriented properly (see Fig. 7.2). Since at these times the solar radiation is most intense this is predicted to be sufficient to increase the total generated yearly energy about 2.3% (see Tab. 7.3), despite the weak performance of CLM-A at large angles.

In consequence, the performance for cases **b** and **c**, however, is rather weak for CLM-A. Light harvesting for these cases can be better addressed with the second configuration (CLM-B) which was optimized for a vertical orientation and which predicts enhancements above 4% for these cases. It is noteworthy, that with a -4.8% reduced current at $\theta = 0°$ under AM1.5G light (see Fig. 7.6b), this configuration would not have attracted much attention. However, if the angle distribution and the changed irradiation spectra over the whole year are taken into account, it can be much better suited for certain application cases (**b** and **c**) than the structure with the superior performance under STC.

Example: Embedded asymmetric nanostructure

The performance improvement of $> 4\%$ caused by the embedded crossed nanostructure CLM-B for case **b** and **c** demonstrates, how an increase in the

[5] this can be seen from Eq. (7.1), which reduces to $\cos(Z) = \cos(\Lambda - \delta)$ for $\omega = 0$, where $-23.4° < \delta < 23.4°$.

energy harvesting can be obtained, when the device is orientated properly with respect to its angular response. If these conditions are explored further, it gets apparent that the sun's seasonal movement (Fig. 7.2a) exhibits a certain asymmetry in terms of delivered power: for locations outside the tropical zone[6], the proximity of the sun and hence the delivered power has its maximum in summer and decreases steadily towards winter as shown in Figs. 7.1 and 7.2b. In contrast, the daylight movement has its power maximum around noon and is symmetric with respect to morning or evening.

In consequence, a light management structure as introduced in Sec. 5.3, which exhibits an asymmetric coating will be perfectly suited to maximize the energy harvested during a solar year. The enhancement measured in Fig. 5.8b thereby exhibits improvements for a small range of angles $\theta_{\phi=0^\circ} \leq 25^\circ$ with some asymmetry, but improvements over a wide range of angles $\theta_{\phi=90^\circ}$ in the perpendicular direction with symmetric behavior.

The absorption in the active layer $Abs(\lambda, \theta)_{\phi=0^\circ,90^\circ}$ is simulated for the light management structure of Sec. 5.3 on two reference devices with different active layer thickness, i.e. $d = 90$ nm and $d = 130$ nm. The first is the thickness of the reference device defined in Sec. 4.1 which was also used in the calculation of the previous examples, whereas the second thickness was obtained in the experiments of Sec. 5.3 on which the asymmetric nanostructure was measured. Furthermore, for the asymmetric direction, positive and negative angles have to be distinguished, which is addressed by the extension of $Abs(\theta, \lambda)$ to negative angles $\theta = [-89^\circ, 89^\circ]$. With the device and the nanostructure lines facing south with a tilt equal to the local latitude [7] $T = \Lambda$ (case **d**), the performance of the light management is evaluated.

Table 7.4: Estimated energy generation with and without the asymmetric embedded line nanostructures calculated for two different active layer thicknesses in the best tilt configuration (case **d**, see Fig. 7.2c).

(in kWh m^{-2} a^{-1})	Total energy	Reference	emb. LM	Enhancement [%]
90 nm active layer	2239.6	111.3	117.7	↑ 5.8
130 nm active layer	2239.6	108.1	121.6	↑ 12.5

Assuming $\eta_{IQE} = 1$ and again an average fill factor of 70% and a constant V_{OC} of 0.7 V, the energy harvested by the photovoltaic device without light management in this conditions can be approximated and is listed in Tab. 7.4.

[6] regions with latitude $|\Lambda| > 23.4^\circ$
[7] $\Lambda \approx 47.6^\circ$ for Basel, Switzerland

With a generated energy of 117.7 kWh m^{-2} a^{-1} for $d = 90$ nm, the embedded asymmetric nanostructure performs better than the embedded crossed nanostructure from the previous example (see Tab. 7.3) and increases the harvesting about 5.8 %.

For the device with the thicker active layer ($d = 130$), the energy harvested with the reference device is lower than for the case of $d = 90$ nm. Since already in the simulations of Fig. 4.2b a lower current was obtained with respect to $d = 90$ nm, it was expected that this holds also for the yearly current generation. However, when the same embedded structure is applied on the thicker device, the harvested energy is increased by 12.5% [144], yielding a value that is even higher than for the thinner device with the nanostructure.

This finding suggests, that it could be possible to obtain not only a larger improvement but also a greater absolute yearly energy harvesting on devices, that were not optimized for straight incidence. However, further investigations are necessary to fully understand this dependence on the device optics under yearly light conditions.

PART III

BACKMATTER

Conclusions & Outlook

Summary

In the present thesis, a new concept of light management was introduced, which distinguished from existing solutions on the one hand, by its external application to the device, which makes it fully independent from the photovoltaic device fabrication and, on the other hand, by its great flexibility which enables versatile applications.

The influence of the diffractive nanostructures on the device optics was investigated and in the following an efficiency enhancement could be demonstrated with respect to a reference device. Thereafter, different configurations could be designed and experimentally validated:

- a crossed nanostructure for a better angular response
- a lamination process for large-scale application
- an embedded structure for protection from external influences and abrasion
- the application on different state-of-the-art devices and tandems

The resulting improvements that were obtained on different devices are summarized in the following table.

Besides the experimental work on the topic, an optical model was developed and adapted during this thesis, which enabled an optimization procedure for

	Enh. [%]	PCE_{ref} [%]	PCE_{LM} [%]	FoM
Chap. 5 (laminated film)	24.2	4.3	5.3	28.8
Chap. 5 (embedded)	10.7	5.7	6.3	31.9
Chap. 6 (thick absorber)	3.4	9.6	9.9	31.2
Chap. 6 (tandem)	8.5	9.2	10.0	80.0

the structural configuration of the diffractive nanostructures and was able to reproduce the experimentally observed enhancement. Furthermore, it was capable to estimate the impact of the light management, when the more complex light conditions of a whole year are considered. This estimation of the yearly performance predicted an increase in harvested energy of 12-13% for the crossed nanostructures that was fabricated on 500 cm^2 plastic sheets and for the asymmetric nanaostructure that was embedded in a protective polymer matrix, respectively.

Finally, all requirements that were imposed on the light management in Sec. 1.3 could be addressed by this work. Together with the demonstrated technological opportunities and the optical model, it provides a platform for customized development of light management solutions based on diffractive nanostructures.

Conclusion

General OPV light management

Light management in thin film solar cells still holds a great potential for improvement, due to their angle, wavelength and polarization dependent coherence effects. Hence, this potential can only be fully exploited by wavelength (polarization) selective light management.

Moreover, to date only few reports on light management consider the related problems of their solution, i.e. compatibility with printing processes and manufacturing costs. However, these issues are of great importance for the actual adaption of the light management technology.

Modeling of yearly harvesting

It was revealed by the simulations in this thesis, that for solar light management it is of utmost importance to consider the yearly light conditions additionally to the standard photovoltaic test conditions. Structures that only

exhibit an efficiency enhancement for larger angles, will seem useless in a single measurement at STC. However, they can still yield a considerable increase in the yearly energy harvesting, which is the criterion that makes a solution attractive for application. Especially for printed photovoltaics, which target non-classical solar cell integration far from the conventional device orientations, this constitutes an essential requirement for future light management solutions.

Since the experimental access to yearly measurements is limited, a reliable optical model had to be established, that is able to reproduce the experimental results in detail for the standard measurements and hence enables the assessment of the yearly potential of any light management configuration.

Outlook

Optical design

In this thesis, dielectric embedded high index nanostructures were confirmed as a device independent but protected light management solution. Since such configuration offers a variety of further realizations, it is expected that considerable advances in the (yearly) efficiency enhancement are within reach.

More sophisticated realizations of photon control structures have for example been proposed by Martins et al. [145], who suggest to use quasi-random structures that can be optimized for photovoltaic applications. In general, there are only few limitations on the shape of such periodic nanostructures, one of which remains the compatibility with mass-manufacturing.

Up-scaling effects

Another aspect that was only briefly discussed, is the dependence of the light management enhancement on the device area. It was shown by Esiner et al. [69] that for increasing device area, the obtained enhancement of a light redirection surface structure was drastically increased upon illumination through the same shadow mask. Consequently, for smaller device size, more light was redirected away from the charge collecting area.

This effect could be reduced if either the device coverage on the substrate is increased, or if the thickness of the substrate is decreased, which will bring the light management closer to the absorber. Hence, the enhancement effect

of the light management is expected to be maximized on modules with a large geometrical fill factor, which are fabricated on thin foils or flexible glass.

Semi-transparent & tandems devices

In this thesis, light management was presented and analyzed on opaque devices, where the enhancement is based on interference in the multilayer stack. Consequently, these optical effects will be much weaker in semi-transparent devices that lack a reflective back electrode. However, smaller absorption enhancement originating from an increased optical path could still be addressed. Moreover, rear reflection of light with desired optical properties can introduce or eliminate a desired color [66, 146] or simply enhance the absorption by backscattering. Naturally, this comes to the cost of transparency (for certain angles [147]), but in turn avoids the parasitic absorption of a metal back electrode [148].

Another approach by Tang et al. [149] was further used for photocurrent balancing in tandems devices, which is a second interesting application that should be further exploited. The results of Chap. 6 suggest, that in particular the angle dependent performance of tandems can be improved by sophisticated light management: due to their complementary absorption spectra, it is possible to individually address the subcells in different spectral regimes [44] with the use of a single light management solution.

Bibliography

[1] Y. Liu, J. Zhao, Z. Li, C. Mu, W. Ma, H. Hu, K. Jiang, H. Lin, H. Ade, and H. Yan, Nature Communications **5**, 5293 (2014).

[2] S. Zhang, L. Ye, W. Zhao, D. Liu, H. Yao, and J. Hou, Macromolecules **47**, 4653 (2014).

[3] W. Zhao, D. Qian, S. Zhang, S. Li, O. Inganäs, F. Gao, and J. Hou, Adv. Mater. (2016), 10.1002/adma.201600281.

[4] M. Graetzel, R. A. J. Janssen, D. B. Mitzi, and E. H. Sargent, Nature **488**, 304 (2012).

[5] J. Zhao, Y. Li, G. Yang, K. Jiang, H. Lin, H. Ade, W. Ma, and H. Yan, Nature Energy **1**, 15027 (2016).

[6] S. H. Park, A. Roy, S. Beaupré, S. Cho, N. Coates, J. S. Moon, D. Moses, M. Leclerc, K. Lee, and A. J. Heeger, Nature Photonics **3**, 297 (2009).

[7] K. Vandewal, S. Albrecht, E. T. Hoke, K. R. Graham, J. Widmer, J. D. Douglas, M. Schubert, W. R. Mateker, J. T. Bloking, G. F. Burkhard, A. Sellinger, J. M. J. Fréchet, A. Amassian, M. K. Riede, M. D. McGehee, D. Neher, and A. Salleo, Nature Materials **13**, 63 (2013).

[8] X. Guo, N. Zhou, S. J. Lou, J. Smith, D. B. Tice, J. W. Hennek, R. P. Ortiz, J. T. L. Navarrete, S. Li, J. Strzalka, L. X. Chen, R. P. H. Chang, A. Facchetti, and T. J. Marks, Nature Photonics **7**, 825 (2013).

[9] J. A. Bartelt, Z. M. Beiley, E. T. Hoke, W. R. Mateker, J. D. Douglas, B. A. Collins, J. R. Tumbleston, K. R. Graham, A. Amassian, H. Ade, J. M. J. Fréchet, M. F. Toney, and M. D. McGehee, Advanced Energy Materials **3**, 364 (2012).

[10] Z. He, C. Zhong, S. Su, M. Xu, H. Wu, and Y. Cao, Nature Photonics **6**, 593 (2012).

[11] V. K. Narasimhan and Y. Cui, Nanophotonics **2** (2013), 10.1515/nanoph-2013-0001.

[12] F.-J. Haug and C. Ballif, Energy Environ. Sci. **8**, 824 (2015).

[13] F. Priolo, T. Gregorkiewicz, M. Galli, and T. F. Krauss, Nature Nanotech **9**, 19 (2014).

[14] M. L. Brongersma, Y. Cui, and S. Fan, Nature Materials **13**, 451 (2014).

[15] W. Cao and J. Xue, Energy Environ. Sci. **7**, 2123 (2014).

[16] G. Kang, J. Yoo, J. Ahn, and K. Kim, Nano Today **10**, 22 (2015).

[17] J. A. Liddle and G. M. Gallatin, ACS Nano **10**, 2995 (2016).

[18] M. Hosel, H. F. Dam, and F. C. Krebs, Energy Technology **3**, 293 (2015).

[19] W. Clemens, D. Lupo, K. Hecker, and S. Breitung, *OE-A Roadmap for Organic and Printed Electronics*, 6th ed. (OE-A (Organic and Printed Electronics Association), 2015).

[20] International Energy Agency (IEA), *Key World Energy Statistics 2016*, online (2016), accessed on 4th Nov 2016: http://www.iea.org/publications/freepublications/publication/KeyWorld2016.pdf.

[21] J. Tsao, N. Lewis, and G. Crabtree, *Solar FAQs*, online (2006), accessed on 4th Nov 2016: http://www.sandia.gov/~jytsao/Solar{%}20FAQs.pdf.

[22] United Nations, *7. d Paris Agreement*, online (2015), accessed on 4th Nov 2016: https://treaties.un.org/pages/ViewDetails.aspx?src=TREATY&mtdsg_no=XXVII-7-d&chapter=27&clang=_en.

[23] European Commission, *Share of renewables in energy consumption in the EU rose further to 16% in 2014*, online (2016), accessed on 4th Nov 2016: http://ec.europa.eu/eurostat/documents/2995521/7155577/8-10022016-AP-EN.pdf/38bf822f-8adf-4e54-b9c6-87b342ead339.

[24] European Commission, *Energy Roadmap 2050*, online (2011), accessed on 4th Nov 2016: http://eur-lex.europa.eu/legal-content/EN/TXT/PDF/?uri=CELEX:52011DC0885&from=EN.

[25] A. Neslen, *Portugal runs for four days straight on renewable energy alone*, online (2016), accessed on 4th Nov 2016: https://www.theguardian.com/environment/2016/may/18/portugal-runs-for-four-days-straight-on-renewable-energy-alone.

[26] M. A. Green, K. Emery, Y. Hishikawa, W. Warta, and E. D. Dunlop, Progress in Photovoltaics: Research and Applications **24**, 905 (2016).

[27] H. Zhang, J. M. Kurley, J. C. Russell, J. Jang, and D. V. Talapin, J. Am. Chem. Soc. **138**, 7464 (2016).

[28] H. P. Mahabaduge, W. L. Rance, J. M. Burst, M. O. Reese, D. M. Meysing, C. A. Wolden, J. Li, J. D. Beach, T. A. Gessert, W. K. Metzger, S. Garner, and T. M. Barnes, Appl. Phys. Lett. **106**, 133501 (2015).

[29] Y. E. Romanyuk, H. Hagendorfer, P. StÃ¼cheli, P. Fuchs, A. R. Uhl, C. M. Sutter-Fella, M. Werner, S. Haass, J. StÃ¼ckelberger, C. Broussillou, P.-P. Grand, V. Bermudez, and A. N. Tiwari, Advanced Functional Materials **25**, 12 (2015).

[30] A. Chirilă, P. Reinhard, F. Pianezzi, P. Bloesch, A. R. Uhl, C. Fella, L. Kranz, D. Keller, C. Gretener, H. Hagendorfer, D. Jaeger, R. Erni, S. Nishiwaki, S. Buecheler, and A. N. Tiwari, Nature Materials **12**, 1107 (2013).

[31] W. Wang, M. T. Winkler, O. Gunawan, T. Gokmen, T. K. Todorov, Y. Zhu, and D. B. Mitzi, Advanced Energy Materials **4**, 1301465 (2014), 1301465.

[32] Raynergy Tek Inc., *Raynergy tek sets world record solution processed single junction opv pce 11.51% using halogen-free ink formulation*, press release (2016), accessed on 4th Nov 2016: `http://www.raynergytek.com/news.asp`.

[33] J. Czolk, D. Landerer, M. Koppitz, D. Nass, and A. Colsmann, Advanced Materials Technologies , 1600184 (2016).

[34] G. Adam, M. Kaltenbrunner, E. D. Glowacki, D. H. Apaydin, M. S. White, H. Heilbrunner, S. Tombe, P. Stadler, B. Ernecker, C. W. Klampfl, N. S. Sariciftci, and M. C. Scharber, Solar Energy Materials and Solar Cells **157**, 318 (2016).

[35] X. Yin, P. Chen, M. Que, Y. Xing, W. Que, C. Niu, and J. Shao, ACS Nano **10**, 3630 (2016).

[36] T. M. Schmidt, T. T. Larsen-Olsen, J. E. Carle, D. Angmo, and F. C. Krebs, Advanced Energy Materials **5**, 1500569 (2015), 1500569.

[37] M. Bernechea, N. C. Miller, G. Xercavins, D. So, A. Stavrinadis, and G. Konstantatos, Nature Photonics **10**, 521 (2016).

[38] S.-H. Bae, H. Zhao, Y.-T. Hsieh, L. Zuo, N. D. Marco, Y. S. Rim, G. Li, and Y. Yang, Chem **1**, 197 (2016).

[39] Z. He, B. Xiao, F. Liu, H. Wu, Y. Yang, S. Xiao, C. Wang, T. P. Russell, and Y. Cao, Nature Photonics **9**, 174 (2015).

[40] M. Scharber and N. Sariciftci, Progress in Polymer Science **38**, 1929 (2013).

[41] N. Li, D. Baran, G. D. Spyropoulos, H. Zhang, S. Berny, M. Turbiez, T. Ameri, F. C. Krebs, and C. J. Brabec, Advanced Energy Materials **4**, n/a (2014).

[42] Heliatek GmbH, *Heliatek sets new organic photovoltaic world record efficiency of 13.2%*, press release (2016), accessed on 4th Nov 2016: `http://www.heliatek.com/en/press/press-releases/details/heliatek-sets-new-organic-photovoltaic-world-record-efficiency-of-13-2`.

[43] O. Inganäs, Nature Photonics **5**, 201 (2011).

[44] C.-C. Chen, W.-H. Chang, K. Yoshimura, K. Ohya, J. You, J. Gao, Z. Hong, and Y. Yang, Adv. Mater. **26**, 5670 (2014).

[45] A. R. bin Mohd Yusoff, D. Kim, H. P. Kim, F. K. Shneider, W. J. da Silva, and J. Jang, Energy Environ. Sci. **8**, 303 (2015).

[46] Y. M. Yang, W. Chen, L. Dou, W.-H. Chang, H.-S. Duan, B. Bob, G. Li, and Y. Yang, Nature Photonics **9**, 190 (2015).

[47] L. Lu, T. Xu, W. Chen, E. S. Landry, and L. Yu, Nature Photonics **8**, 716 (2014).

[48] Q. An, F. Zhang, J. Zhang, W. Tang, Z. Deng, and B. Hu, Energy Environ. Sci. **9**, 281 (2016).

[49] L. Zuo, C.-Y. Chang, C.-C. Chueh, S. Zhang, H. Li, A. K.-Y. Jen, and H. Chen, Energy Environ. Sci. **8**, 1712 (2015).

[50] X. Li, X. Ren, F. Xie, Y. Zhang, T. Xu, B. Wei, and W. C. H. Choy, Advanced Optical Materials **3**, 1220 (2015).

[51] Raynergy Tek Inc., *Raynergy tek achieves 7.56% world record single junction slot die coated opv modules*, press release (2015), accessed on 4th Nov 2016: `http://www.raynergytek.com/news.asp`.

[52] T. R. Andersen, H. F. Dam, M. Hosel, M. Helgesen, J. E. Carle, T. T. Larsen-Olsen, S. A. Gevorgyan, J. W. Andreasen, J. Adams, N. Li, F. Machui, G. D. Spyropoulos, T. Ameri, N. Lemaitre, M. Legros, A. Scheel, D. Gaiser, K. Kreul, S. Berny, O. R. Lozman, S. Nordman, M. Valimaki, M. Vilkman, R. R. Sondergaard, M. Jorgensen, C. J. Brabec, and F. C. Krebs, Energy Environ. Sci. **7**, 2925 (2014).

[53] Heliatek GmbH, *Efficiency and lifespan*, homepage (2016), accessed on 17th Nov 2016: http://www.heliatek.com/en/heliafilm/technical-data.

[54] S. Berny, N. Blouin, A. Distler, H.-J. Egelhaaf, M. Krompiec, A. Lohr, O. R. Lozman, G. E. Morse, L. Nanson, A. Pron, T. Sauermann, N. Seidler, S. Tierney, P. Tiwana, M. Wagner, and H. Wilson, Advanced Science **3**, 1500342 (2016), 1500342.

[55] Q.-D. Ou, Y.-Q. Li, and J.-X. Tang, Advanced Science **3**, 1600123 (2016), 1600123.

[56] C.-C. Chueh, M. Crump, and A. K.-Y. Jen, Adv. Funct. Mater. **26**, 321 (2015).

[57] Z. Tang, W. Tress, and O. Inganäs, Materials Today **17**, 389 (2014).

[58] Q. Gan, F. J. Bartoli, and Z. H. Kafafi, Adv. Mater. **25**, 2385 (2013).

[59] M. Burresi, F. Pratesi, F. Riboli, and D. S. Wiersma, Advanced Optical Materials **3**, 722 (2015).

[60] S. Mokkapati and K. R. Catchpole, J. Appl. Phys. **112**, 101101 (2012).

[61] H. A. Atwater and A. Polman, Nature Materials **9**, 205 (2010).

[62] A. K. K. Kyaw, D. H. Wang, D. Wynands, J. Zhang, T.-Q. Nguyen, G. C. Bazan, and A. J. Heeger, Nano Letters **13**, 3796 (2013), pMID: 23805897.

[63] S. B. Dkhil, D. Duché, M. Gaceur, A. K. Thakur, F. B. Aboura, L. Escoubas, J.-J. Simon, A. Guerrero, J. Bisquert, G. Garcia-Belmonte, Q. Bao, M. Fahlman, C. Videlot-Ackermann, O. Margeat, and J. Ackermann, Advanced Energy Materials **4**, n/a (2014).

[64] J. Gilot, I. Barbu, M. M. Wienk, and R. A. J. Janssen, Appl. Phys. Lett. **91**, 113520 (2007).

[65] R. Betancur, P. Romero-Gomez, A. Martinez-Otero, X. Elias, M. Maymó, and J. Martorell, Nature Photonics **7**, 995 (2013).

[66] C. Bronnbauer, J. Hornich, N. Gasparini, F. Guo, B. Hartmeier, N. A. Luechinger, C. Pflaum, C. J. Brabec, and K. Forberich, Advanced Optical Materials **3**, 1424 (2015).

[67] Y. Li, M. E. Calvo, and H. Míguez, Advanced Optical Materials **4**, 464 (2015).

[68] J. D. Myers, W. Cao, V. Cassidy, S.-H. Eom, R. Zhou, L. Yang, W. You, and J. Xue, Energy Environ. Sci. **5**, 6900 (2012).

[69] S. Esiner, T. Bus, M. M. Wienk, K. Hermans, and R. A. J. Janssen, Advanced Energy Materials **3**, 1013 (2013).

[70] C. Cho, H. Kim, S. Jeong, S.-W. Baek, J.-W. Seo, D. Han, K. Kim, Y. Park, S. Yoo, and J.-Y. Lee, Solar Energy Materials and Solar Cells **115**, 36 (2013).

[71] Y. Chen, M. Elshobaki, Z. Ye, J.-M. Park, M. A. Noack, K.-M. Ho, and S. Chaudhary, Physical Chemistry Chemical Physics **15**, 4297 (2013).

[72] Z. Fang, H. Zhu, Y. Yuan, D. Ha, S. Zhu, C. Preston, Q. Chen, Y. Li, X. Han, S. Lee, G. Chen, T. Li, J. Munday, J. Huang, and L. Hu, Nano Letters **14**, 765 (2014).

[73] J.-D. Chen, C. Cui, Y.-Q. Li, L. Zhou, Q.-D. Ou, C. Li, Y. Li, and J.-X. Tang, Adv. Mater. **27**, 1035 (2014).

[74] J.-D. Chen, L. Zhou, Q.-D. Ou, Y.-Q. Li, S. Shen, S.-T. Lee, and J.-X. Tang, Advanced Energy Materials **4**, 1301777 (2014), 1301777.

[75] Z.-Y. Huang, S.-W. Chiu, C.-W. Chen, Y.-H. Chen, L.-Y. Lin, K.-T. Wong, and H.-W. Lin, Nanoscale **6**, 2316 (2014).

[76] J. Yun, W. Wang, S. M. Kim, T.-S. Bae, S. Lee, D. Kim, G.-H. Lee, H.-S. Lee, and M. Song, Energy Environ. Sci. **8**, 932 (2015).

[77] G. Kang, K. Bae, M. Nam, D.-H. Ko, K. Kim, and W. J. Padilla, Energy Environ. Sci. **8**, 2650 (2015).

[78] C. Cho, S. Jeong, H.-J. Choi, N. Shin, B. Kim, E.-c. Jeon, and J.-Y. Lee, Advanced Optical Materials **3**, 1697 (2015).

[79] Y. Chen, M. Elshobaki, R. Gebhardt, S. Bergeson, M. Noack, J.-M. Park, A. C. Hillier, K.-M. Ho, R. Biswas, and S. Chaudhary, Phys. Chem. Chem. Phys. **17**, 3723 (2015).

[80] R. Lampande, G. W. Kim, M. J. Park, B. Y. Kang, and J. H. Kwon, Solar Energy Materials and Solar Cells **151**, 162 (2016).

[81] M. Nam, H.-K. Kwon, S. J. Kwon, S.-H. Kwon, M. Cha, S.-H. Lee, S. Park, D. Jeong, K.-T. Lee, H. Rhee, Y. R. Do, S. Kim, K. Kim, R. H. Friend, J. S. Han, I. K. Han, and D.-H. Ko, Advanced Energy Materials **6**, 1502404 (2016).

[82] J. Ham, W. J. Dong, G. H. Jung, and J.-L. Lee, ACS Appl. Mater. Interfaces **8**, 5990 (2016).

[83] Y. Park, J. Berger, Z. Tang, L. MÃ¼ller-Meskamp, A. F. Lasagni, K. Vandewal, and K. Leo, Applied Physics Letters **109**, 093301 (2016), http://dx.doi.org/10.1063/1.4962206.

[84] K. Forberich, G. Dennler, M. C. Scharber, K. Hingerl, T. Fromherz, and C. J. Brabec, Thin Solid Films **516**, 7167 (2008).

[85] B. V. Andersson, D. M. Huang, A. J. Moule, and O. Inganäs, Appl. Phys. Lett. **94**, 043302 (2009).

[86] J. Nelson, Materials Today **14**, 462 (2011).

[87] J. C. Blakesley and D. Neher, Phys. Rev. B **84**, 075210 (2011).

[88] N. K. Elumalai and A. Uddin, Energy Environ. Sci. **9**, 391 (2016).

[89] G. Li, R. Zhu, and Y. Yang, Nature Photonics **6**, 153 (2012).

[90] K. Leo, Nature Reviews Materials **1**, 16056 (2016).

[91] C. W. Tang, Applied Physics Letters **48**, 183 (1986).

[92] G. Yu, J. Gao, J. C. Hummelen, F. Wudl, and A. J. Heeger, Science **270**, 1789 (1995).

[93] J. J. M. Halls, C. A. Walsh, N. C. Greenham, E. A. Marseglia, R. H. Friend, S. C. Moratti, and A. B. Holmes, Nature **376**, 498 (1995).

[94] M. Hiramoto, H. Fujiwara, and M. Yokoyama, Applied Physics Letters **58**, 1062 (1991).

[95] U. Würfel, D. Neher, A. Spies, and S. Albrecht, Nature Communications **6**, 6951 (2015).

[96] F. Zhang, O. Inganäs, Y. Zhou, and K. Vandewal, Nat. Sci. Rev. **3**, 222 (2016).

[97] A. J. Heeger, Adv. Mater. **26**, 10 (2013).

[98] D. Bartesaghi, I. del Carmen Pérez, J. Kniepert, S. Roland, M. Turbiez, D. Neher, and L. J. A. Koster, Nature Communications **6**, 7083 (2015).

[99] L. Huo, T. Liu, X. Sun, Y. Cai, A. J. Heeger, and Y. Sun, Advanced Materials **27**, 2938 (2015).

[100] X. Guo, M. Zhang, W. Ma, L. Ye, S. Zhang, S. Liu, H. Ade, F. Huang, and J. Hou, Advanced Materials **26**, 4043 (2014).

[101] W. Zinth and U. Zinth, *Optik* (Oldenbourg Wissenschaftsverlag GmbH, 2005).

[102] M. Born and E. Wolf, *Principles of Optics: Electromagnetic Theory of Propagation, Interference and Diffraction of Light* (Pergamon Press, 1975).

[103] H. V. Wolferen and L. Abelmann, *Laser interference lithography* (Nova Science Pub Inc, 2011) Chap. 5, pp. 133–148.

[104] temicon GmbH, http://www.temicon.com/technologien/laserinterferenz-lithographie/ (accessed 06.10.2016).

[105] L. Duempelmann, D. Casari, A. Luu-Dinh, B. Gallinet, and L. Novotny, ACS Nano **9**, 12383 (2015).

[106] V. Shrotriya, G. Li, Y. Yao, T. Moriarty, K. Emery, and Y. Yang, Advanced Functional Materials **16**, 2016 (2006).

[107] E. Zimmermann, P. Ehrenreich, T. Pfadler, J. A. Dorman, J. Weickert, and L. Schmidt-Mende, Nature Photonics **8**, 669 (2014).

[108] National Renewable Energy Laboratory, *Reference Solar Spectral Irradiance: Air Mass 1.5*, online, accessed on 8th Nov 2016: `http://rredc.nrel.gov/solar/spectra/am1.5/`.

[109] T. H. Ghong, S.-H. Han, J.-M. Chung, J. S. Byun, T. J. Kim, D. E. Aspnes, Y. D. Kim, I. H. Park, and Y.-W. Kim, Opt. Lett. **35**, 733 (2010).

[110] M. G. Moharam, T. K. Gaylord, E. B. Grann, and D. A. Pommet, Journal of the Optical Society of America A **12**, 1068 (1995).

[111] B. Gallinet, J. Butet, and O. J. F. Martin, Laser & Photonics Reviews **9**, 577 (2015).

[112] M. G. Moharam and T. K. Gaylord, J. Opt. Soc. Am. **71**, 811 (1981).

[113] L. A. A. Pettersson, L. S. Roman, and O. Inganäs, J. Appl. Phys. **86**, 487 (1999).

[114] O. Inganäs, Z. Tang, J. Bergqvist, and K. Tvingstedt, *Optical modeling and light management in organic photovoltaic devices* (Pan Stanford Publishing, 2014) Chap. Optical Modeling and Light Management in Organic Photovoltaic Devices, pp. 367–427.

[115] A. Meyer and H. Ade, J. Appl. Phys. **106**, 113101 (2009).

[116] J. Kim, S. Jung, and I. Jeong, Journal of the Optical Society of Korea **16**, 6 (2012).

[117] D. Cheyns, B. P. Rand, B. Verreet, J. Genoe, J. Poortmans, and P. Heremans, Applied Physics Letters **92**, 243310 (2008).

[118] M. Campoy-Quiles, P. G. Etchegoin, and D. D. C. Bradley, Physical Review B **72** (2005), 10.1103/physrevb.72.045209.

[119] L. A. Pettersson, S. Ghosh, and O. Inganäs, Organic Electronics **3**, 143 (2002).

[120] D. Cheyns, *Device Physics and Architectures of Organic Bilayer Photovoltaic Cells*, Ph.D. thesis, KATHOLIEKE UNIVERSITEIT LEUVEN (2008).

[121] T. Lanz, B. Ruhstaller, C. Battaglia, and C. Ballif, J. Appl. Phys. **110**, 033111 (2011).

[122] N. Tucher, J. Eisenlohr, H. Gebrewold, P. Kiefel, O. Höhn, H. Hauser, J. C. Goldschmidt, and B. Bläsi, Opt. Express **24**, A1083 (2016).

[123] N. Tucher, J. Eisenlohr, P. Kiefel, O. Höhn, H. Hauser, M. Peters, C. Müller, J. C. Goldschmidt, and B. Bläsi, Optics Express **23**, A1720 (2015).

[124] J. Eisenlohr, N. Tucher, O. Höhn, H. Hauser, M. Peters, P. Kiefel, J. C. Goldschmidt, and B. Bläsi, Opt. Express **23**, A502 (2015).

[125] A. Mellor, I. Tobías, A. Martí, M. Mendes, and A. Luque, Progress in Photovoltaics: Research and Applications **19**, 676 (2011).

[126] Z. Knittl, *Optics of Thin Films (Pure & Applied Optics)* (John Wiley & Sons Ltd, 1976).

[127] J. E. Carlé, M. Helgesen, M. V. Madsen, E. Bundgaard, and F. C. Krebs, J. Mater. Chem. C **2**, 1290 (2014).

[128] L. Lajaunie, F. Boucher, R. Dessapt, and P. Moreau, Phys. Rev. B **88**, 115141 (2013).

[129] E. Yablonovitch, Journal of the Optical Society of America **72**, 899 (1982).

[130] A. Mertens, J. Mescher, D. Bahro, M. Koppitz, and A. Colsmann, Optics Express **24**, A898 (2016).

[131] G. Dennler, K. Forberich, M. C. Scharber, C. J. Brabec, I. Tomis, K. Hingerl, and T. Fromherz, J. Appl. Phys. **102**, 054516 (2007).

[132] J. Mescher, A. Mertens, A. Egel, S. W. Kettlitz, U. Lemmer, and A. Colsmann, AIP Advances **5**, 077188 (2015).

[133] F. Lütolf, M. Stalder, and O. J. F. Martin, Optics Letters **39**, 6557 (2014).

[134] J. Kong, I.-W. Hwang, and K. Lee, Advanced Materials **26**, 6275 (2014).

[135] J. Y. Kim, K. Lee, N. E. Coates, D. Moses, T.-Q. Nguyen, M. Dante, and A. J. Heeger, Science **317**, 222 (2007).

[136] J. Gilot, M. M. Wienk, and R. A. J. Janssen, Advanced Materials **22**, E67 (2010).

[137] Y. Liu, C.-C. Chen, Z. Hong, J. Gao, Y. M. Yang, H. Zhou, L. Dou, G. Li, and Y. Yang, Scientific Reports **3** (2013), 10.1038/srep03356.

[138] H. Zhou, Y. Zhang, C.-K. Mai, S. D. Collins, G. C. Bazan, T.-Q. Nguyen, and A. J. Heeger, Advanced Materials **27**, 1767 (2015).

[139] M. Riede, C. Uhrich, J. Widmer, R. Timmreck, D. Wynands, G. Schwartz, W.-M. Gnehr, D. Hildebrandt, A. Weiss, J. Hwang, S. Sundarraj, P. Erk, M. Pfeiffer, and K. Leo, Advanced Functional Materials **21**, 3019 (2011).

[140] N.-K. Persson and O. Inganäs, Solar Energy Materials and Solar Cells **90**, 3491 (2006).

[141] G. Dennler, K. Forberich, T. Ameri, C. Waldauf, P. Denk, C. J. Brabec, K. Hingerl, and A. J. Heeger, Journal of Applied Physics **102**, 123109 (2007).

[142] R. Timmreck, T. Meyer, J. Gilot, H. Seifert, T. Mueller, A. Furlan, M. M. Wienk, D. Wynands, J. Hohl-Ebinger, W. Warta, R. A. J. Janssen, M. Riede, and K. Leo, Nature Photonics **9**, 478 (2015).

[143] U.S. Department of Energy (DOE)/NREL/ALLIANCE, *Bird Simple Spectral Model - SPCTRAL2*, online, accessed on 11th Nov. 2016: `http://rredc.nrel.gov/solar/models/spectral/`.

[144] J. A. Mayer, B. Gallinet, T. Offermans, I. Zhurminsky, and R. Ferrini, Solar Energy Materials and Solar Cells **163**, 51 (2017).

[145] E. R. Martins, J. Li, Y. Liu, V. Depauw, Z. Chen, J. Zhou, and T. F. Krauss, Nature Communications **4** (2013), 10.1038/ncomms3665.

[146] B. Brudieu, A. L. Bris, J. Teisseire, F. Guillemot, G. Dantelle, S. Misra, P. R. i Cabarrocas, F. Sorin, and T. Gacoin, Advanced Optical Materials **2**, 1105 (2014).

[147] D. M. N. M. Dissanayake, B. Roberts, and P.-C. Ku, Applied Physics Letters **101**, 063302 (2012).

[148] Z. Tang, A. Elfwing, A. Melianas, J. Bergqvist, Q. Bao, and O. Inganäs, J. Mater. Chem. A **3**, 24289 (2015).

[149] Z. Tang, A. Elfwing, J. Bergqvist, W. Tress, and O. Inganäs, Advanced Energy Materials **3**, 1606 (2013).

[150] H. J. Snaith, Energy & Environmental Science **5**, 6513 (2012).

A

Correction factors

Any emergent photovoltaic technology will be primary evaluated on its efficiency that is reported under standard test conditions (STC). Since consequently reports of advances in the obtained efficiency are highly recognized, this had led to a tendency to overestimate the real performance, which was revealed recently by Zimmermann et al. [107]. Hence, it has to be taken special care about a correct characterization of the photovoltaic devices, with some additonal aspects for organic (excitonic) solar cells [106, 150], which are explained below.

A.1 Spectral mismatch

For that purpose, the influence of different light sources can be accounted for by spectral mismatch factor M, which denotes the deviation from the recognized AM1.5G reference spectrum. As an example Fig. A.1a shows the AM1.5G reference $S^{Ref}(\lambda)$ spectrum together with the spectrum of the sciencetech solar simulator $S^{T}(\lambda)$ that was used in this work. The mismatch for different spectral regions is inherent to the xenon arc lamp and can be partly corrected by optical filters. The final match in different spectral regions, which defines the class of the solar simulator, is given by the company [1] and are shown in Fig. A.1b.

[1] http://www.sciencetech-inc.com/fileuploader/download/download/?d=0&-file=custom%2Fupload%2FFile-1470323551.pdf (accessed: 25.11.2016)

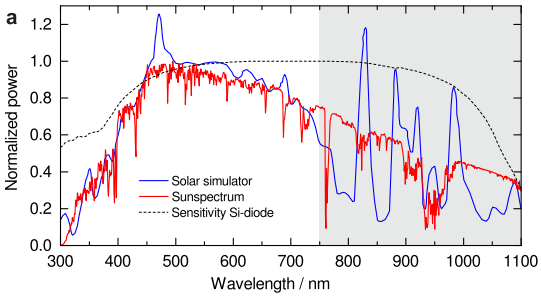

b **SPECTRAL MATCH**

Range (nm)	ASTM AM 1.5G	Sciencetech FRSS AM 1.5G
300-400		
400-500	18.40%	21.81%
500-600	19.90%	20.65%
600-700	18.40%	17.81%
700-800	14.90%	13.00%
800-900	12.50%	11.00%
900-1100	15.90%	15.73%
1100-1400		

Figure A.1: Spectral mismatch. **a** Spectrum of the AM1.5G reference spectrum and the spectrum of the solar simulator. **b** Comparisson of the spectral match in different wavelength regions.

Besides the spectral match, also the power density of the illumination with the solar simulator has to be aligned to 1000 W m^{-1}. This is done with the help of a silicon photodiode with a well known response $R^{Ref}(\lambda)$, which is shown in Fig. A.1a. Once calibrated, the generated photocurrent under illumination with AM1.5G and 100 W m^{-1} is known, and the power of the solar simulator can be adjusted accordingly with the use of this reference photodiode.

However, the spectral response of the test device $R^T(\lambda)$ will usually deviate from $R^{Ref}(\lambda)$, which may lead to a difference in absorbed power when the two spectra are compared. To account for this error, the measured current density on the test device J_T can be devided by M to obtain the correct current density that corresponds to STC illumination conditions $J_{STC} = J_T/M$, where the mismatch factor calculates as [106, 150]

$$M = \frac{\int S^T(\lambda)R^T(\lambda)\ d\lambda \cdot \int S^{Ref}(\lambda)R^{Ref}(\lambda)\ d\lambda}{\int S^{Ref}(\lambda)R^T(\lambda)\ d\lambda \cdot \int S^T(\lambda)R^{Ref}(\lambda)\ d\lambda}. \tag{A.1}$$

Since organic solar cells are usually absorbing below $\lambda < 800$ nm where the agreement of the spectra is high, the mismatch is mostly defined by the differences in the spectral responses of the devices. However, this difference could be reduced if the calibrated reference is equipped with an additional filter (KG5).

Since in the present work on light management mainly relative effects of the measured quantities are investigated, the mismatch correction is not of utmost relevance, a mismatch factor of $M \approx 1.08$ was calculated in this work only for the measurements of Sec. 5.3, which is a typical value for organic photovoltaics [2] Further, to control the resulting current, J_{STC} can be compared

[2] see http://assets.newport.com/webDocuments-EN/images/Spectral_Mismatch-App_Note_51.PDF (accessed in August 2016)

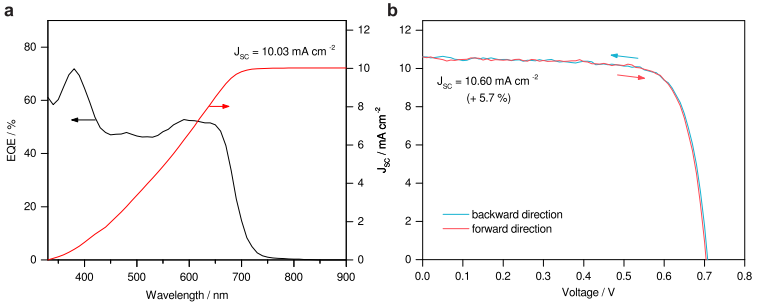

Figure A.2: (a) EQE measurement of the reference device with the integrated current density. (b) JV- measurement of the same cell, exhibiting a 6% higher current after correction with the calculated mismatch factor and accounting for the

to the value that is obtained by Eq. (2.5) through spectral integration of the measured η_{EQE} multiplied with the AM1.5G, which is shown in Fig. A.2a. When compared to the corrected J-V measurement only a small deviation of 6% is observed, which is far below the threshold set by Ref. [107].

Both the adjustment procedure with the photodiode and the correction with M, however, provide only an wavelength independent correction (for values like J_{SC} and η_{PCE}), whereas the enhancement of the light management is more influenced by individual spectral regions. For example a large enhancement due to the light management in the range 700 nmλ < 800 nm will still be underestimated by the solar simulator measurement, since for these wavelength $S^{T}(\lambda)$ is much lower than $S^{Ref}(\lambda)$ (see Fig. A.1a).

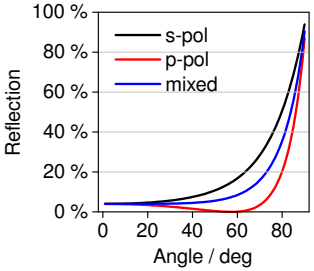

Figure A.3: fresnel reflection at the quarz window of the sample container.

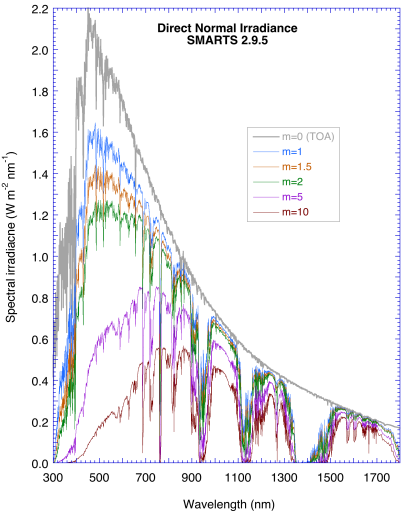

Figure A.4: Influence of different air masses on the irradiation spectrum. Calculated with SMARTS 2.9.5 for air mass=0 to 10 (By Solar Gate (My own calcualtions and graphing) [GFDL (http://www.gnu.org/copyleft/fdl.html) or CC-BY-SA-3.0 (http://creativecommons.org/licenses/by-sa/3.0/)], via Wikimedia Commons).

A.2 Quartz window

A second correction becomes necessary due to the N_2- filled transfer box that is used for most measurements. The quartz window, through which the cells are illuminated introduce a additional reflections, which reduces the transmitted power that arrives at the cells. To account for that, Eqs. 3.1) and (3.2) are used to calculate an angle dependent reflection R, which is depicted in Fig. A.3.

For the calculations, a wavelength independent refractive index of $n = 1.5$ is assumed for the quartz and $n = 1$ for air. The contributions of both polarizations are further equally mixed to account for the unpolarized light of the solar simulator. Since the reflection at straight incidence becomes $R = 4\%$, the correction factor $Q(\theta) = J(\theta)_{final}/(J(\theta)_T/M)$ at $\theta = 0°$ has a value of 0.96, which decreases to 0.85 at $\theta = 70°$.

A.3 Other spectra

Another spectral consideration, that is especially relevant for the simulations in Chap. 7 is the changes that are introduced from atmospheric absorption. Dependent zenith angle and thus on the path of the light to the ground, the air mass (AM) describes the number of atmosphere thicknesses which the light has to travel through the atmosphere. Dependent on this number part of the power is absorbed by the atmosphere, which is the reason for the color appearance at sunset and sunrise. The changes in the spectrum are shown in Fig. A.4 for AM0 to AM10.

Publications

Light Management for OPV,
J. Mayer, B. Gallinet, T. Offermans and R. Ferrini, CSEM Scientific Report 2015, http://www.csem.ch/Doc.aspx?id=40087, 67 (2015)

Diffractive nanostructures for enhanced light-harvesting in organic photovoltaic devices,
J. Mayer, B. Gallinet, T. Offermans and R. Ferrini, Opt. Express **24**, A358–A373 (2016), doi:10.1364/OE.24.00A358

Self-Contained Optical Enhancement Film for Printed Photovoltaics,
J. Mayer, B. Gallinet, T. Offermans, I. Zhurminsky and R. Ferrini, Sol. Energy Mat. Sol. Cells **163**, 51–57 (2017), doi: 10.1016/j.solmat.2017.01.015

Embedded Light Management Films for Printed Photovoltaics,
J. Mayer, B. Gallinet, T. Offermans, I. Zhurminsky and R. Ferrini, CSEM Scientific Report 2016, submitted (2017)

Printed organic tandem solar cells including light management,
J. Mayer, T. Offermans, M.Chrapa and G. Nisato, in preparation (2017)

Talks

Diffractive Nanostructures for Enhanced Light-Harvesting in OPV Devices, Talk at the Large-area, Organic & Printed Electronics Convention (LOPEC), Munich (DE), 06.04.2016.

Diffraction Gratings for Enhanced All-Season Energy-Harvesting in OPV Devices, Invited talk at the International Conference on Simulation of Organic Electronics and Photovoltaics (simOEP), Winterthur (CH), 15.09.2016.

Poster Contributions

Application of nanoscale diffraction gratings for light-management in OPVs, J. Mayer, T. Offermans, B. Gallinet, I. Zhurminski, M. Chrapa and R. Ferrini. Poster at the international summer school on organic photovoltaics 2014, Strasbourg (FR), 04.09.2014

Nanoscale surface-relief diffraction gratings for light-management in OPVs, J. Mayer, T. Offermans, B. Gallinet, I. Zhurminski, M. Chrapa and R. Ferrini. Poster at the Large-area, Organic & Printed Electronics Convention (LOPEC), Munich (DE), 03.03.2015.

Application of nanoscale diffraction gratings for light-management in OPVs, J. Mayer, T. Offermans, B. Gallinet, I. Zhurminski, M. Chrapa and R. Ferrini. Poster at the 13. Nationale Photovoltaik-Tagung 2015, Basel (CH), 16.03.2015.

Light Management for Organic Photovoltaic Devices,
J. Mayer, B. Gallinet, T. Offermans, T. Gasser and R. Ferrini. Poster at the Swiss NanoConvention, Neuchatel (CH), 27.05.2015.

Light Management for Organic Photovoltaic Devices,
J. Mayer, B. Gallinet, T. Offermans, T. Gasser and R. Ferrini. Poster at the 9th international nanoscience conference (INASCON), Basel (CH), 13.08.2015

Light-Management for Organic PV,
J. Mayer, T. Offermans, B. Gallinet and R. Ferrini. Best poster award at the Swiss-e-Print, Neuchatel (CH), 01.10.2015.

Acknowledgements

Foremost, I would like to thank my fiancée Tina for her unlimited support and patience and her ability to always cheer me up. I greatly thank her for all the (short) nights that she took care of our son Moritz alone. During the hard times, this gave me some rest and the strength to finish this thesis, which I would not have accomplished without her. In particular, I thank Moritz, who always made me forget about any stress, just by watching his attempts to crawl, to grin, to walk and to chew or throw things – or just by discovering the world.

Furthermore, I thank my friends and my sister, who always accompanied and motivated me during this time and longer. I will remember the great summer holidays 2015 and 2016 and the good surf. Thanks goes to Michael Och, who accompanied me during our studies and with whom I share and advanced the passion for slopestyle freeskiing. Special thanks goes to Jonas Jelli, the Neo-Prenes-Wolf-Gang and the Robbendompteure for their fresh music support, including "Grammatik" and "Mixtape31", which greatly helped to be both productive and relaxed during commutation.

I thank Dr. Rolando Ferrini for the chance of executing my thesis at the CSEM Center Muttenz. I am grateful for his supervision and guidance. Further thanks go to Dr. Ton Offermans for supervision of the work and his support, whenever I had questions or problems, as well as to Dr. Benjamin Gallinet for his advice and for helpful discussions.

Moreover, I thank Prof. Dr. Christian Schönenberger and Dr. PD Michel Calame from the Nanoelectronics group at the University of Basel for their scientific guidance and supervision.

Special thanks go to Nicolas Glaser for introducing me to the Birs wave, to

Fabienne Herzog for hosting the yearly “Fiirtigs-idringgede”, to Marec Chrapa for sharing his great lab experience with me and to all other collegues from CSEM Muttenz for their support during this time.

Contribution of other people to this work

For their help in experiments in this thesis, I would like to acknowledge the following persons

- *Igor Zhurminsky* for creating the simulated structures with interference holography, including the master and foil fabrication of the crossed nanostructure (Secs. 5.1 & 5.2) and the lorentzian lineshape nanostructure (Sec. 5.3), as well as the record of their SEM pictures.
- *Timo Gasser*, who built the setup for and performed the diffraction efficiency measurements of Fig. 4.11c
- *Refik Maxhuni* & *Jiaming Xiao* for the help with nanostructure replication and device fabrication in Chap. 5
- *Marek Chrapa* & *Ton Offermans* for the help with OPV device fabrication in Chap. 6
- *Tilman Beierlein* (ZHAW) for the ellipsometric measurement and subsequent fitting of the thin absorber films presented in Fig. 4.1a.

Finally, I would like to thank my parents, which always supported me with my decisions and pursuits. I am grateful for their parenting and the values, which I adopted from them and which eventually brought me to this point.